

# **Real Time Completely Bio-compatible Flow Control Technique for Microchannel Based Physiological Studies**

by

Dilendra Lalantha Galhena

Thesis submitted to the department of mechanical engineering in the faculty of  
Engineering at Monash University, Australia in partial fulfillment of the requirements  
for the degree of

Degree of Master of Engineering Science (Research)

Supervisors:

Dr. Josie Carberry

Dr. Andreas Fouras

Clayton, Australia

---

## **Copyright Notices**

### **Notice 1**

Under the Copyright Act 1968, this thesis must be used only under the normal conditions of scholarly fair dealing. In particular no results or conclusions should be extracted from it, nor should it be copied or closely paraphrased in whole or in part without the written consent of the author. Proper written acknowledgement should be made for any assistance obtained from this thesis.

### **Notice 2**

I certify that I have made all reasonable efforts to secure copyright permissions for third-party content included in this thesis and have not knowingly added copyright content to my work without the owner's permission.

## Acknowledgement

My utmost gratitude goes towards my supervisors Dr. Josie Carberry and Dr. Andreas Fouras for their constant support, guidance and good nature.

My appreciation goes to the Monash Mechanical & Physics department workshop members for dedicating their time to fabricate system design components.

I would like to thank Dr. Judy Callaghan from Monash Micro Imaging for the guidance provided in completing multi-photon confocal Imaging.

Special thanks to all at Laboratory of Dynamic Imaging, Monash University for their support and direction. It was a privilege to complete my Master's Thesis with you all.

---

# **Real Time Completely Bio-compatible Flow Control Technique for Microchannel Based Physiological Studies**

## **Abstract**

A real-time and biocompatible flow control technique for microchannel based physiological experiments has been developed. Current micro flow control techniques are limited in their ability to develop physiological waveforms and maintain high flow accuracy. The new technique provides accurate real time flow control of steady and user specified complex waveforms. This low impact flow control technique offers high adaptability for a wide range of frequencies and flow rates. The system is highly scalable as the operating parameters rely on the scale of specific components.

A prototype system was constructed incorporating a constant air pressure source to supply the base flow rate, a compact, disposable flow probe to measure the flow rate and a real time feedback control system to drive a fluid control valve. The fluid control valve allows for finer control over the base flow by pinching the silicone tube carrying the flow. Performance tests were completed for this prototype, showing a steady flow error of 1.2%. The optimum pulsatile range was for oscillations between 1 – 3 Hz. For sinusoidal waveforms within this range the total harmonic distortion was under 2% and the root mean square error was under 8 %.

Micro PIV and thrombus growth experiments were completed to demonstrate the capacity of this flow control systems ability to be used in microchannel based physiological experiments. Micro PIV results indicate that viscous forces affect the flow profile within a high aspect ratio microchannel with fluid viscosity of  $4 \times 10^{-3}$  N.s/m<sup>2</sup> and a Womersley number between 0.117 and 0.2925. Thrombus growth experiments comparing the pulsatile flow with steady flow at the microchannel wall showed that pulsatile flow promoted higher thrombi growth. It was hypothesised that pulsatile velocities varying between 33.1 and 67.5 mm/s in a platelet rich region would significantly promote the development of thrombi.

## Nomenclature

$\alpha$	Womersley number
$\epsilon$	Ratio between the correlation weighting at $z_{corr}$ and $z = 0$
$\rho$	Density
$\mu_{TA}$	Mean thrombus area
$\sigma_{TA}$	Standard deviation of sample thrombus area
$\tau$	Shear rate
$\lambda$	Particle fluorescence wavelength
$A$	Amplitude
$A_{1,2}$	Cross sectional area
$A_i$	Weighting coefficient of Savitzky-Golay algorithm
$d_p$	Particle diameter
$e(t)$	Flow error
$f$	Frequency
$f^\#$	Focal number
$h$	Height dimension
$i$	Data point
$K_d$	Derivative gain
$K_d \frac{d}{dt} e(t)$	Differential term
$K_i$	Integral gain
$K_i \int_0^t e(\tau) d\tau$	Integral term
$K_p$	Proportional gain
$K_p e(t)$	Proportional term
$M$	Magnification factor
$n$	Number of data points
$P$	Pressure
$P_{freq}$	Power of input frequency
$P_{total}$	Total power of waveform
$Q_m$	Microchannel mean flow rate
RBC	Red blood cells
RMSE %	Root mean square error percentage
RMSE	Root mean square error
RMS <sub>input</sub>	Root mean square of input waveform
$t$	Instantaneous time
THD	Total harmonic distortion
$u(t)$	Desired flow rate

$V_r(t)$	Real time flow measurement
$u_d(t)$	Digitally stored flow measurement
$u_s(t)$	Standby flow rate
$V$	Flow velocity
$V_{PID}$	PID calculated control valve velocity voltage measurement
$w$	Width dimension
$x_{input}$	Input flow rate
$x_{measured}$	Measured flow rate
$x_{px}$	Pixel displacement
$x_{TA}$	Thrombus area
$y_k$	Smoothed data point
$y(t)$	Controlled flow rate
$y_{fb}(t)$	Feedback flow rate
$V_{px}$	Pixel velocity
$V_r(t)$	External real time flow voltage measurements
$u_d(t)$	Digitally stored flow measurements
$T_i$	Integral time
$T_d$	Deferential time
$8\beta^2 D \Delta t f^{#2}$	Effects of Brownian motion
$u_r(t)$	External real time flow measurements
$u_d(t)$	Digitally stored flow measurements
$V_{PID}(t)$	Variable voltage for valve control
$y_{fb}(t)$	Feedback flow measurements
$u_s(t)$	Standby flow
$V_{fb}(t)$	Feedback flow voltage measurements
$e_{old}(t)$	Flow error for last iteration
$e_{tot}(t)_{total}$	Total flow error for run

## List of equations

$$P_1 + \frac{1}{2}\rho V_1^2 = P_2 + \frac{1}{2}\rho V_2^2 \quad (1)$$

$$q = V_1 A_1 = V_2 A_2 \quad (2)$$

$$q = A_2 [2(P_1 - P_2)/\rho(1 - (A_2/A_1)^2)]^{\frac{1}{2}} \quad (3)$$

$$u(t) = K_p e(t) + K_i \int_0^t e(\tau) d\tau + K_d \frac{d}{dt} e(t) \quad (4)$$

$$K_i = \frac{K_p}{T_i} \quad (5)$$

$$K_d = K_p T_d \quad (6)$$

$$T_d = \frac{T_i}{4} \quad (7)$$

$$u(t) = K_p \left[ e(t) + \frac{1}{T_i} \int_0^t e(\tau) d\tau + T_d \frac{d}{dt} e(t) \right] \quad (8)$$

$$(y_k)_s = \frac{\sum_{i=n}^n A_i y_{k+i}}{\sum_{i=n}^n A_i} \quad (9)$$

$$THD = \left( \frac{P_{total} - P_{frq}}{P_{frq}} \right) \times 100 \% \quad (10)$$

$$RMSE \% = \frac{RMSE}{RMS_{input}} = \frac{\sqrt{\frac{\sum_{i=n}^n (x_{i_{input}}^2 - x_{i_{measured}}^2)}{n}}}{\sqrt{\frac{\sum_{i=n}^n (x_{i_{input}}^2)}{n}}} \times 100\% \quad (11)$$

$$\Delta t = 1/f \quad (12)$$

$$V_{px} = \frac{\Delta x_{px}}{\Delta t} \quad (13)$$

$$z_{corr} = \left[ \frac{1-\sqrt{\epsilon}}{\sqrt{\epsilon}} \left( f^{\#2} d_p^2 + \frac{5.95 (M+1)^2 \lambda^2 f^{\#2}}{M^2} + 8\beta^2 D \Delta t f^{\#2} \right) \right]^{\frac{1}{2}} \quad (14)$$

$$\tau = \frac{6Qm}{wh^2} \quad (15)$$

$$M = \frac{m}{x_{px}} \quad (16)$$

$$x = x_{px} \times M \quad (17)$$

$$v = \frac{x_{px}}{\Delta t} \times M \quad (18)$$

$$f(x_{TA}; \mu_{TA}, \sigma_{TA}^2) = \frac{1}{\sigma_{TA} \sqrt{2\pi}} e^{-\frac{(x_{TA} - \mu_{TA})^2}{2\sigma_{TA}^2}} \quad (19)$$

## List of tables

<b>Table 2.1</b> Summary table for available pump system .....	15
<b>Table 2.2</b> Change in response of the control system for independent increase of PID gain .....	20
<b>Table 2.3</b> Guide table for increasing performance of the flow control system .....	50
<b>Table 4.1</b> Summary of adhesion receptors and ligands used at different shear rates .....	73
<b>Table 4.2</b> List of chemical and quantities required for producing Tyrodes buffer .....	77
<b>Table 4.3</b> Imaging properties for x-y-z planes for each thrombi evaluation characteristic.....	81



## List of figures

<b>Figure 1.1</b> Pie chart of global mortality for 2008.....	1
<b>Figure 1.2</b> Pie chart of cardiovascular condition leading to global mortality for 2008.....	2
<b>Figure 1.3</b> Varying pulsatile flow waveforms along an arterial system.....	3
<b>Figure 1.4</b> Flowchart presenting significance of developing a new flow control technique.....	4
<b>Figure 2.1</b> Block diagram of the flow control technique.....	7
<b>Figure 2.2</b> Simple gear pump design.....	8
<b>Figure 2.3</b> Cross-sectional view through an impeller pump.....	9
<b>Figure 2.4</b> Cross-sectional view of a piston metering pump.....	10
<b>Figure 2.5</b> CAD model of an axial flow blood pump.....	10
<b>Figure 2.6</b> Side view of a peristaltic pump mechanism.....	11
<b>Figure 2.7</b> Common piston pump design.....	12
<b>Figure 2.8</b> Progressive cavity pump design.....	13
<b>Figure 2.9</b> Servo controlled syringe pump system.....	13
<b>Figure 2.10</b> Dual pump system.....	14
<b>Figure 2.11</b> Cross-sectional view of a venture meter.....	16
<b>Figure 2.12</b> Cross-sectional view of an orifice meter.....	16
<b>Figure 2.13</b> The transfer function block diagram .....	21
<b>Figure 2.14</b> Schematic diagram of (a) the flow control system (b) Expanded view of the fluid control valve (c) Cross section of the 3D printed four channel flow.....	22
<b>Figure 2.15</b> Schematic diagram of the pressure pump system.....	23
<b>Figure 2.16</b> Micro diaphragm air pump ( KNF, NMP 830 KNDC 12V).....	23
<b>Figure 2.17</b> The pressure box 3D Printed from Object Fullcure 7020 material.....	24
<b>Figure 2.18</b> Clippards EV-P-05-6025 proportional valve.....	25
<b>Figure 2.19</b> Clippards, EV-2-12-L solenoid valve.....	25
<b>Figure 2.20</b> Honeywell, ASDX005D44D differential pressure sensor.....	26
<b>Figure 2.21</b> The fluid holding reservoir.....	26
<b>Figure 2.22</b> The Labview interface designed to control the pressure system.....	27

<b>Figure 2.23</b> Control hardware for the pressure system.....	28
<b>Figure 2.24</b> The fluid control valve.....	29
<b>Figure 2.25</b> The designed 3D printed flow probe.....	30
<b>Figure 2.26</b> The feedback control system.....	31
<b>Figure 2.27</b> Flow chart of PID control algorithm.....	32
<b>Figure 2.28</b> Graph of (a) calibration curves of pressure loss as a function of the flow rate for each orifice diameters of the flow probe. (b) the cross sectional view of the flow probe.....	36
<b>Figure 2.29</b> Measured flow rate as a function of the operational pressure range of the flow control system for different viscous fluids.....	37
<b>Figure 2.30</b> Experimental setup used for manual tuning.....	38
<b>Figure 2.31</b> The response time as a function of proportional gain.....	39
<b>Figure 2.32</b> The flow error as a function of integral gain.....	40
<b>Figure 2.33</b> Performance test experimental setup.....	41
<b>Figure 2.34</b> Measured flow versus the programmed flow for 40% hematocrit fluid.....	42
<b>Figure 2.35</b> Plot of (a) total harmonic distortion as a function of the sinusoid frequency (b) the root mean square error as a function of sinusoid frequency.....	43
<b>Figure 2.36</b> Transonic perivascular probe attached to a rat aorta to record blood flow.....	44
<b>Figure 2.37</b> Production of (a) a digitised human aorta waveform (b) rat aorta waveform.....	45
<b>Figure 3.1</b> Development of Instantaneous velocity from micro PIV image pairs.....	50
<b>Figure 3.2</b> Image presenting (a) change in particle size when imaged as it moves away from the focal plane (b) a micro PIV image seeded with particles.....	53
<b>Figure 3.3</b> Experimental setup used for micro PIV flow evaluation.....	55
<b>Figure 3.4</b> Imaging planar locations inside the microchannel for 4 frequencies.....	56
<b>Figure 3.5</b> Step process involved in generating contour plots of in-plane magnitude of the velocity as a function of time and the distance from the center from micro PIV data.....	58
<b>Figure 3.6</b> Steady flow velocity profile across the width of the microchannel.....	59
<b>Figure 3.7.</b> Flow probe measurement of input flow rate averaged over 60 seconds and plotted as a function of normalised time .....	60
<b>Figure 3.8</b> Contour plots of in-plane magnitude of the velocity at $z = 100\ \mu\text{m}$ above the bottom of the microchannel wall as a function of time and the distance from the center for frequencies (a) 1 Hz, (b) 1.5 Hz, (c) 2 Hz and (d) 2.5 Hz .....	61

<b>Figure 3.9</b> Temporally normalised contour plots of in-plane magnitude of the velocity at $z = 100\ \mu\text{m}$ above the bottom of the microchannel wall as a function of time and the distance from the center for frequencies (a) 1 Hz, (b) 1.5 Hz, (c) 2 Hz and (d) 2.5 Hz .....	62
<b>Figure 3.10</b> Contour plots of in-plane magnitude of the velocity at $z = 50\ \mu\text{m}$ above the bottom of the microchannel wall as a function of time and the distance from the center for frequencies (a) 1 Hz, (b) 1.5 Hz, (c) 2 Hz and (d) 2.5 Hz .....	63
<b>Figure 3.11</b> Temporally normalised contour plots of in-plane magnitude of the velocity at $z = 50\ \mu\text{m}$ above the bottom of the microchannel wall as a function of time and the distance from the center for frequencies (a) 1 Hz, (b) 1.5 Hz, (c) 2 Hz and (d) 2.5 Hz.....	64
<b>Figure 3.12</b> Contour plots of in-plane magnitude of the velocity at $z = 25\ \mu\text{m}$ above the bottom of the microchannel wall as a function of time and the distance from the center for frequencies (a) 1 Hz, (b) 1.5 Hz, (c) 2 Hz and (d) 2.5 Hz .....	65
<b>Figure 3.13</b> Temporally normalised contour plots of in-plane magnitude of the velocity at $z = 25\ \mu\text{m}$ above the bottom of the microchannel wall as a function of time and the distance from the center for frequencies (a) 1 Hz, (b) 1.5 Hz, (c) 2 Hz and (d) 2.5 Hz .....	66
<b>Figure 3.14</b> Contour plots of in-plane magnitude of the velocity at (a) $z = 100\ \mu\text{m}$ , (b) $z = 50\ \mu\text{m}$ , (c) $z = 25\ \mu\text{m}$ above the bottom of the microchannel wall as a function of time and the distance from the center for frequency of 1 Hz .....	67
<b>Figure 3.15</b> (a) Poiseuille flow, (b) experimentally evaluated flow velocity profile developed inside a rectangular microchannel.....	68
<b>Figure 4.1</b> Concentration profile of platelets (a) without ghost red blood cells developing tubular pinch effect. (b) with ghost red blood cells.....	70
<b>Figure 4.2</b> Process of platelet aggregation.....	71
<b>Figure 4.3</b> Electron microscopy images of (a) tether formation of a platelet (b) a group of platelets adhering to each via the membrane tethers.....	72
<b>Figure 4.4</b> Cross sectional area of thrombus growth over a 10 min time period.....	72
<b>Figure 4.5</b> The progression of atherosclerosis.....	74
<b>Figure 4.6</b> Shear rate vs. shear stress of blood with 40% hematocrit.....	75
<b>Figure 4.7</b> Experimental setup for the thrombus growth.....	79
<b>Figure 4.8</b> Image of fluorescing thrombi superimposed on to the bright field image.....	79
<b>Figure 4.9</b> Inverted confocal microscope setup used for biological cell imaging.....	80
<b>Figure 4.10</b> Overlapping Image acquired in the x-y plane along the microchannel and $\Delta z$ plane increments.....	81
<b>Figure 4.11</b> Maximum projected image in the x-y plane (a) unfiltered with background illumination (b) filtered with background illumination removed.....	82
<b>Figure 4.12</b> Thrombi identified from Matlab function .....	84

<b>Figure 4.13</b> Planar location and direction of flow inside the microchannel.....	84
<b>Figure 4.14</b> Avizo three dimensional re-construction of (a) thrombi developed under steady flow (b) thrombi developed under pulsatile flow.....	85
<b>Figure 4.15</b> Maximum projected image of (a) steady flow (b) pulsatile flow.....	86
<b>Figure 4.16</b> graph of average density of thrombi growth over half a width of the microchannel for (a) steady flow (b) pulsatile flow (c) steady and pulsatile flow.....	88
<b>Figure 4.17</b> graphical comparison of (a) fluorescence image (b) density of thrombi growth (c) particle image velocimetry at $z = 50 \mu\text{m}$ plane developed under pulsatile flow.....	90
<b>Figure 4.18</b> Population density distribution of thrombi area for steady and pulsatile flow.....	91
<b>Figure 4.19</b> Florescence image of thrombi selected (a) at the middle of the microchannel for steady flow (b) at the wall of the microchannel for steady flow (c) at the middle of the microchannel for pulsatile flow (d) at the wall of the microchannel for pulsatile flow.....	92
<b>Figure 4.20</b> Bar graph of average thrombi height and standard deviation for ten thrombi selected for steady and pulsatile flow at the middle and wall of the microchannel.....	94
<b>Figure 5.1</b> CAD image of a conceptual fluid controlled cross slot designed to isolate and interrogate cell properties.....	99

## Table of Contents

Abstract .....	i
Nomenclature .....	ii
List of equations .....	iv
List of tables .....	v
List of figures .....	vi
<b>1.0 Introduction .....</b>	<b>1</b>
1.1 Motivation of project .....	1
1.2 Aims .....	5
1.2.1 Primary Aims .....	5
1.2.2 Secondary Aims .....	6
<b>2.0 Flow Control Technique &amp; Prototype Design .....</b>	<b>7</b>
2.1 Background Literature .....	7
2.1.1 Pump Systems .....	8
2.1.2 Flow probe designs .....	15
2.1.3 Feedback control system .....	18
2.2 Prototype system .....	21
2.2.1 Pressure system .....	23
2.2.2 Flow control valve design .....	29
2.2.3 Flow probe Design .....	30
2.2.4 Feedback control system .....	31
2.3 Methods .....	35
2.3.1 Flow Probe Calibration test .....	35
2.3.2 Effects of Viscosity on steady flow performance .....	37
2.3.3 Feedback Control System Tuning .....	38
2.3.3 Flow Control System Performance Tests .....	41
2.4.3 Steady flow .....	42
2.4.4 Sinusoidal Pulsatile flows .....	42
2.4.5 Complex Waveforms .....	44
2.5 Flow control technique key advantages .....	46
2.6 Chapter conclusion .....	48
<b>3.0 Particle Image Velocimetry .....</b>	<b>49</b>
3.1 Background .....	49
3.1.1 Blood velocity profile and diseases .....	49
3.1.2 Micro PIV .....	50
3.1.4 Factors affecting micro PIV quality .....	51
3.2 Methods .....	55
3.2.1 Experimental procedure .....	55
3.2.2 Pixels to ms <sup>-1</sup> .....	57
3.2.3 Developing in plane velocity plots .....	57
3.3 Results & Discussion .....	59
3.3.1 Normalised input flow rate flow probe measurement .....	59
3.3.2 Micro PIV results z = 100 $\mu\text{m}$ .....	60
3.3.3 Micro PIV results z = 50 $\mu\text{m}$ .....	63
3.3.3 Micro PIV results z = 25 $\mu\text{m}$ .....	65
3.3.3 Normalised micro PIV results for 1 Hz .....	67

3.4 Chapter conclusion .....	68
<b>4.0 Blood flow .....</b>	<b>69</b>
4.1 Background .....	69
4.1.1 Blood flow and disease .....	69
4.1.2 Platelet distribution in microvessels .....	70
4.1.3 Platelet aggregation process .....	71
4.1.4 Stenosis .....	73
4.1.5 Atherosclerosis .....	74
4.1.6 Factors effecting blood viscosity .....	75
4.2 Methods .....	76
4.2.1 Experimental Procedure .....	76
4.2.2 Thrombi Staining procedure .....	79
4.2.3 Thrombi imaging procedure .....	80
4.2.4 Image Processing .....	81
4.2.5 Data evaluation .....	83
4.3 Results & Discussion .....	85
4.3.1 Density of thrombi growth .....	88
4.3.2 Population density for steady and pulsatile .....	90
4.3.3 Thrombus height for steady and pulsatile .....	91
4.4 Chapter conclusion .....	95
<b>5.0 Conclusions .....</b>	<b>96</b>
5.1 Summary of major findings and contributions to the field .....	96
5.2 Recommendations for future work .....	98
<b>6.0 References .....</b>	<b>100</b>

# 1.0 Introduction

## 1.1 Motivation of project

Cardiovascular diseases are the principal cause of mortality worldwide. It accounts for 30% of global deaths. As shown in figure 1.1 this is an estimated 17.3 million people per year. This figure is projected to increase to 23.6 million people per year by the year 2030.

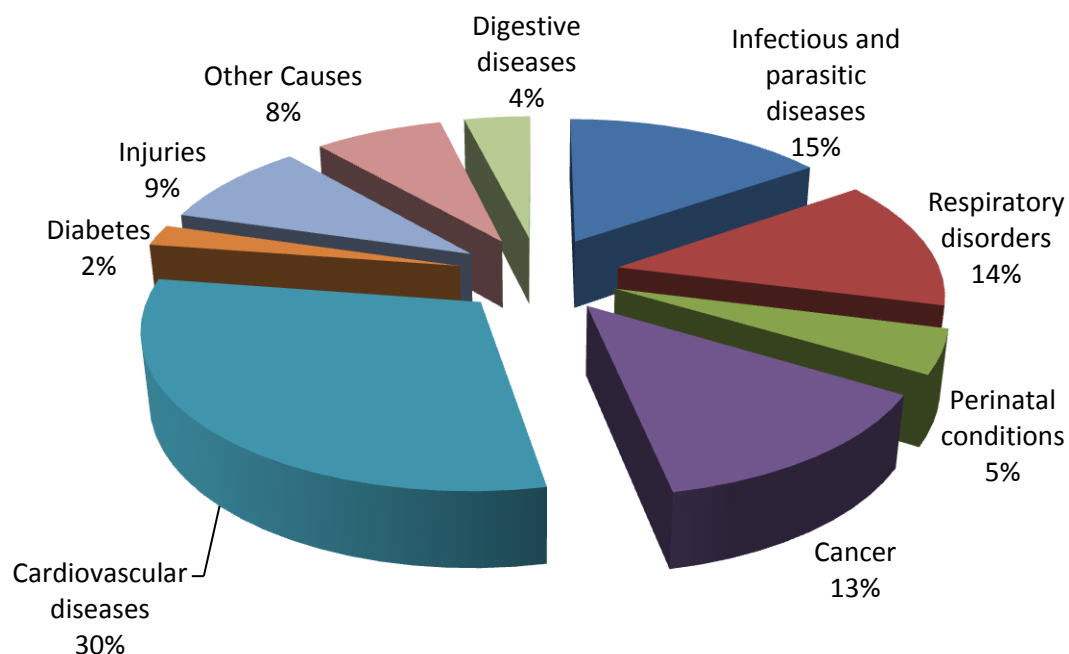


**Figure 1.1** Pie chart of global mortality for 2008 (World Health Organization 2011). Cardiovascular diseases accounts for accounts for 30% of global deaths, which is an estimated 17.3 million people per year.

In addition to health implications, cardiovascular diseases also impact at a macro-economic level. Over 80% of worldwide deaths from cardiovascular diseases occur in low and middle income countries. This is estimated to reduce gross domestic product (GDP) between 1 and 5% in low and middle income countries experiencing rapid economic growth (World Health Organization 2011).

Cardiovascular diseases are caused by defects of the heart and blood vessels. As shown in figure 1.2, heart attack, stroke and hypertension accounts for majority of cardiovascular diseases. These diseases are often directly related to atherosclerosis. In atherosclerosis, blood vessels narrow due to accumulation of lipids in the sub-endothelial layer. This unstable accumulation of plaque is prone to rupture. Rupture

exposes thrombogenic<sup>1</sup> material promoting thrombi development inside vessels (Charo & Taub 2011). These undesirable thrombi travel downstream to occlude smaller vessels. A heart attack occurs when an artery to the heart is significantly occluded. Similarly, a stroke occurs when an artery supplying blood to the brain is occluded.

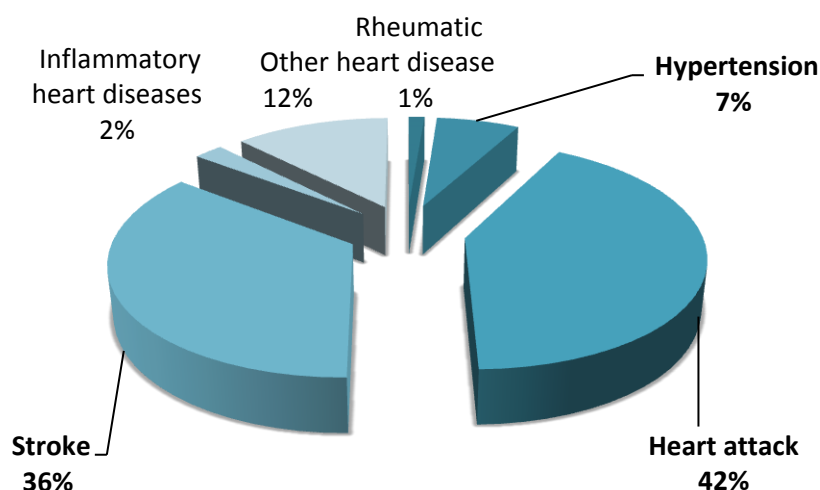


**Figure 1.2** Pie chart of cardiovascular condition leading to global mortality for 2008 (World Health Organization 2011). Heart attack, stroke & hypertension accounts for the major portion of cardiovascular diseases.

The processes of thrombosis require platelet adhesion and subsequent aggregation. Studies have linked abnormal increases in platelet aggregation to heart attack and stroke. There are many biomechanical mechanisms promoting platelet adhesion and aggregation. The magnitude of the shear stress has been known to affect platelet function (Tolouei *et al.* 2011). Recently it was shown that the shear gradient can initiate platelet adhesion even in the absence of soluble agonists (Nesbitt *et al.* 2009). For the activation process, platelets must experience high accelerating shear followed by subsequent decelerating shear (Nesbitt *et al.* 2009).

High level of research interest exists in understanding hemodynamics inside vessels, platelet activation and the role of flow in cardiovascular conditions such as atherosclerosis (Ku *et al.* 1985). Sherwood *et al.* (2014) investigated the relationship between hematocrit, viscosity and velocity with a pressure driven system. The majority of work on platelet function, hematocrit, viscosity and velocity profiles have been investigated under steady flow. But Nesbitt *et al.* (2009) experimentally showed the important role of varying flow in platelet aggregation and hemodynamics. Experiments designed to investigate these process are predominantly microchannel based, and have only been completed under steady or limited number of pulsatile flow conditions. However, in-vivo blood flow is complex

<sup>1</sup> Thrombogenic substances induce and promote the formation of thrombi



and highly dependent on vessel location. Figure 1.3 presents how pulsatile flow waveforms vary at different parts of the arterial system.

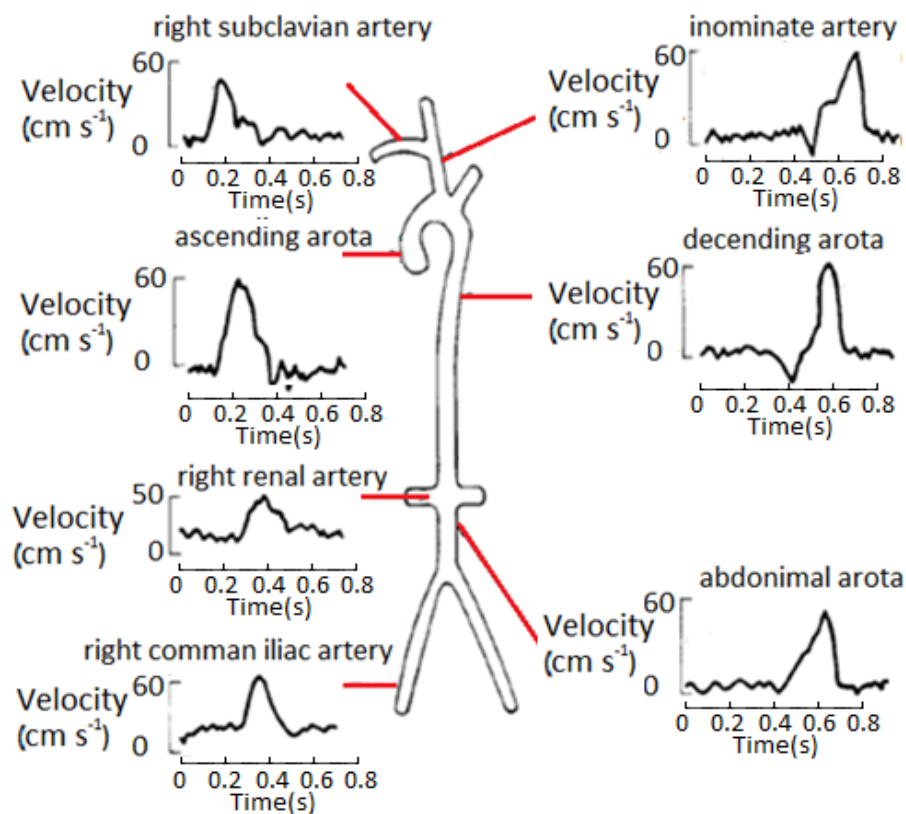


**Figure 1.3** Varying pulsatile flow waveforms along an arterial system. Each velocity profiles consist of a unique pattern. These subtle variations would be hard to reproduce through current flow control techniques. Figures courtesy of (Caro C.G. 1978).

The pulsatile nature of blood flow creates a dynamic environment that raises many interesting and fundamental fluid mechanic questions. The answer to these questions may hold the key to understanding the disease allowing the development of better targeted treatments. It is vital to accurately simulate the pulsatile nature of blood flow when examining the fluid mechanics associated with physiological conditions as unusual hemodynamic conditions create an abnormal biological response.

A limiting factor for expanding our knowledge has been the absence of a flow control technique and a flow control system, capable of producing accurate complex flows, specifically for microchannel based physiological experiments. This relationship is highlighted by the flowchart presented in figure 1.4. To develop effective treatments the chemical and mechanical processes must be investigated. The effect of mechanical processes of diseases has been the less investigated pathway. The development of a new flow control technique will enable in-vitro experiments which can replicate in-vivo hemodynamic conditions. This would lead to increased understanding of these processes and ultimately the development of effective treatments.

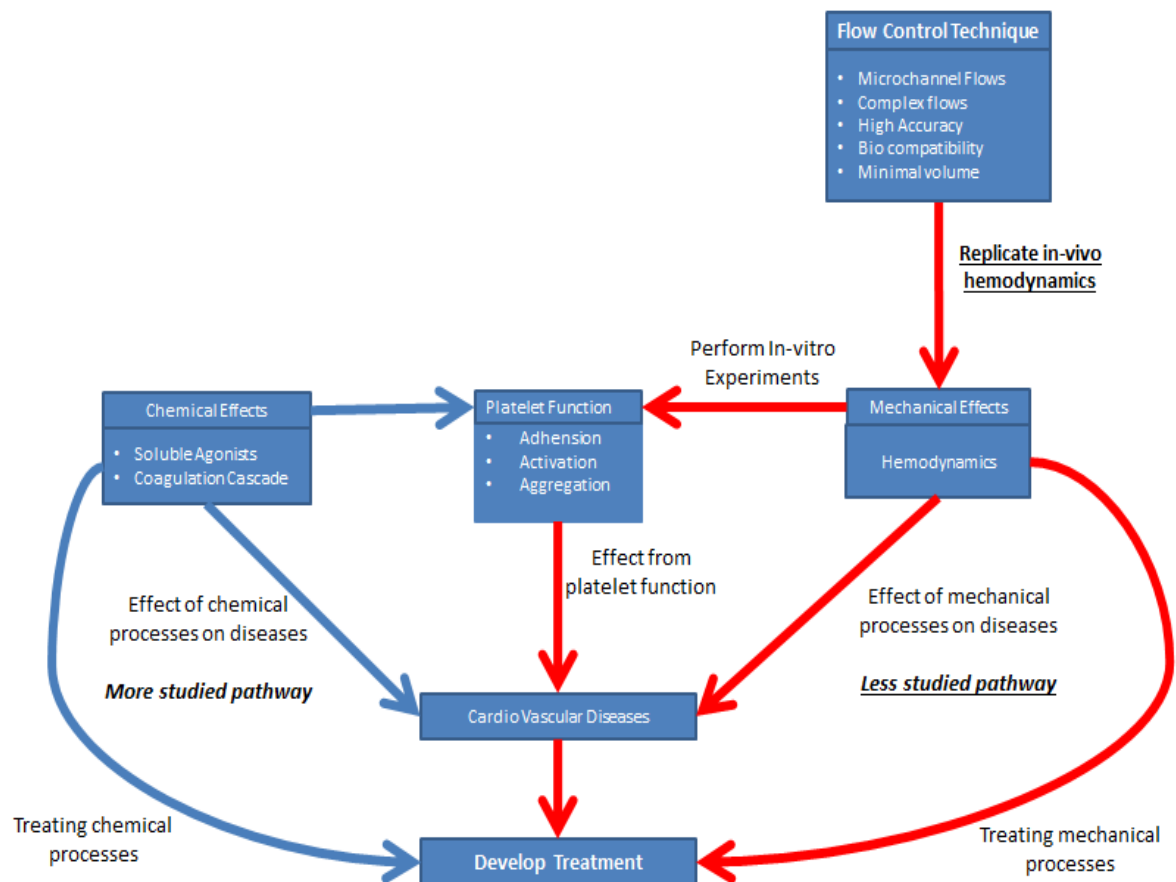


**Figure 1.4** Flowchart demonstrating the significance of developing a new flow control technique. It will enable in-vitro experiments which can replicate in-vivo hemodynamic conditions leading to better understanding of these processes and ultimately towards development of effective treatments.

Current systems lack the ability to produce accurate complex flows for microchannel based physiological experiments. They are limited in flow scalability and operational range. Some systems cause undesired cavitation and blood trauma by damaging suspended particles and their cell membranes. Without the regenerative properties of the human body the cells are not replaced. This in turn may generate abnormal result. Therefore a new system should be developed which is real time and completely biocompatible suited for microchannel based physiological experiments.

## 1.2 Aims

The aims of this thesis are as follows

### 1.2.1 Primary Aims

1. Produce a new flow control technique for microchannel based physiological flow experiments. Minimum system specifications are:

- a. Microchannel Flows

Production of controlled flow between 0 - 5 ml/min. This corresponds to a shear rate of  $0 - 6225 \text{ s}^{-1}$  when generated within a microchannel of 0.2 mm x 2 mm rectangular cross section. This shear rate range is based on hemodynamics experienced by the human body (*Bluestien et al. 1997, Long et al. 2005*). Shear rates within this range are used for experimental work on hemodynamic flow, thrombus formation and platelet aggregation (*Tolouei, E. et al., 2001, Nesbitt et al. 2009*).

- b. Complex waveform generation

Able to produce any complex waveform within the operational flow, shear and frequency range. Frequency range is between 0 - 3 Hz corresponding to 0 - 180 beats per minute.

- c. High accuracy

Achieve a maximum steady flow error of 2% and a maximum root mean square error of 10% for complex flows.

- d. Bio compatibility

The technique must cause minimal blood trauma during pumping

- e. Minimal volume

Human blood is a limited resource. Therefore the technique must achieve 100% utilization of fluid. In blood experiments buffer fluids are used to protect blood from external conditions. Rotational pumping mechanisms require a pump cavity to be pre-filled with a buffer fluid or blood to prevent cavitation. This restricts the minimum amount of fluid required for operation. Due to fluid mechanic properties of rotating systems, blood could get diluted with buffer fluids rendering it unsuitable for experiments.

2. Design a prototype of a functional flow control system for microchannel based physiological flow studies based on this technique.

### 1.2.2 Secondary Aims

1. Demonstrate the flow control techniques ability to accurately replicate physiological pulsatile flow conditions
2. Illustrate the importance of pulsatile flow by producing distinguishable thrombus growth results through sample experiments under steady and pulsatile flow.

In the next three chapters the pump design, flow evaluation and thrombus growth experiments are presented. Each section has its own background literature, experimental results, discussion and conclusion. The final chapter concludes the thesis by presenting further recommendations and major findings of this thesis.

## 2.0 Flow Control Technique & Prototype Design

This chapter presents the new flow control technique and the developed prototype system. The functionality and detailed description of its hardware and software components are described. Qualitative evaluations of the current flow control techniques have been completed. Performance test results completed for the prototype support its ability to improve upon existing systems and demonstrate its capabilities for microchannel based physiological flow studies.

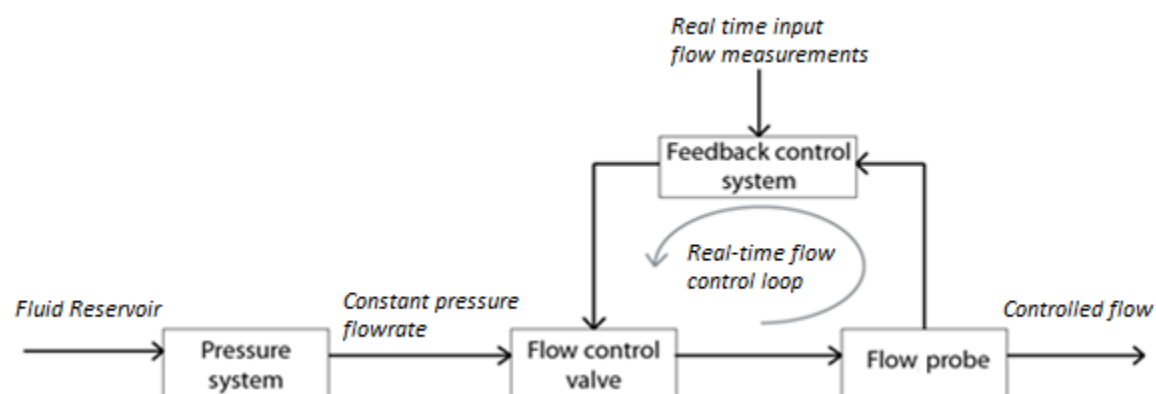


**Figure 2.1** Block diagram of the flow control technique. The pressure system provides the required constant base flow rate. The flow control valve provides finer control over the base flow. The feedback control system directs the fluid control valve according to the desired flow rates. The flow probe measures the output flow rate of the flow control system and sends this reading to the feedback control system.

Figure 2.1 presents a block diagram of the developed flow control technique. It consists of four main systems. The pressure system provides the pressure head to drive the required constant base flow rate. A flow control valve provides finer control over the flow. The feedback control system directs the fluid control valve according to the desired flow rates. The flow probe measures the current output flow rate of the flow control system and sends this reading to the feedback control system. The strength of this technique is in its scalability, the concepts can be adopted to suit multiple flow applications limited only by the physical capabilities of the hardware used. For example, the prototype flow control system is able to accept real time flow measurements and control the output flow at high accuracy with a lag of 0.07s. If a faster control valve is substituted the temporal accuracy can be further improved.

### 2.1 Background Literature

Qualitative looks at current flow techniques and systems have been completed. Design theory for each prototype system component is discussed in this section. Currently, there are several flow control system designs capable of producing complex flows. However, these designs are not practical as their flow production regimes are simply too large to be used for microchannel based physiological

experiments. Scaled versions of these systems will lack flow resolution. Commercial micro pump designs only produce steady flow or highly constrained pulsatile flows.

Generally, only small quantities (<500 ml) of blood are available for experimental use and it is desirable to minimize wastage. An ideal flow system needs to be biochemically compatible, operate with a minimum quantity of biological fluid and low operating shear to minimize blood damage. Disposability would be an advantage as it eliminates blood clotting and enables faster cleaning between experimental runs. Clot formation is unacceptable as it would alter both the flow and biological signaling.

### 2.1.1 Pump Systems

The majority of existing fluid delivery systems consist of a single or dual pump setup with or without feedback control. Blood pumps are designed as part of a cardiovascular model or as a ventricular assist devices. Numerous pumping systems have been developed encompassing a wide range of specifications, operating parameters and levels of optimisation. The different classes of available pumps and their suitability for microchannel based experiments is discussed through the subsequent sections.

#### *Gear Pumps*

Gear pumps are simple in construction. Figure 2.2 shows a basic gear pump design. The two meshing gears rotate in opposite direction. The fluid that fills the space is bounded by two successive gear teeth and the case. Then it follows the teeth rotation gets pushed out. Gear pumps are attractive due to their ability to produce steady flow and for the proportional relationship between rotational speed and output flow rate. However, they physically damage suspended particle in the working fluid by exerting high stresses during gear rotation (*Petersen 1984; Hoskins et al. 1989; Wong et al. 2008; Plewes et al. 1995*). They have a large dead volume and are prone to gear locking vibrations. They are classified as positive displacement pumps. Positive displacement pumps are insensitive to back pressure requiring constant monitoring of over pressure to prevent bursting. Therefore, this system would not be suitable for an application that requires pressure to be maintained.

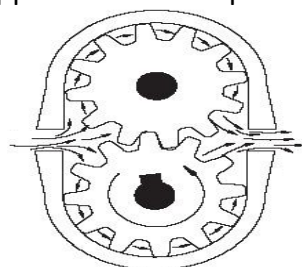


**Figure 2.2** Simple gear pump design consisting two spur gears meshing together and revolving in opposite directions within a casing. Any liquid that fills the space bounded by two successive gear teeth and the case must follow along with the teeth as they revolve. Figure courtesy of (Netpumps 2010).

## Impeller Pumps

The advantage of using an impeller pump is its well established design scheme. Although control of an impeller pump is slightly more complicated than a positive displacement pump, it allows for control of pressure. Impeller blades in these types of pumps have shown to cause hemolysis (K. X. Qian 1990). It is possible to carefully design a pump which has low internal shear stresses for a specified operational flow range (Masahiro *et al.*, 2004). However, a new impeller pump would have to be designed each time a different operational flow range or pattern is required. This makes impeller pumps impractical for laboratory experiments. These pumps are widely used in ventricular assist devices where the body's regenerative process offsets blood damage from the pump. Figure 2.3 shows a cross-sectional view of an impeller pump. The figure shows the velocity field and vector field through the pump impeller diffuser and housing. Impeller pumps reduce thrombus formation within the pump by reducing regions of stagnation, turbulent shear stress or flow recirculation. This is evident through the vector field in figure 2.3. Qian (1990) showed thrombus formation could be reduced by developing impellers according to the stream surfaces. They developed an impellers shroud and vane according to stream surfaces by solving the partial differential equations of continuity, motion and energy. The pump surface fully rinsed by non-turbulent flow was thrombus free and caused low hemolysis (K. X. Qian 1990).

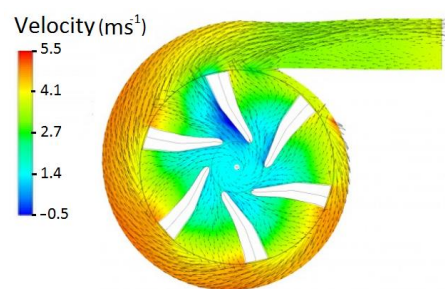


**Figure 2.3** Cross-sectional view through an impeller pump. Vector field indicating flow through the pump impeller, diffuser and housing. Reduction of flow stagnation reduces unwanted thrombus formation within the pump. Figure courtesy of (Enmodes 2012)

## Metering Pump

Metering pump models use an actuated piston to develop pulsatile flow. Figure 2.4 shows a cross-sectional view of a piston metering pump. The inlet and outlet valves interchange allowing for fluid flow. During the suction phase, fluid enters the pump through the inlet valve. The outlet valve stops any backflow to the metering pump. During the discharge phase, fluid is forced out through the outlet valve. Varying the volume of air can alter velocity and pulse characteristics (Greaby *et al.* 2007). These pumps are incapable of developing steady flow and complex flows.

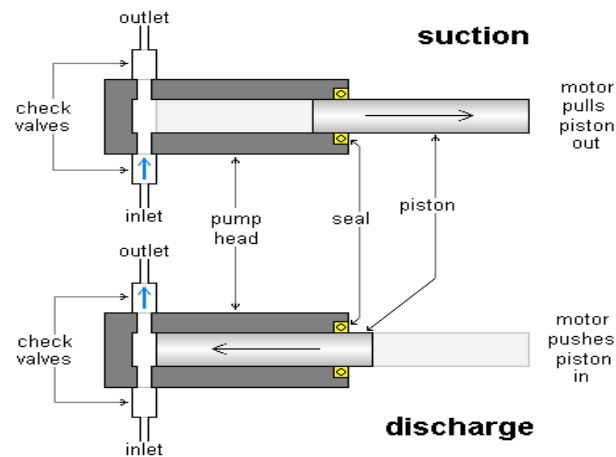


**Figure 2.4** Cross-sectional view of a piston metering pump. The discharge and suction valve interchange allowing for fluid flow. Blue arrows indicate direction of flow. Figure courtesy of (H Padleckas 2006).

### Axial flow pumps

Axial flow pumps are commonly used as ventricular assist devices. Figure 2.5 shows a screw pump design with a flow straightener, flow inducer and a diffuser that was designed by Dabakey (1999). The pump was of size of an AA battery but was capable of delivering very high flow rates. This design incapable of producing complex waveforms (DeBaakey 1999).



**Figure 2.5** CAD model of an axial flow blood pump designed by Debaakey (1999). Figure courtesy of (RWTH Aachen University 2010).

A pulsatile pump model consisting of an axial flow pump moving axially along the flow by an external actuator was designed by Qian et al. (2001). This model produced low hemolysis and pulsatile flow with no back flow. This design was incapable of producing constant flow (K. Qian et al. 2001).

### Peristaltic Pumps

Peristaltic or roller pump designs have minimum moving parts and only the rolled tube is in contact with blood. Figure 2.6 shows a side view of a typical peristaltic pump mechanism. The pumping mechanism invokes rotating rollers squeezing the blood carrying tube to discharge the fluid. The low impact pumping method cause low hemolysis (Douville et al. 1983; Law et al. 1987; Iijima & Salerno 1965). Smoothness of the tube material, tube diameter, flow velocity and rotation



frequency have been shown to be factors affecting hemolysis in a roller pump (Borgstrom *et al.* 1981). Peristaltic pumps generally produce a pulsatile output at constant rotational speed. A Modified peristaltic pump with adjustable screws has been shown to generate carotid waveforms (Douville *et al.* 1983). The inability to generate accurate steady flow and flexibility to generate complex waveforms are the primary drawback for this design.

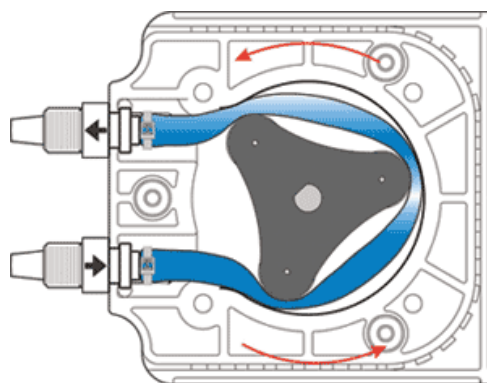


**Figure 2.6** Side view of a peristaltic pump mechanism. The rotating roller squeezes the blood containing tube to discharge the fluid. The system is highly bio compatible but produces a pulsatile flow error and incapable of generating complex flows. Figure courtesy of (Robin Gledhill 2011).

### *Piston & Cam Pump*

Many researchers have attempted to design cam and piston driven pump systems. Figure 2.7 shows a common piston pump design. The system draws liquid into the cylinder through the suction valve during the suction stroke and forces liquid out through the discharge valve at high pressure during the discharge stroke. Cam driven systems produce complex waveforms by combining their harmonics using a series of sinusoidal waveforms with different frequencies. Unfortunately, if a different waveform is required the pistons needed to be individually adjusted for amplitude and phase (Kiyose *et al.* 1977). Further, these systems were unable to produce constant flow and lacks the accuracy and the flexibility to produce complex waveforms observed in vivo (Reul *et al.* 1974; Hoppmann & Liu 1972; Calil & Roberts 1985; Kiyose *et al.* 1977; Law *et al.* 1987; Werneck *et al.* 1984).

Several variations of piston pumps were able to get around these difficulties. One such design incorporated a micro stepper driven dual piston cylinder where one piston would refill while the other infuses. When the end of the cylinder is reached the refill cylinder becomes the infuse cylinder while the infuse cylinder becomes the refill cylinder (Holdsworth *et al.* 1991). An improvement was made to Holdsworth's design by replacing the dual cylinder by a single cylinder divided with a bi-directional spool (Frayne *et al.* 1992). These improvements addressed the issues faced by conventional cam and piston driven systems. However, both systems produced flow disruptions at the point where the pistons or the spool would change direction (Frayne *et al.* 1992; Holdsworth *et al.* 1991).

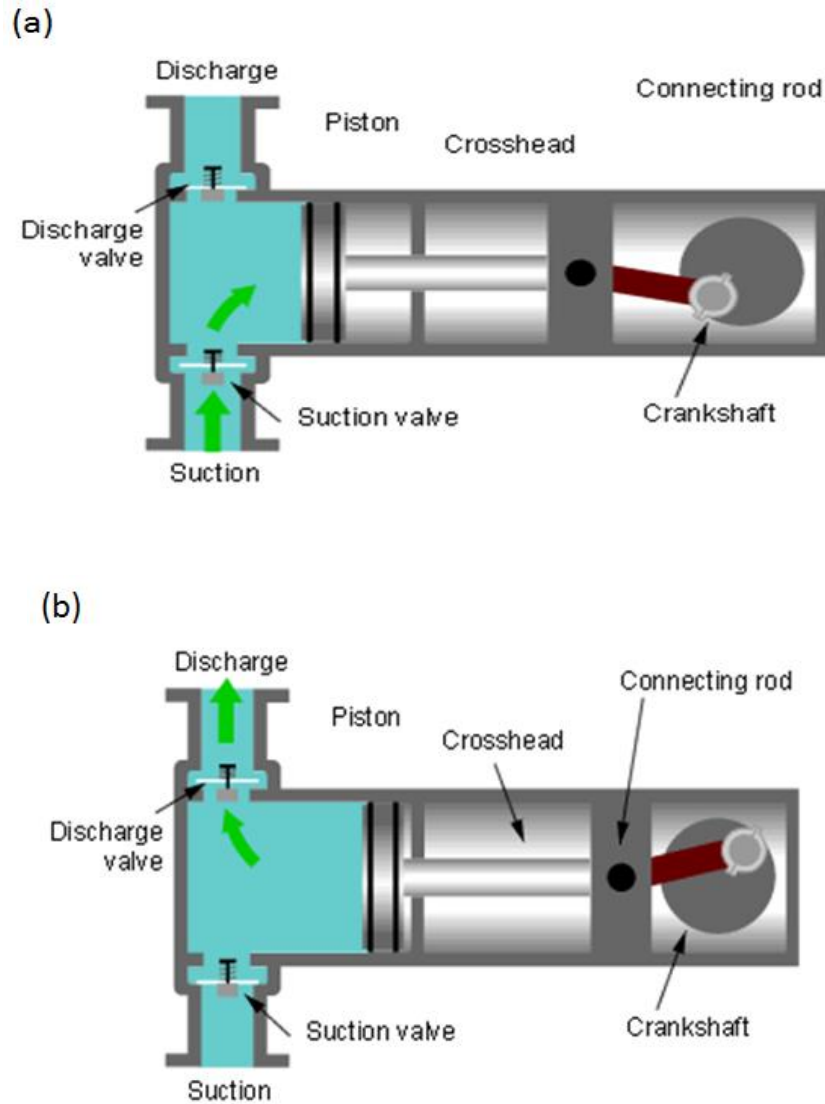


**Figure 2.7** Common piston pump design. (a) The system draws liquid into the cylinder through the suction valve on the suction stroke (b) The system forces liquid out through the discharge valve at high pressure during the discharge stroke. Figure courtesy of (Flexible Learning 2008).

### Cavity Pump

Progressive cavity pumps are suitable for pumping sensitive liquids such as blood. However they are difficult to construct and produce errors at low flow rates with back pressure (Eriksson *et al.* 2000). Figure 2.8 shows a progressive cavity pump designed by Eriksson *et al.* (2000). The pump consists of a rotor connected to a motor and an elastomer based stator as the cavity. During rotation the rotor forces the liquid forward through its cavity. This pumping mechanism is less stressful on suspended particles. High precision is required for good sealing and to avoid interference with rotational parts.

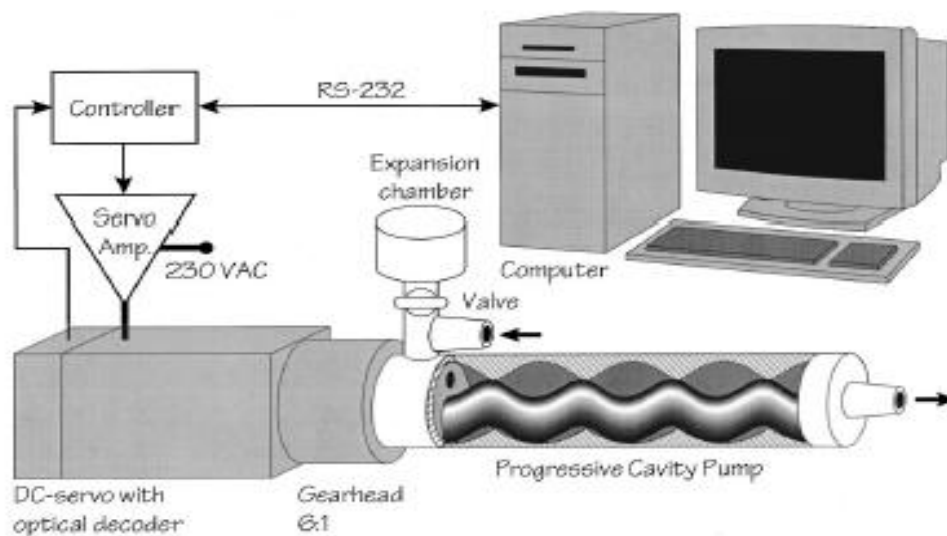


**Figure 2.8** Progressive cavity pump designed by Eriksson et al. (2000). The pump consists of a rotor connected to a motor and an elastomer based stator as the cavity. High precision is required for good sealing and to avoid interference of rotational parts. Figure courtesy of (Eriksson et al. 2000).

### Servo Controlled



**Figure 2.9** Servo controlled syringe pump system. These systems show promising results to produce complex flows. However they have shown to produce undesired oscillatory components. Figure courtesy of (Analytik Jena 2012).

Servo controlled hydraulic systems to provide pulsatile component have been developed since 1970s. Figure 2.9 shows a servo controlled spool driven syringe pump system. These systems were able to generate matching flow pulses to physiologically important flow waveforms. It was shown that syringe pumps exhibit undesired oscillatory components (Tolouei et al. 2011). Adapting these systems for the small scale flow regimes would require highly complex construction and is expected to perform poorly in terms of accuracy (Pitts & Dewey 1975).

### Dual Pump systems

Dual pump systems have been designed to overcome individual pump system drawbacks. Figure 2.10 shows one such design consisting of a gear pump to generate the mean component and a piston pump to generate the oscillatory component (Tsai & Savas 2010). Several researchers combined a peristaltic pump to produce steady flow and a piston or a cam driven syringe pump to super impose the pulsatile component (Conklin et al. 2000; Hein & Obrien 1992; Law et al. 1987; Krane 2006). Even with this arrangement high frequency flow responses are difficult to achieve.

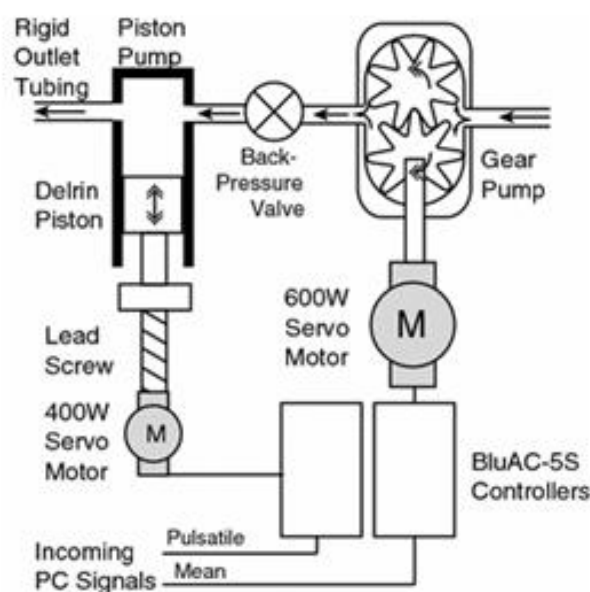


**Figure 2.10** Dual pump system. A gear pump was used to produce the base flow followed by a piston pump to produce the oscillatory component. The system exhibited low accuracy. Figure courtesy of (Tsai & Savas 2010)

### Pumping mechanisms summary

As summarised in table 2.1, it is clear that none of the existing systems are capable of producing both steady and complex micro flows at high accuracy. Gear and impeller pumps cause hemolysis. Piston, cam driven, peristaltic pumps require modifications each time a change in waveform is required. Axial and cavity pumps are hard to construct and lacks the accuracy when scaled down to micro flow rates. Dual pump systems also showed low accuracy in waveform production.

In a majority of these designs, feedback control systems were not utilised. Systems that did use a feedback control showed an increase in performance compared to the standard systems (Plewes et al. 1995; Wong et al. 2008). Several researches suggested that improved system performance would have been realised if a feedback control system was incorporated to their designs (Conklin et al. 2000; Tsai & Savas 2010). As well as improving accuracy, the feedback control system is essential to realize real time flow control.

Legend X - No existing system Y - Existing system capable	Able to develop micro flow rates (0-20 mL/min)	Able to produce steady flow	Able to produce Complex flows	Maintain high flow Accuracy ( >5% steady flow error, >10% RMS for complex flows)	Completely Bio-compatible	Minimal working fluid (>10 mL)
Gear pump	X	X	Y	Y	X	X
Impeller pump	X	X	Y	Y	X	X
Metering pump	Y	X	X	X	X	Y
Axial flow pump	X	Y	Y	Y	Y	Y
Peristaltic pump	Y	X	Y	X	Y	Y
Piston & cam pump	Y	X	Y	Y	Y	Y
Cavity pump	X	Y	Y	Y	Y	Y
Servo controlled pump	Y	X	Y	Y	Y	Y
Dual pump system	X	X	Y	Y	X	X
Developed flow control technique	Y	Y	Y	Y	Y	Y

**Table 2.1** Table summarising currently available pump systems and their capabilities. Notation “X” indicates that current systems are incapable of meeting this requirement. Notation “Y” indicates that a design exists that is capable of this meeting this requirement. None of the existing systems are capable of producing both steady and complex micro flows at high accuracy.

### 2.1.2 Flow probe designs

To provide flow rate measurements to the feedback control system a custom flow probe was designed. Several flow measuring principals and flow probe designs were considered. Many current flow meters and probes lack the response rate desired for high frequency applications or are very expensive. A typical ultrasonic flow meter is a bulky piece of equipment requiring a large footprint. Therefore, we designed a blood flow measuring device that is highly responsive, sterile, disposable, low cost in operation and small in physical dimension.

The most common principals for fluid flow metering are as follows

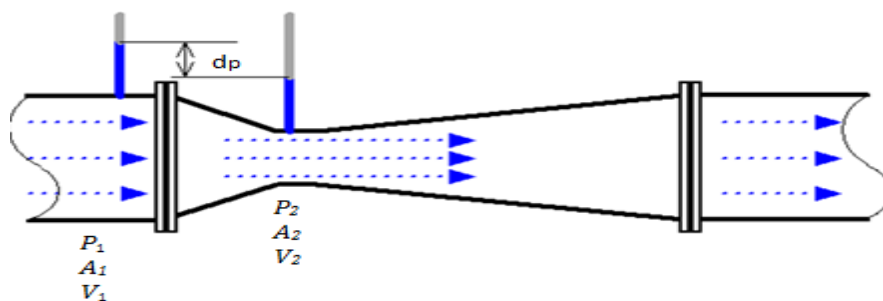
- Differential pressure flow meters
- Velocity flow meters
- Positive displacement flow meters
- Mass flow meters

We will now review these fluid flow measuring principles.

## Differential pressure

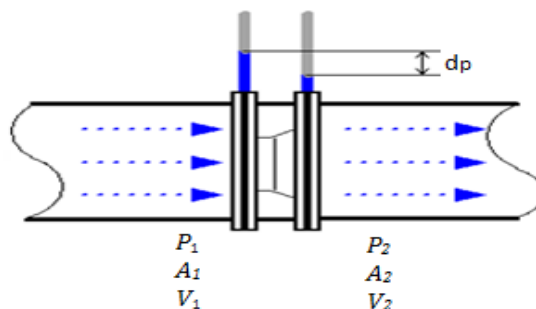
Differential pressure flow meters measure flow based on the Bernoulli's principle. The most commonly used differential pressure flow meters are venturi and orifice meters. These are easy and cheap to construct and shown to produce accurate results. With advances in pressure transducer electronics even subtle changes in flow can be measured accurately. In both venturi and orifice meters, the pressure drop is measured across a restriction. Using the Bernoulli's principle we can relate this pressure drop to the flow velocity. This relationship is established as the calibration equation for the flow meter.

Figure 2.11 shows a cross-sectional view of a venturi meter. In the venturi flow meter, the measurable pressure difference is created by gradually restricting the flow path. The flow is then allowed to travel through a longer expanding path allowing the pressure to be recovered.



**Figure 2.11** Cross-sectional view of a venturi meter. The measurable pressure difference is created by gradually restricting the flow path. The flow is then allowed to travel through a longer expanding path allowing the pressure to be recovered. Figure Courtesy of (Engineeringtoolbox 2009).

Figure 2.12 shows a cross-sectional view of an orifice meter. In the orifice flow meter, flow travels through a sudden restriction. The accuracy depends on the orifice meters physical finish, especially having a sharp edge to the upstream side. Wear reduces the accuracy of the orifice meter. They are simpler to produce than a venturi flow meters and can be produced for almost any application and in any build material.



**Figure 2.12** Cross-sectional view of an orifice meter. Figure courtesy of (Engineeringtoolbox 2009). Flow is allowed to travel through a sudden restriction creating a pressure differential.

### *Velocity meters*

In a velocity flow meter the flow is calculated by measuring the speed in one or more points in along flow and integrating the flow speed over the flow area (*Engineeringtoolbox 2009*). Ultrasonic meters are one of the most popular forms of velocity flow meters. They operate according to the principles observed by Christian Johann Doppler. When a fluid moves towards a transducer, the frequency of the returning signal will increase. As fluid moves away from a transducer, the frequency of the returning signal decreases. The originating frequency is the frequency at which the ultrasonic wave was emitted from the source. The returning frequency is the frequency at which the emitted wave returns to the source. The frequency difference is equal to the returning frequency minus the originating frequency and this can be used to calculate the fluid flow speed (*Engineeringtoolbox 2009*).

### *Positive Displacement Flow meter*

A positive displacement flow meter measures fluid flow using precision fitted rotors as flow measuring elements. The rotational displacement is calibrated to the volume of fluid displaced. These meters are often connected to an integral electronic pulse transmitter where rotations are converted to volume and flow rate.

### *Mass Flow meters*

Mass meters measure the mass flow rate directly. The most popular method is to use thermal mass flow. These operate independently of density, pressure, and viscosity. It uses a heating element to heat the flow. A heating sensor downstream measures the heat. The conducted heat is directly proportional to the mass flow rate. The temperature difference is calibrated to give the mass flow rate. Therefore accuracy of the device depends on the calibration process. Variations in temperature, pressure, flow rate, heat capacity and viscosity of the fluid affects accuracy of the calibration process (*Engineeringtoolbox 2009*).

### *Flow probe model selection*

Venturi and Orifice meters are the most suited for this application. Ultrasound source and measuring electronics are excessively expensive. Thermal flow meter designs would affect blood properties and are too costly for a disposable design. Mass flow meters would be impractical for low flow applications as they require a large working volume. Flow measurements through differential pressure, is a proven technique offering simplicity of design and flexibility of scaling. Advances in cost effective 3D printing with bio-compatible material allows for disposability.

A similar venturi style flow meter was designed to measure automotive engine intake by Beaulieu et al. (2011). The flow regimes for this model were much higher at around 6000 ml/min compared to 0 to 5 ml/min for microchannel blood flows (Beaulieu et al. 2011). This microchannel flow range limited the selection of pressure transducers as the corresponding pressure drop over the constriction was 0 – 350 mbar. To reduce noise signal, filtering was required. For testing purposes both

venturi and orifice style flow meters were designed. The venturi style meters showed poor quality results due to manufacturing flaws. It showed poor results in repeatability. The orifice style flow meter on the other hand showed good functionality and accuracy. Therefore the orifice design was selected as the preferred flow probe model.

### Governing Equations

Both venturi and orifice meters are designed based on Bernoulli and continuity principles as expressed in equation (1) and (2).

Where the quantities can be defined as below with reference to figure 2.11 and 2.12.

$P_1$	Upstream pressure	$P_2$	Downstream pressure
$A_1$	Upstream cross sectional area	$A_2$	Downstream cross sectional area
$V_1$	Upstream flow velocity	$V_2$	Downstream flow velocity
$Q$	Fluid flow rate	$\rho$	Fluid density

Assuming flow is horizontal

$$P_1 + \frac{1}{2}\rho V_1^2 = P_2 + \frac{1}{2}\rho V_2^2 \quad (1)$$

Assuming steady and uniform, flow continuity can be expressed as equation (2).

$$Q = V_1 A_1 = V_2 A_2 \quad (2)$$

Assuming  $A_2 < A_1$  Combining (1) and (2),

$$Q = A_2 [2(P_1 - P_2)/\rho(1 - (A_2/A_1)^2)]^{\frac{1}{2}} \quad (3)$$

### 2.1.3 Feedback control system

A real time flow control system requires constant monitoring, comparison and adjustment of flow rate. Research has shown that flow models with feedback systems and control strategies provided improved waveform accuracy (*Plewes et al. 1995; Wong et al. 2008*). For the current model control system will be driven by a PID control loop. A signal filtering strategy will be implemented to reduce undesired signal noise.



### PID algorithms governing equations

The PID algorithm is one of the most successfully used control algorithms. It is a robust and easily programmable allowing for excellent control performance under dynamic environments. The performance of the PID controller depends on its tuning parameters. The extent of tuning is subjected to the desired performance level of transient and steady-state response.

The ideal PID algorithm can be described as

$$u(t) = K_p e(t) + K_i \int_0^t e(\tau) d\tau + K_d \frac{d}{dt} e(t) \quad (4)$$

Where the algorithm variables are defined as,

$t$	Instantaneous time	$e(t)$	Flow error
$u(t)$	Desired flow	$y(t)$	Controlled flow
$K_d$	Derivative gain	$K_d \frac{d}{dt} e(t)$	Differential term
$K_i$	Integral gain	$K_i \int_0^t e(\tau) d\tau$	Integral term
$K_p$	Proportional gain	$K_p e(t)$	Proportional term
$T_i$	Integral time	$T_d$	Differential time

The flow error  $e(t)$  is the difference between the desired flow  $u(t)$  and the controlled or output flow  $y(t)$ . The proportional term  $K_p e(t)$  produces an output response proportional to the error term. The integral term  $K_i \int_0^t e(\tau) d\tau$  produces an output response by summing the flow error over time. The derivative term  $K_d \frac{d}{dt} e(t)$  produces a response proportional to the rate of change of controlled flow. The proportional gain is related to the integral and differential gains with equations (5) and (6). The integral time ( $T_i$ ) and the differential time ( $T_d$ ) are related to each other with equation (7)

$$K_i = \frac{K_p}{T_i} \quad (5)$$

$$K_d = K_p T_d \quad (6)$$

$$T_d = \frac{T_i}{4} \quad (7)$$

Substituting equations (5) and (6) to (4) gives the standard PID form.

$$u(t) = K_p \left[ e(t) + \frac{1}{T_i} \int_0^t e(\tau) d\tau + T_d \frac{d}{dt} e(t) \right] \quad (8)$$

A change in any one of the PID gains results in a change of overall system response. Table 2.2 shows the effect each gain has on rise or fall time (which is the time taken to change an output from a set value to another specified value), steady state error, stability and settling time when they are independently increased. By increasing the

proportional gain higher rise or fall time is decreased. But a steady state error always exists. Integral gain can minimize steady state error but reduces transient response time due to increase in settling time. Deferential gain can improve the transient response and system stability.

PID gain	Rise/fall time	Steady-state error	Stability	Settling time
$K_p$	Major decrease	Minor decreases	Moderate decrease	Moderate decrease
$K_i$	Moderate decrease	Major decrease	Major decrease	Major decrease
$K_d$	Minor increase	No effect	Moderate increase	Moderate increase

**Table 2.2** Change in response of the control system for independent increase of a PID gain

The transfer function block diagram for the proposed PID algorithm is shown in figure 2.13. The PID gain variables are identical to quantities described for equation (4). The additional variables are described below.

$V_r(t)$	External real time flow voltage measurements
$u_d(t)$	Digitally stored flow measurements
$V_{PID}(t)$	Variable voltage for valve control
$y_{fb}(t)$	Feedback flow measurements
$V_{fb}(t)$	Feedback flow voltage measurements
$V_{fb}(t)$	Feedback flow voltage measurements

The controller input  $u(t)$  is the desired flow. Desired flow can be either from real time flow measurements  $V_r(t)$  or digitally stored flow measurements  $u_d(t)$ . Feedback voltage ( $V_{fb}(t)$ ) is filtered and converted to feedback flow  $y_{fb}(t)$ . The flow error  $e(t)$  is calculated between the desired flow and the feedback flow  $y_{fb}(t)$ . The PID algorithm calculates the gains as per equation (4) and produces a variable voltage  $V_{PID}(t)$  to control the velocity of the fluid control valve. The fluid control valve pinches the flow carrying silicone tube producing controlled flow  $y(t)$ .

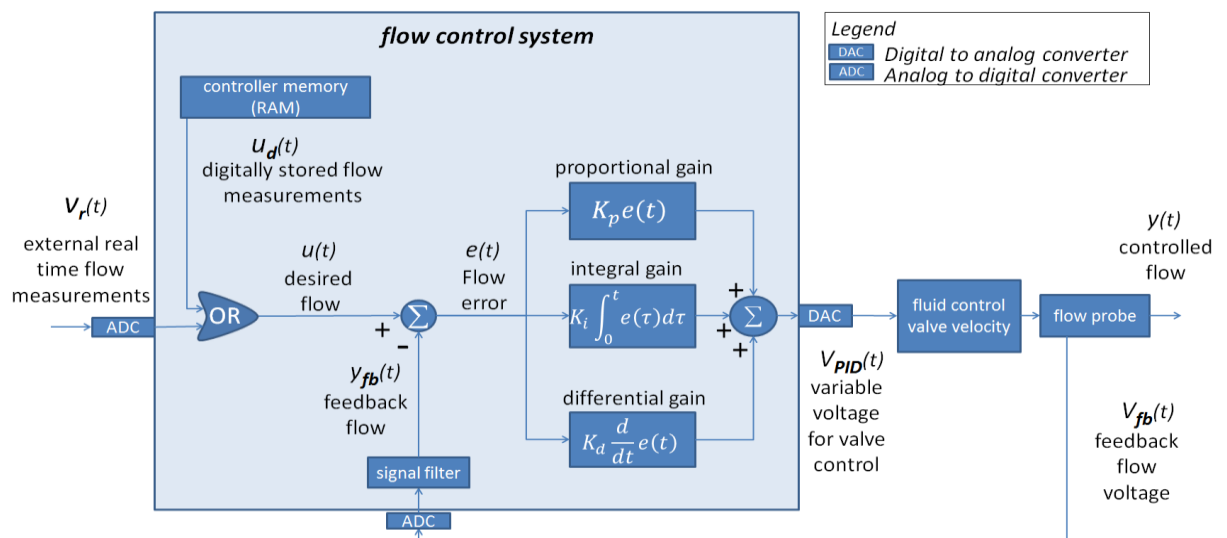


**Figure 2.13** The transfer function block diagram for the proposed PID algorithm.

## Signal filtering & governing equations

In the flow meter the high-resolution differential pressure transducer produces instabilities for noise and vibration in the system. To address this issue a fast and effective Savitzky–Golay smoothing filter was used. This filtering method allows for eliminating vibrational noise while preserving the differential pressure signal.

For a noisy signal the simplest form of averaging filter would involve performing a least squares fit of a small set of consecutive data points to a polynomial, then taking the calculated central point of the fitted polynomial curve as the new smoothed data point. The Savitzky–Golay smoothing filter uses an improved algorithm whereby a set of integers  $(A_{-n}, A_{-(n-1)} \dots, A_{n-1}, A_n)$  known as convolution integers are derived and used as weighting coefficients to carry out the smoothing operation (Savitzky & Golay 1964). The convolution integers are equivalent to the polynomial method but are computationally more efficient. It is far less aggressive than a moving average algorithm as it preserves vital information.

The smoothed data point  $(y_k)_s$  can be related to the the Savitzky-Golay algorithm by equation (9). Where  $A_i$  is the weighting coefficient and  $n$  is the number of data points

$$(y_k)_s = \frac{\sum_{i=-n}^n A_i y_{k+i}}{\sum_{i=-n}^n A_i} \quad (9)$$

## 2.2 Prototype system

The prototype flow control system achieves the desired flow by producing a constant base flow using an air pressure system and allowing finer control of this flow with a feedback controlled flow control valve. Figure 2.14 presents a schematic diagram of the prototype flow control system.

The system consists of a main pressure box and a damper box which are pressurised by a micro diaphragm air pump. The main pressure box contains the majority of the system air volume. The damper pressure box is positioned in between the pressure box and the air pump to eliminate pressure waves from the diaphragm mechanism.

The main pressure box is regulated from the bleed valve. The air pressure of the system is measured by a 350 mbar rated differential pressure sensor. Initially, the outlet valve is restricted allowing for pressure build up at the main pressure box. Once the desired pressure is achieved the airflow line to the fluid control reservoir is unrestricted. This causes the reservoir to be pressurised driving the fluid out. Peripheral hardware of the pressure system is managed by PIC microprocessors. Software integration with the PIC processors were achieved through a National instruments interface card and a custom Labview interface. All airflow lines are connected with 1/8 inch silicone tubing. The fluid expelled out from the reservoir is controlled by a flow control valve. The flow rate is measured by the flow probe. The

feedback flow rate measured from the flow probe is sent to the feedback control system which then signals the control valve to adjust the flow. Detailed description of hardware and software design is presented for the four main components in the system. These are the pressure system, flow probe, fluid control valve and the feedback control system.

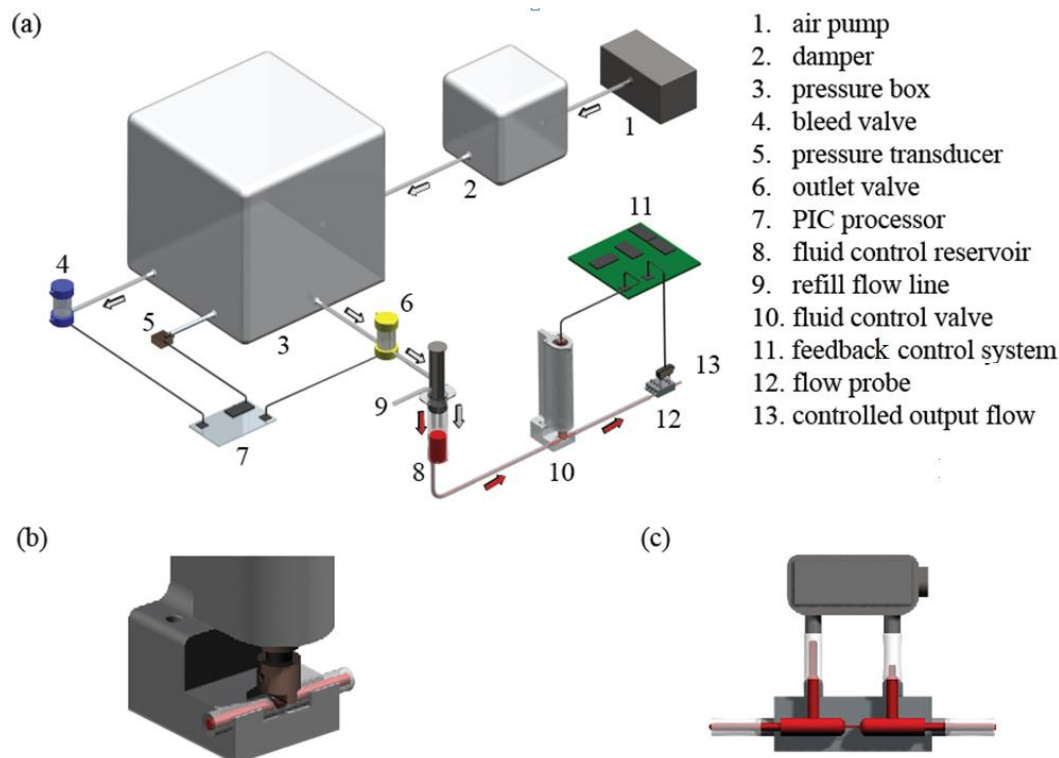


**Figure 2.14** Schematic diagram of (a) the prototype flow control system. The desired flow rate is achieved by producing a constant base flow using an air pressure system and providing finer control of this flow with a feedback controlled flow control valve. Pressure levels are sustained through a micro air pump, pressure box, pressure sensor, outlet valve and a bleed valve. The fluid is contained in a modified syringe with air and fluid access through the plunger side. (b) Expanded view of the fluid control valve. The linear actuator is enclosed in an aluminium housing. The plunger is attached to the tip of the actuator. 1/32 inch tubing sits on a groove of the tube block. The tube block slides into the control valve slot. (c) Cross section of the 3D printed four channel flow probe with a pressure transducer and latex tubing attached to 0.5 mm orifice diameter channel

### 2.2.1 Pressure system

Figure 2.15 shows the schematic diagram of the pressure pump system. The pressure system functions by pressurizing and maintaining a pressure box (3) at constant pressure. Once the desired pressure is achieved the airflow line (6) to the fluid reservoir (8) is unrestricted, causing the reservoir to be pressurised driving the fluid out. The pressure in the pressure box is maintained by supplying air from air pump (1) and maintaining the desired pressure through a bleed valve (4), pressure sensor (5) and control hardware (7). The damper box (2) eliminates pressure pulses from the air pump

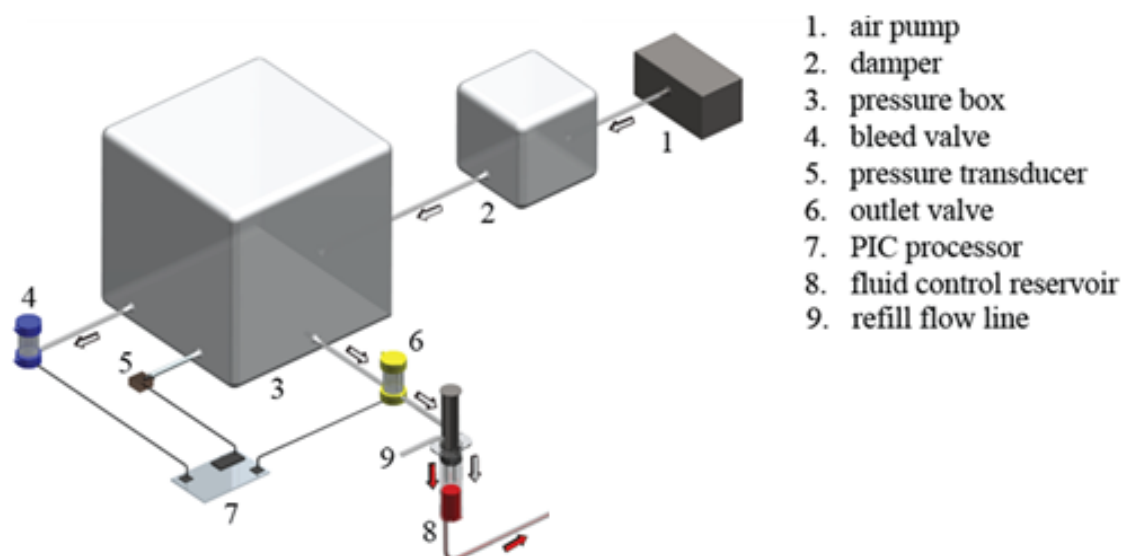


**Figure 2.15** Schematic diagram of the pressure pump system. Desired constant fluid flow rate is generated by maintaining constant air pressure of the pressure box. Pressure levels are sustained through a micro air pump, pressure sensor, proportional bleed air valve and control hardware. The fluid is contained in a modified syringe with an air access through the plunger side.

#### Air pump



**Figure 2.16** Micro diaphragm air pump (KNF, NMP 830 KNDC 12V) which provides the supply air to pressurize the flow control loop

Figure 2.16 shows the KNF NMP 830 KNDC 12V micro diaphragm air pump that provides the supply air to pressurize the flow control loop. The diaphragm pumping mechanism introduces undesired pressure pulsation to the system. To eliminate pulsations an intermediate damper box is placed in between the pump and the main pressure box. For more condition sensitive blood applications the air pump could be replaced with nitrogen or other suitable inactive gas cylinder.

### *Damper boxes*

The damper is positioned in between the pressure box and the air pump to eliminate pressure waves from the diaphragm mechanism of the air pump. The box is rated for 500 mbar of pressure and 3D printed from Object Fullcure 7020 material by Formero, Australia. The two built in 1/8 inch inlet and outlet barbs allow for air exchange. The damper box dimensions are 0.05 m x 0.05 m x 0.05 m.

### *Pressure Box*

The pressure box contains the majority of the air volume. The box is rated for 500 mbar of pressure and 3D printed from Object Fullcure 7020 material by Formero, Australia. Figure 2.17 shows the 3D printed box with tubing attached. The box has four 1/8 inch built in barbs. Two barbs are required for inflow and outflow while the other two barbs are utilised for the sensor line and the bleed line. The pressure box dimensions are 0.1 m x 0.1 m x 0.1 m.

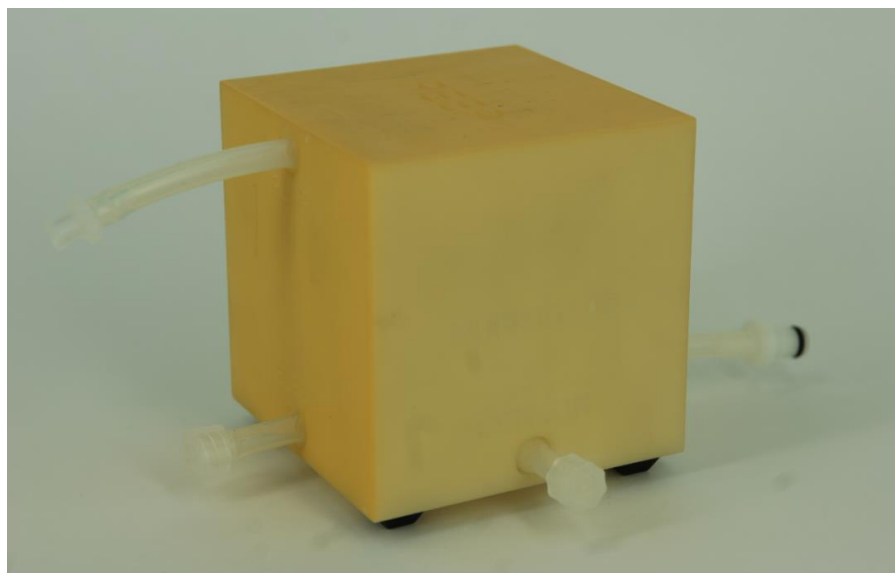


**Figure 2.17** The pressure box rated for 500 mbar of pressure and 3D Printed from Object Fullcure 7020 material by Formero. The box consists of an inlet, outlet, bleed line and a pressure sensor line. The pressure box dimensions are 0.1 m x 0.1 m x 0.1 m.

### Proportional Valve



**Figure 2.18** Clippards EV-P-05-6025 proportional valve. It is used as a bleed valve which is connected to the bleed line of the pressure box

The pressure box is regulated using a Clippards, EV-P-05-6025 proportional bleed valve as shown in figure 2.18. The bleed valve is connected to the bleed line of the pressure box.

### Outlet Valve

The outlet valve is a Clippards, EV-2-12-L solenoid valve as shown in figure 2.19. The outlet valve is connected between the pressure box and the reservoir.



**Figure 2.19** Clippards, EV-2-12-L solenoid valve. It is used as the outlet valve which is connected between the pressure box and the reservoir

### Pressure sensor



**Figure 2.20** Honeywell, ASDX005D44D 350mbar differential pressure sensor with circuitry and tube attached. The sensor is used to measure differential pressure of the flow control system.

The pressure of the system is measured by a Honeywell, ASDX005D44D 350 mbar differential pressure sensor as shown in figure 2.20. The sensor has a low operating voltage suitable for the system. It is accurate up to  $\pm 2\%$  of the operating span corresponding to  $\pm 7$  mbar. Pressure is measured in terms of voltage output. Therefore prior to use the sensor was calibrated using a known pressure source. To increase the working range of the pumping system the pressure transducer and boxes can be upgraded with a transducer and box capable of handling higher pressures.

### Fluid holding reservoir

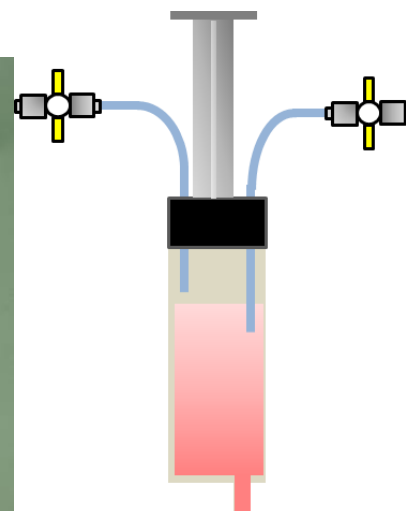


**Figure 2.21** The fluid holding reservoir. It is a modified Terumo 50 ml syringe with an air and refill flow access through the plunger side. By connecting these tubes to the return flow pump and the pressure pump we are able to refill and pressurize the syringe when it is fixed to a flow loop. The syringe approach makes it highly bio friendly as it is easily disposable and operable with minimum quantity of working fluid.



The fluid holding reservoir is a modified Terumo 50 ml syringe with an air and refill flow access through the plunger side. The modification is relatively easy to complete requiring only two holes through the plunger in to the cavity area. Tubes are guided through these holes and sealed in position. Figure 2.21 shows a syringe with these modifications completed. The air flow line is connected to one of the outlet valves. If a constant flow of fluid is required a refill pump can be connected to the remaining valve. If there is no refill requirement the remaining valve can be closed. By connecting these tubes to the return flow pump and the pressure pump we are able to refill and pressurize the syringe simultaneously when it is fixed to a flow loop.

Use of a syringe makes it highly bio friendly as it is easily disposable. Since the tube ends are not exposed open to air, the syringe maintains its normal functionality. This makes filling blood to the pressure pump simple. When pressure is supplied to the syringe, fluid is expelled out in a controlled manner. The syringe is interchangeable according to the amount of working fluid and flow rate. A 50 ml syringe was used for all experimental presented in this thesis.

### *Pressure system control software*

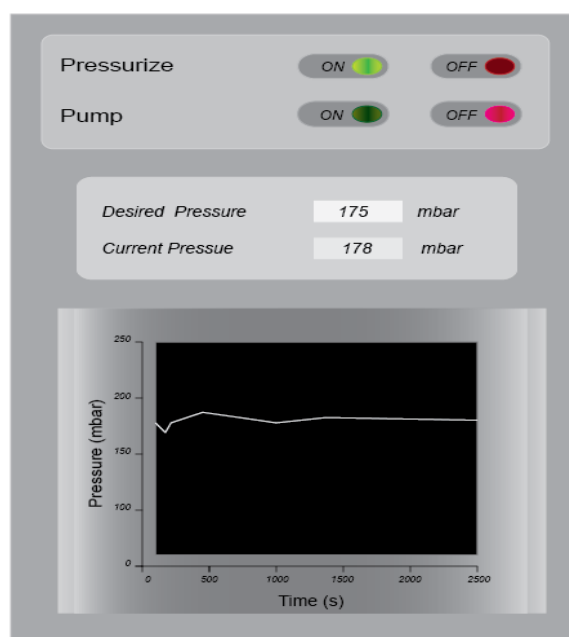


**Figure 2.22** *The Labview interface designed to control the pressure system. The interface provides the basic functions necessary for operation. It allows for pressurizing, pumping, setting desired pressure, view current and historical pressure measurements.*

Figure 2.22 shows the software interface designed through Labview software. The interface provides the basic functions necessary for operation. It allows for pressurizing, pumping, setting desired pressure, as well as viewing current and historical pressure measurements. The Labview interface and the hardware was integrated through a National instruments NI USB 6259 card.

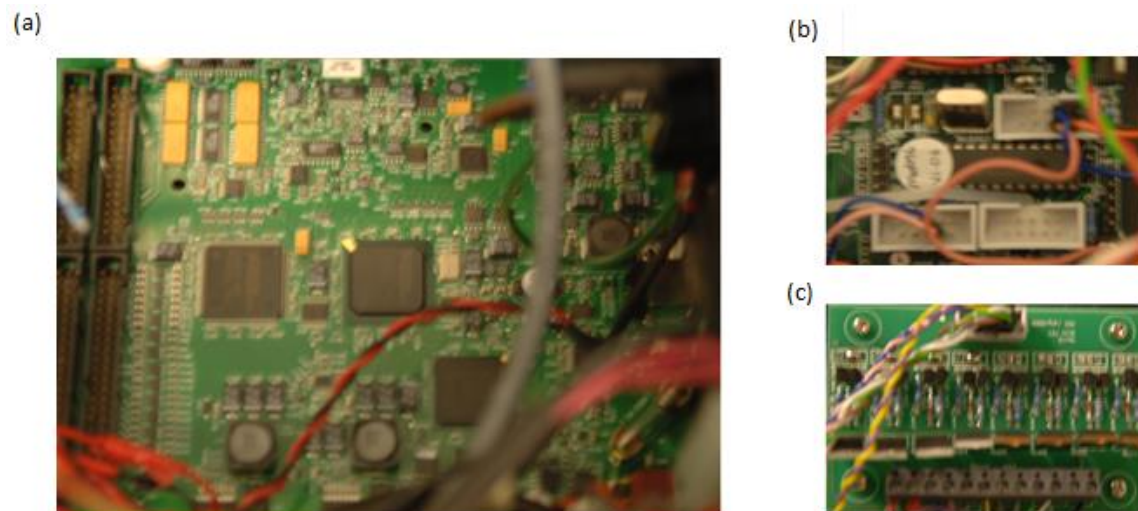


**Figure 2.23** Control hardware for the pressure system. Image of (a) the NI USB 6259 card used as the main board for hardware and software integration. (b) PIC processors used execute the control algorithm for the pressure system (c) MOSFETS used for amplifying control signaling to the bleed and outlet valve.

Figure 2.23 presents images of the electronic hardware components used for the pressure system. The National instruments NI USB 6259 card provides software and hardware interrogation. The PIC (peripheral interface controller) processors execute a PID algorithm to maintain the desired pressure. The feedback pressure is measured by the pressure sensor. Excess air is bled out through the bleed valve. Signals from the PIC processors are sent to the MOSFETS (metal–oxide–semiconductor field-effect transistor) which amplifies the signal to the valves. These hardware and software interactions allow for the pressure system to function.

### 2.2.2 Flow control valve design

A control valve was designed to achieve real time flow control. Figure 2.24 shows the physical and the CAD model of the flow control valve and its main components. The main component of the valve is a high precision linear actuator enclosed in aluminum housing. The housing holds the actuator centered to the tube seat. The flow carrying tube is positioned on the tube seat. A silicone rubber tube (Geko Optical, Australia, silicone tube) of 1.6 mm OD and 0.8 mm ID was used as the flow carrying tube for all experiments in this thesis. A pinch tip is fixed to the actuator to produce a sharper flow restriction without physical damage to the tube. The valve does not have any contact with the fluid making it a biocompatible flow manipulating method. The technique is insensitive to fluid properties.

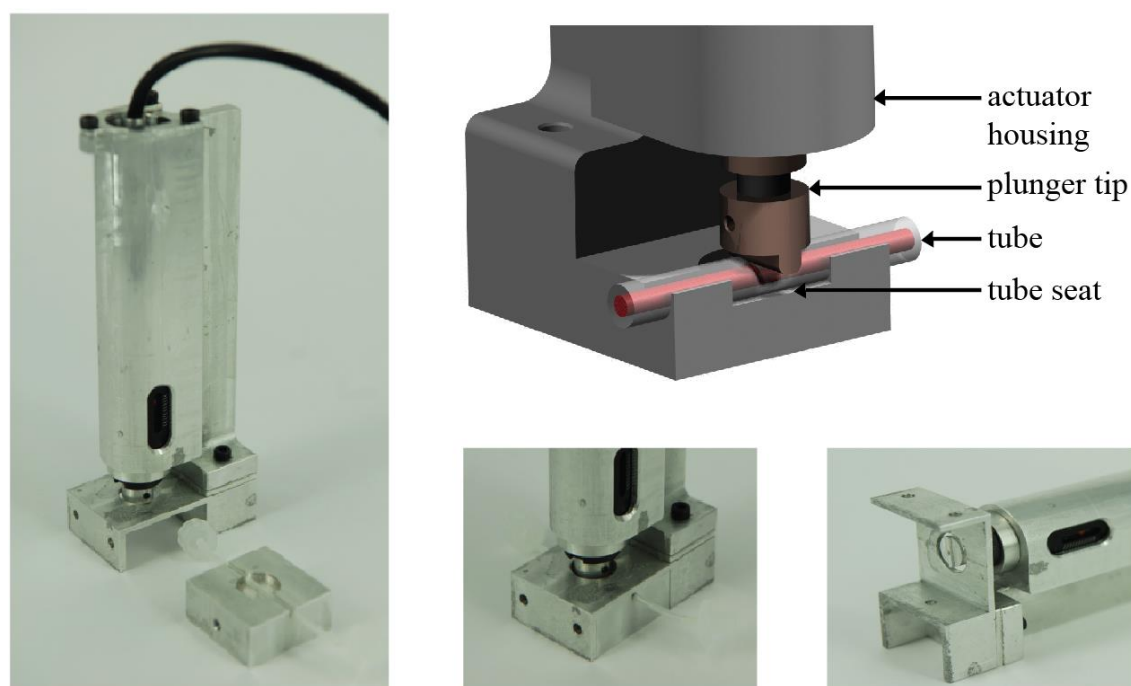


**Figure 2.24** The fluid control valve. Real time flow control is achieved by compressing the silicone tube carrying the flow as shown in figure. The main component of the control valve is a high precision linear actuator (PI instruments M 228.10S ) enclosed in an aluminum housing. The aluminum housing holds the actuator centred to the tube seat. A silicone rubber tube (Geko Optical, Australia, silicone tube) of 1.6mm OD and 0.8mm ID is wedged into the tube seat. A tip fixed to the actuator pinches the silicone tube avoiding damage to the biological fluid.

The actuator is a PI instruments M-228s linear actuator capable of a minimum increment of 1  $\mu\text{m}$ , maximum velocity of 1.5 mm/s, travel displacement of  $\pm 5$  mm, maximum a force of 20 N and a minimum backlash of 5  $\mu\text{m}$ . The displacement of the valve tip is proportional to the voltage provided to the actuator. Actuation is executed according to the voltage signals received from the feedback control system.

### 2.2.3 Flow probe Design

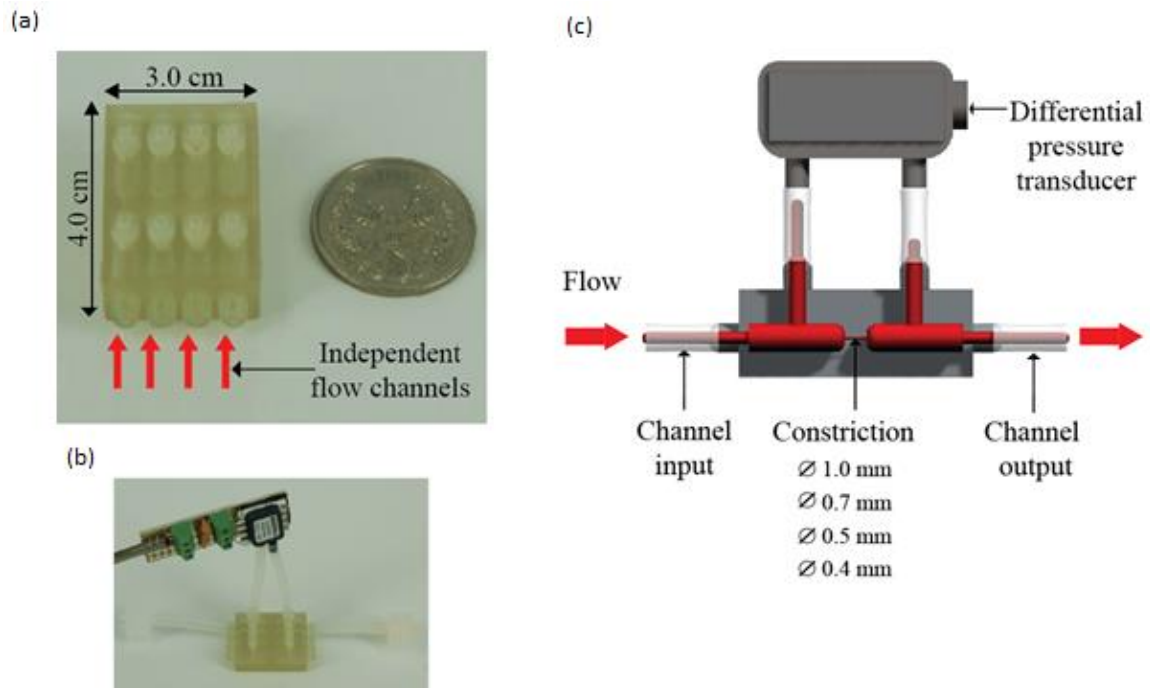


**Figure 2.25** The designed 3D printed flow probe. (a) The dimensions of the designed flow probe (b) the flow probe with a high precision pressure transducer attached. (c) cross section of the 3D printed flow probe

To measure the flow rate of biological fluids a disposable, compact and highly responsive flow-measuring device has been developed. The flow probe is modeled based on an orifice plate flow meter. Figure 2.25 (a) shows the dimensions of the flow probe. The physical volume of the flow block is  $12 \text{ cm}^3$ . The flow probe was 3D printed from Object Fullcure 7020 material at Formero, Australia. Volumetric flow rate is calculated by measuring the pressure differential across the constriction using a high sensitivity Sensortech, HCLA12X5DU differential pressure transducer. The sampling rate of the flow probe is 500 Hz. Figure 2.25 (b) shows the 3D printed flow probe with a high precision pressure transducer attached. Figure 2.25 (c) shows a cross section of the 3D printed flow. The flow probe has four independent channels with 1 mm, 0.7 mm, 0.5 mm and 0.4 mm orifice diameters. This permits exclusive sensitivity and dynamic flow range for each channel.

## 2.2.4 Feedback control system

### Feedback control system hardware

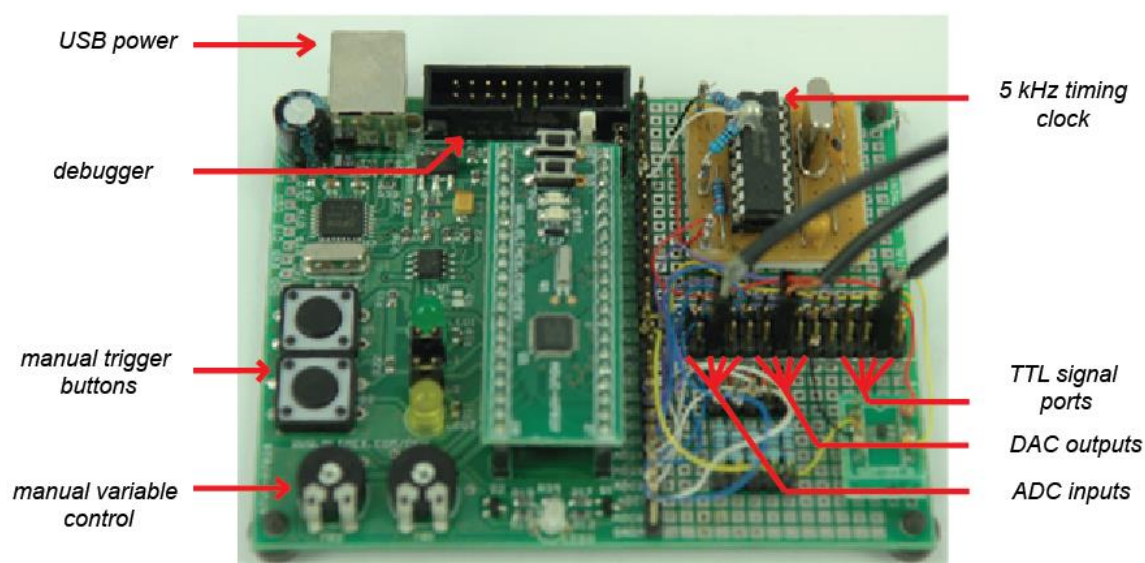


**Figure 2.26** The feedback control system. It is driven by an ARM7 microprocessor. The control system is able to accept real time flow signals at 5 kHz. Pre-programmed flow waveforms can also be stored on the board. Multiple TTL pulses or pulse trains for device triggering is easily implemented. The chipset has 4 analog to digital inputs and 4 digital to analog outputs giving it the capability to handle four fluid control valves each with its own feedback loop.

Figure 2.26 shows the key components of the feedback control system. The feedback control system is driven by an Olimex ADUC H7020 ARM7 microprocessor mounted on to a Olimex ATUC M7020 development board. The feedback control algorithm is executed from flash memory. The control system is able to accept real time flow signals at 5 kHz. Pre-programmed flow waveforms can also be stored on the board. Multiple 5V TTL pulses or pulse trains for device triggering can be easily implemented. The chipset has 4 analog to digital inputs (ADC) and 4 digital to analog outputs (DAC) giving it the capability to handle four fluid control valves each with its own feedback loop. This makes this system very attractive for microfluidic applications. The ADCs and DACs have a voltage range between 0 - 3.3V. The fluid control valve has a similar operational voltage range. At 0 V the valve has maximum negative velocity, at 3.3V the valve has maximum positive velocity. The input and output variables (of the control system) are 12bit registers. This corresponds to a number range of 0 - 4096. The processor is programmed from C programming language. The control system software executes standard PID control algorithm for flow control. Signal conditioning was performed on the raw feedback flow rate signal received from the pressure transducer. A Savinsky-Golay smoothing filter was used to filter the input signals. Sensor scaling and analog to digital conversion was also performed. The feedback control algorithm is described in the next section.

(a)

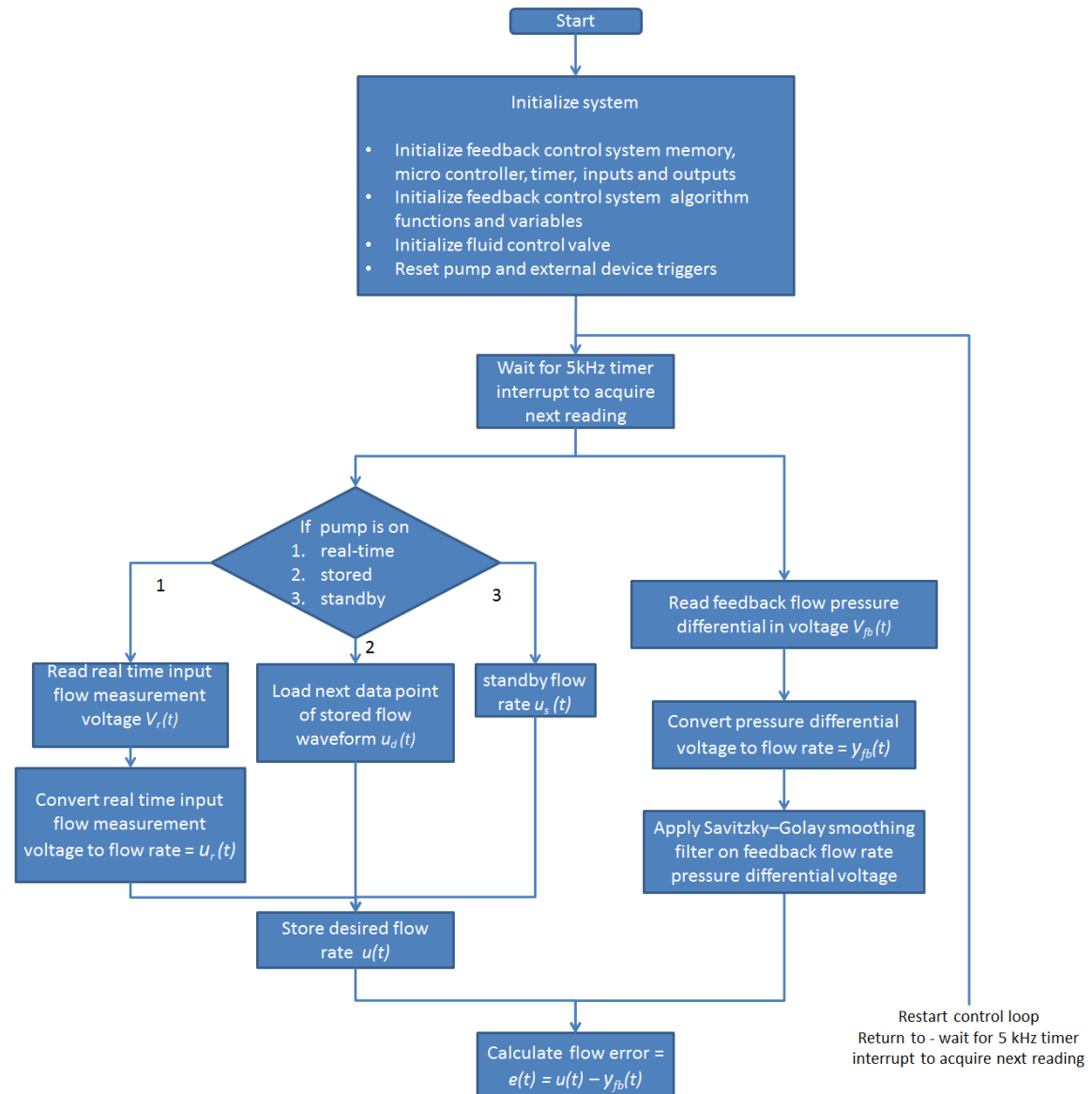


**Figure 2.27** Flow chart of the (a) first segment of the PID control algorithm.

(b)

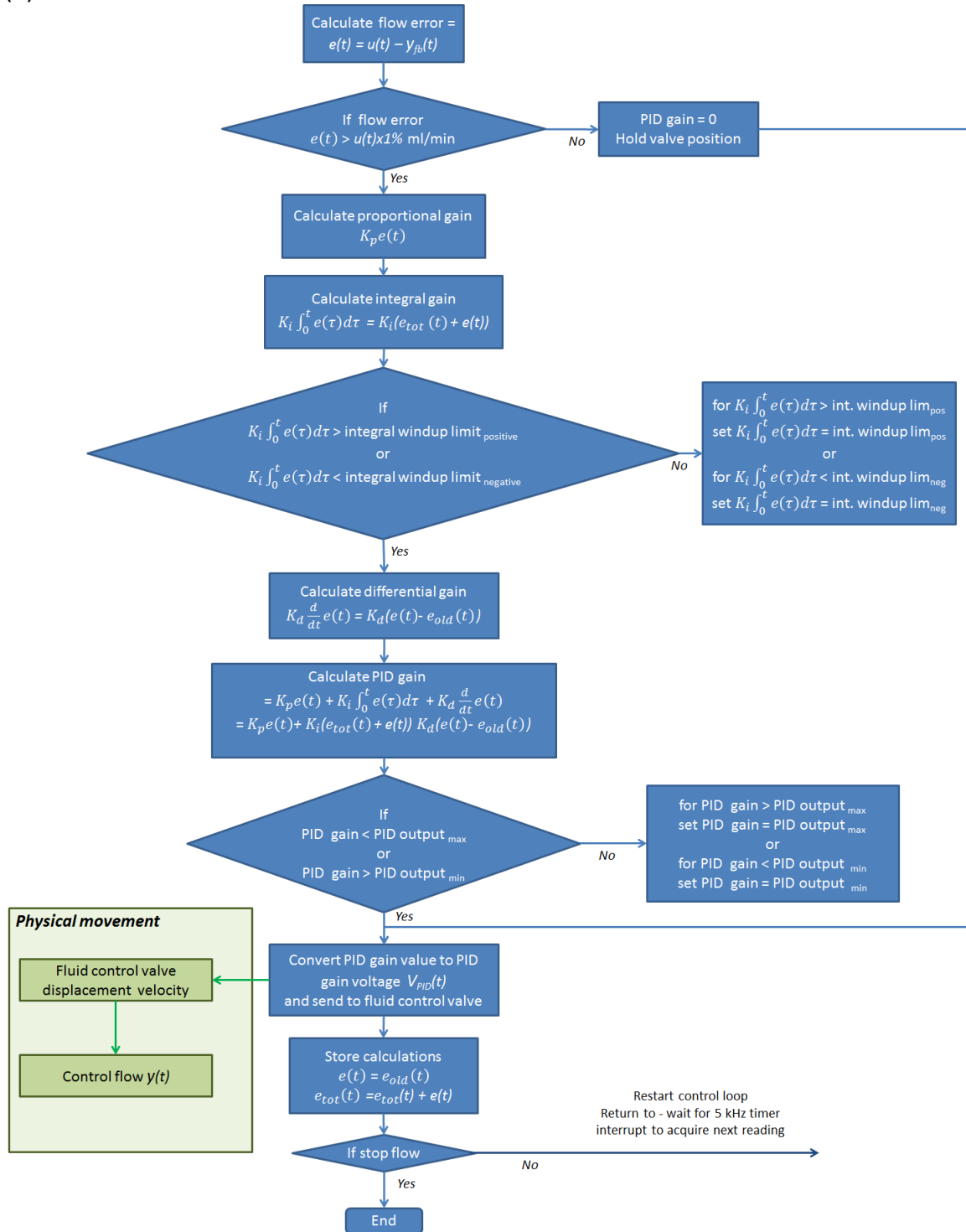


Figure 2.27 (b) second segment of the PID control algorithm.



The control algorithm is executed at a rate of 5 kHz. Figure 2.27 (a) shows the flow chart for the first segment of the feedback control algorithm. Upon system initialization the program waits for the 5 kHz interrupt timer. At each interrupt a new desired  $u(t)$  and feedback flow rate  $y_{fb}(t)$  measurement is acquired. The pump can be switched between standby, real time and stored waveform modes. If real time input  $u_r(t)$  is selected, the external flow readings are acquired as voltages and converted to flow rate. For digitally stored flow measurements  $u_d(t)$  the next data point of the stored flow curve is selected. The standby flow measurement  $u_s(t)$  is a pre-determined steady flow rate stored in memory executed at startup. The selected reading is then stored as the desired flow rate  $u(t)$ . The control system reads the feedback flow pressure differential voltage  $V_{fb}(t)$  from the flow probe. The value is then converted to a feedback flow measurement  $y_{fb}(t)$ . This reading and the previously read feedback flow measurements goes through the Savitzky-Golay filter. Finally the flow error  $e(t)$  is calculated between the desired flow rate and the feedback flow rate.

The control algorithm continues according to the flow chart on figure 2.27 (b). Once the flow error is calculated it is checked against the desired flow. If the error is smaller than 1% gains are not updated and the variable voltage for the fluid control valve  $V_{PID}(t)$  is set to 1.65V (output registry value of 2048 which corresponds to zero velocity to hold the fluid control valve in position. If error is bigger than 1%, the proportional, integral and differential gains are calculated.

A common fault experienced by a PID algorithm is integral windup. It causes the fluid control valve to reach and remain held in its negative or positive limit. This occurs due to the controller receiving an integral error for a long period of time accumulating itself to become a large error. To avoid integral windup maximum and minimum allowable contribution by the integral gain to the output voltage ( $V_{PID}(t)$ ) was limited to be 80% of the control valve travel limit. This allows for other gains to affect change in flow control and integral windup. We must also check for the maximum and minimum total gain to avoid register overflow. The gain limits are set to be within the limits of the PID voltage output  $V_{PID}(t)$  register which is between 0-4096 for a 12 bit register.

The calculated total PID gain is then converted to PID output voltage ( $V_{PID}(t)$ ) through the DAC (0-4096 12bit register value corresponding to 0 - 3.3V). The voltage controls the valve displacement velocity and in return control the output flow ( $y(t)$ ). The calculated error and total error for duration of operation is saved as the old error ( $e(t)_{old}$ ) and the total error ( $e(t)_{total}$ ). These will be used for calculation of PID gains in the next iteration. If the stop sequence is initiated the control system terminates. Otherwise it iterates from the beginning of the control algorithm by waiting for the next timer interrupt to restart the sequence.



## 2.3 Methods

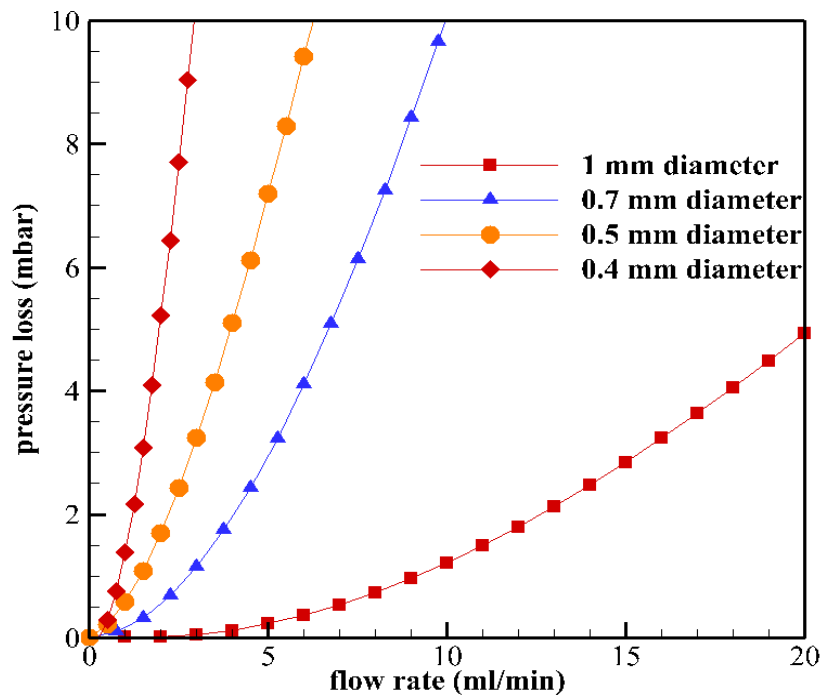
A Calibration test was completed on the flow probe to relate the pressure differential across the constriction to volume flow rate. The resulting calibration equation was utilised to enable flow measuring capability to the prototype flow control system. Manual tuning of the flow control algorithm was completed to generate desired response from the system. Performance tests were completed to evaluate flow generation performance. The experimental procedure and test results are presented in the subsequent sections.

### 2.3.1 Flow Probe Calibration test

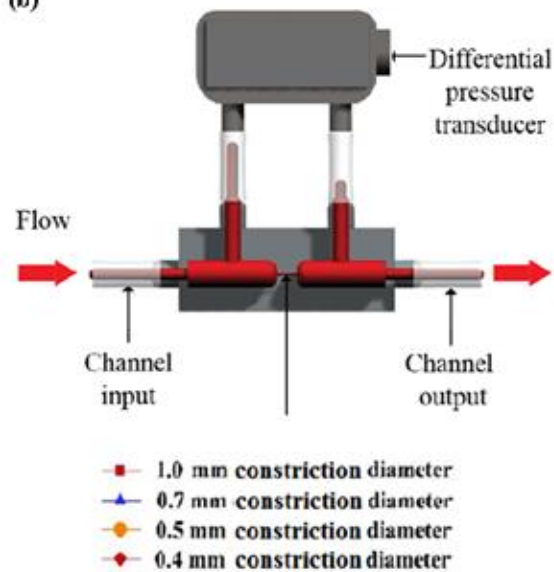
A calibration test was performed to relate volume flow rate through the flow probe and the pressure loss across the constriction. Fluid was pumped from a syringe pump (PHD2000 Harvard Syringe pump) for 60 seconds. The instantaneous flow rate and differential pressure from the pressure transducer were recorded using a flow meter (Transonic TS410 with ME1PXN probe) and a data acquisition device (IDT Motion pro data acquisition system). The measurements were integrated over time to estimate the average flow rate and the differential pressure reading. The calibration equation is then programmed to the feedback control system enabling flow measuring capabilities to the flow control system.

Figure 2.28 (a) presents the pressure loss as a function of the flow rate for each orifice diameter of the flow probe. The maximum standard deviation was 0.0275 ml/min for the 0.5 mm diameter constriction at a flow rate of 4.75 ml/min. Measurements show a parabolic trend with low variability. With increasing constriction diameter the flow probe range is increased but the sensitivity is decreased. Therefore, the correct channel should be selected once the required sensitivity and flow range is determined. The measurement error of the flow probe is 1.25% of the operational dynamic flow range. For experiments completed for this thesis this level of accuracy was sufficient. A suitable pressure transducer must be selected for applications requiring increased accuracy.

(a)



(b)



**Figure 2.28** Graph of (a) calibration curves of pressure loss as a function of the flow rate for each orifice diameters of the flow probe. The pressure loss, shown here in mbar, is measured between the orifice constrictions using the differential pressure transducer. (b) the cross sectional view of the flow probe.

### 2.3.2 Effects of Viscosity on steady flow performance

Generally, high viscosity limits the flow generation range of pressure driven pumps. Investigation of this characteristic is crucial as blood viscosity increases with increasing level of hematocrit (Ascuitto *et al.* 2010). On average, blood hematocrit varies between 40% and 60% (Ascuitto *et al.* 2010). To determine the operating flow range, low to highly viscous fluids were pumped for 60 seconds and the corresponding average flow rates was recorded. The viscous fluids were prepared by mixing exact measures of glycerin and water replicating the biological fluid viscosities of plasma ( $1.5 \times 10^{-3} \text{ N.s/m}^2$ ), 40% hematocrit ( $4 \times 10^{-3} \text{ N.s/m}^2$ ) and 60% hematocrit ( $6 \times 10^{-3} \text{ N.s/m}^2$ ) (Ascuitto *et al.* 2010).

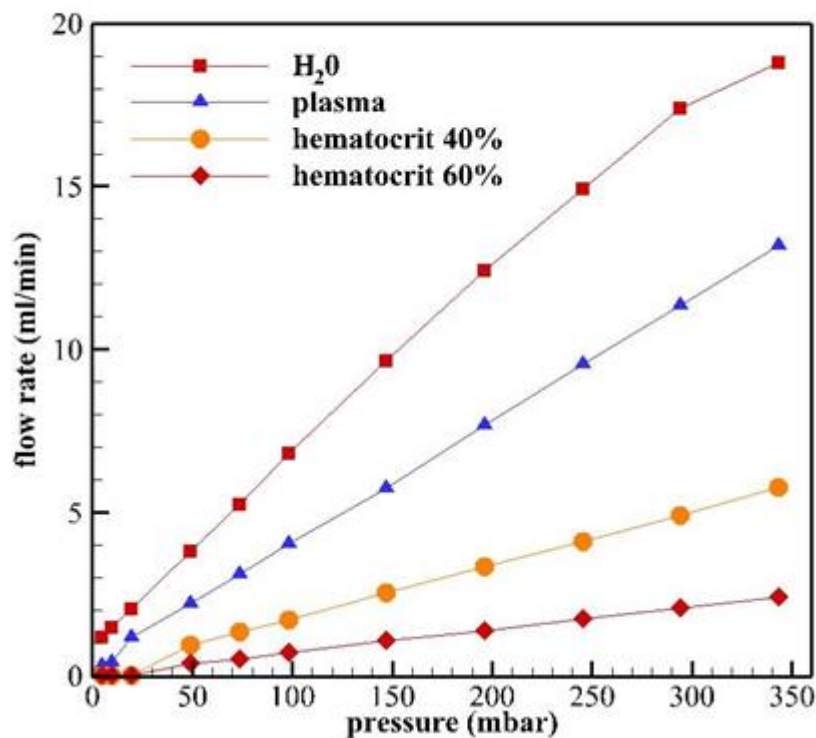


**Figure 2.29** Measured flow rate as a function of the operational pressure range of the flow control system for different viscous fluids. The maximum operational pressure is 350 mbar. As evident on the figure, the maximum flow rate decreases with increasing viscosity.

Figure 2.29 presents the average flow rate measured for various fluids, H<sub>2</sub>O, plasma, 40% hematocrit and 60% hematocrit, over the operational range of the pressure pump. The maximum standard deviation was 0.0325 ml/min at 350 mbar pressure for 40% hematocrit fluid. The maximum flow rates for H<sub>2</sub>O, plasma, 40% hematocrit and 60% hematocrit are 18.79 ml/min, 13.18 ml/min, 5.75 ml/min and 2.42 ml/min respectively. Higher flow rates can be achieved by increasing the pressure rating of the system. Results indicate that for this control technique, selected hardware and a pressure range of 0 – 350 mbar a linear relationship is observed between flow rate and pressure. The gradient is a function of the viscosity of the fluid.

### 2.3.3 Feedback Control System Tuning

Once flow measuring capability is established the feedback control system must be tuned to generate the appropriate response. There are several methods available for tuning a PID loop. They are the Ziegler Nicholas method, Cohen Coon method and manual tuning.

The proposed system aims to achieve flow generation with high response and low error. In a control algorithm high response is dictated by the proportional gain. Flow error is reduced by adjusting the integral gain. Therefore, to better determine these gains the manual approach was adopted. The differential gain provides improved stability and transient response to the system. This gain was calculated directly from the experimentally estimated  $K_p$ ,  $K_i$  and equations (5),(6) and (7).

Figure 2.30 shows the experimental setup used to conduct manual tuning. The complete flow control system shown in figure 2.14 was used. To closely reassemble experimental conditions a fluid with a viscosity of  $(4 \times 10^{-3} \text{ N.s/m}^2)$  was pumped through a  $0.2 \times 2 \times 200 \text{ mm}$  microchannel (item 3 in figure 2.29) to simulate similar operational back pressure. The refill flow line (item 8 in figure 2.14) was connected to the auxiliary pump (item 2 in figure 2.29) to maintain constant flow.

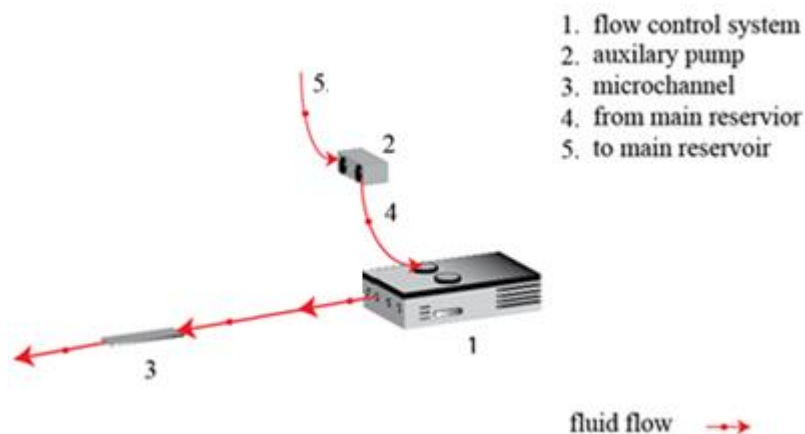


**Figure 2.30** Experimental setup used for manual tuning. The complete flow control system described in figure 2.14 was used. To closely reassemble experimental conditions fluid with a viscosity of  $(4 \times 10^{-3} \text{ N.s/m}^2)$  was pumped through a  $0.2 \times 2 \times 200 \text{ mm}$  microchannel

First the proportional gain that produced the fastest response time was determined. For this process the integral and differential gain is set to zero. The response time is the time measured from subjecting the system to a step change and the flow achieving steady state. For this experiment the steady state was considered to be when the flow error is less than 20% and the moving variance is less than 10% of the desired flow. The moving variance is calculated from the moving average and the square difference to the moving mean. The system was subjected to step inputs from 0 to 1 – 6 ml/min for proportional gains between 300 – 1800. The moving variance checks if the flow is steady. The flow error checks if the output is within

range and for drift in the output. Together they ensure the output flow stays within range of desired flow and maintains steady state and is not slowly drifting away with a small variance.

Next the proportional gain which delivered the fastest response time was fixed and the integral gain was changed to produce the smallest flow error. The differential gain is maintained at zero. The system was subjected to step changes from 0 to 1 – 6 ml/min for integral gains between 25 – 325. For the integral gain the flow error was measured instead of response time. The flow error was measured when the moving variance is less 5% of the desired input flow. Once the proportional ( $K_p$ ) and integral ( $K_i$ ) gains are established equations (5), (6) and (7) were used to determine the differential gain ( $K_d$ ).

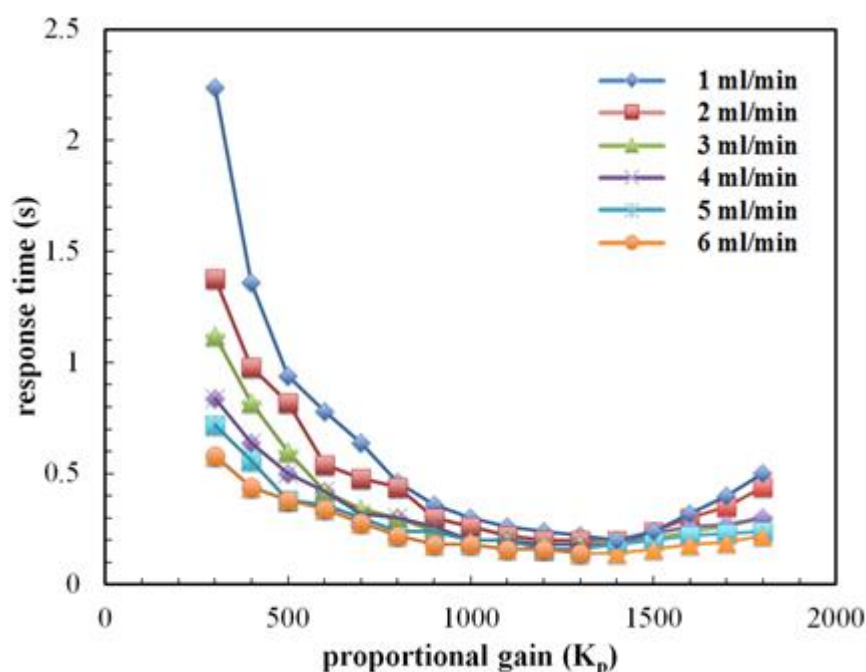


**Figure 2.31** The response time as a function of proportional gain for base flow rates from 1 -6 ml/min. Integral and differential gains were set to zero value. The optimum response was observed at a proportional gain of 1300.

Figure 2.31 shows the response time as a function of proportional gain for base flow rates from 1 -6 ml/min. The fastest response time was observed at a proportional gain of 1300. For low proportional gain the response time is much longer as velocity of the fluid control valve is slow. As the gain is increased the response time reduces. Increasing the gain past the optimum value increases the response time. This is due to increase in overshoot of the response curve requiring more time to achieve steady state.

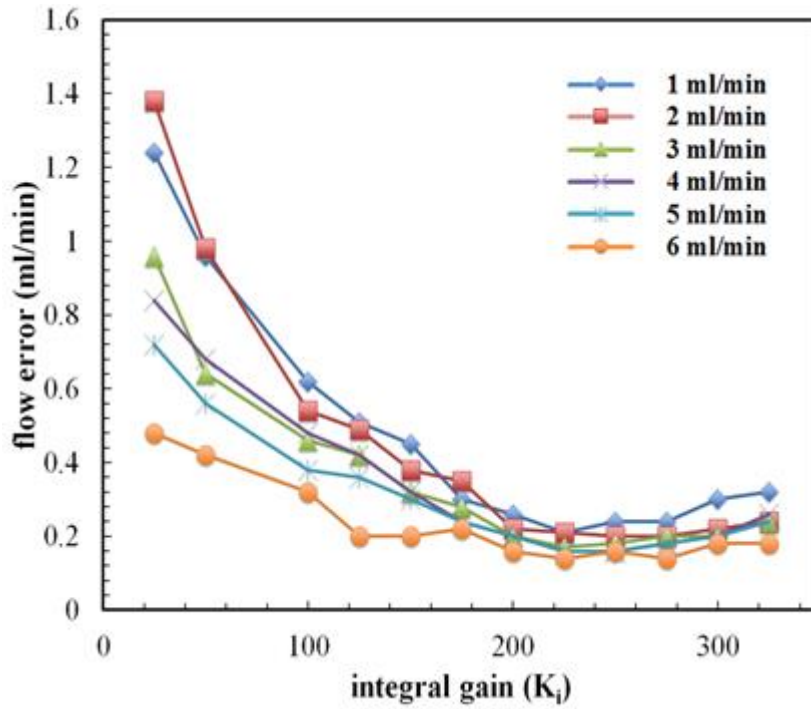


**Figure 2.32** The flow error as a function of integral gain for base flow rates from 1 -6 ml/min. The proportional gain was set to 1300 and the differential gains were set to zero value. The optimum response was observed at a integral gain of 225.

Figure 2.32 shows the flow error as a function of integral gain for base flow rates from 1 -6 ml/min. For low integral gain the steady state error is higher. This is due to the integral gain not having enough effect on the total gain. As the integral gain is increased so does its influence on the response. The lowest flow error was observed at an integral gain of 225. Further increase in gain starts to increase the instability of the system increasing flow error.

The differential gain ( $K_d$ ) was calculated from the determined proportional ( $K_p = 1300$ ), integral ( $K_i = 225$ ) gains and equations (5),(6) and (7). The differential gain is calculated below.

$$K_i = \frac{K_p}{T_i} \quad T_i = \frac{K_p}{K_i} = \frac{1300}{225} = 5.77$$

$$T_d = \frac{T_i}{4} \quad T_d = \frac{5.77}{4} = 1.44$$

$$K_d = K_p T_d \quad K_d = 1300 \times 1.44 = 1877$$

The described manual tuning method and established gains proved to produce effective flow control performance for steady, pulsatile and complex flows. It also exceeded flow requirements for proposed flow evaluation and thrombus growth experiments. The flow control performance results are presented in the next section.

### 2.3.3 Flow Control System Performance Tests

The performance of the flow control system was evaluated for steady, pulsatile and complex flows. The complete system shown in figure 2.14 was used. The controlled output (item 13 in figure 2.14), was connected to the Transonic flow meter and a data acquisition device as shown in figure 2.33. Using the transonic flow meter allows for independent confirmation of flow measuring of the flow control system. This is beneficial for prototype testing purposes. The refill flow line (item 8 in figure 2.14) was connected to the auxiliary pump (item 4 in figure 2.33) to maintain constant flow. To closely reassemble experimental conditions fluid with a viscosity of ( $4 \times 10^{-3} \text{ N.s/m}^2$ ) was pumped through a  $0.2 \times 2 \times 200 \text{ mm}$  microchannel (item 5) to simulate similar operational back pressure. For the steady flow performance test, the average flow rate was measured over 60 seconds and compared to the programmed steady flow rate. To quantify the accuracy of pulsatile flow generation, the total harmonic distortion (THD, *equation 10*) and the root mean square error percentage (RMSE, *equation 11*), for sinusoidal waveforms were measured.

$$THD = \left( \frac{P_{total} - P_{frq}}{P_{frq}} \right) \times 100 \% \quad (10)$$

$$RMSE \% = \frac{RMSE}{RMS_{input}} = \frac{\sqrt{\frac{\sum_{i=n} (x_{i_{input}}^2 - x_{i_{measured}}^2)}{n}}}{\sqrt{\frac{\sum_{i=n} (x_{i_{input}}^2)}{n}}} \times 100\% \quad (11)$$

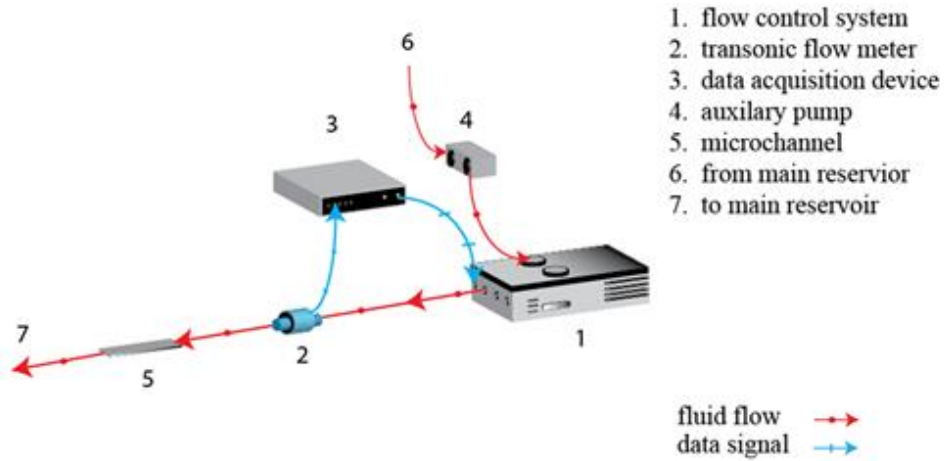


**Figure 2.33** Performance test experimental setup. To measure performance the complete flow control system described in figure 2.14 was connected to the Transonic flow meter and a data acquisition device. To closely reassemble experimental conditions fluid with a viscosity of ( $4 \times 10^{-3} \text{ N.s/m}^2$ ) was pumped through a  $0.2 \times 2 \times 200 \text{ mm}$  microchannel

### 2.4.3 Steady flow

Figure 2.34 presents the steady flow maintainability of the flow control system. Results indicate excellent linearity between measurements with a linear regression of 0.988 and an intercept of 0.01 ml/min. The maximum error is under 1.2% of the operating flow rate.

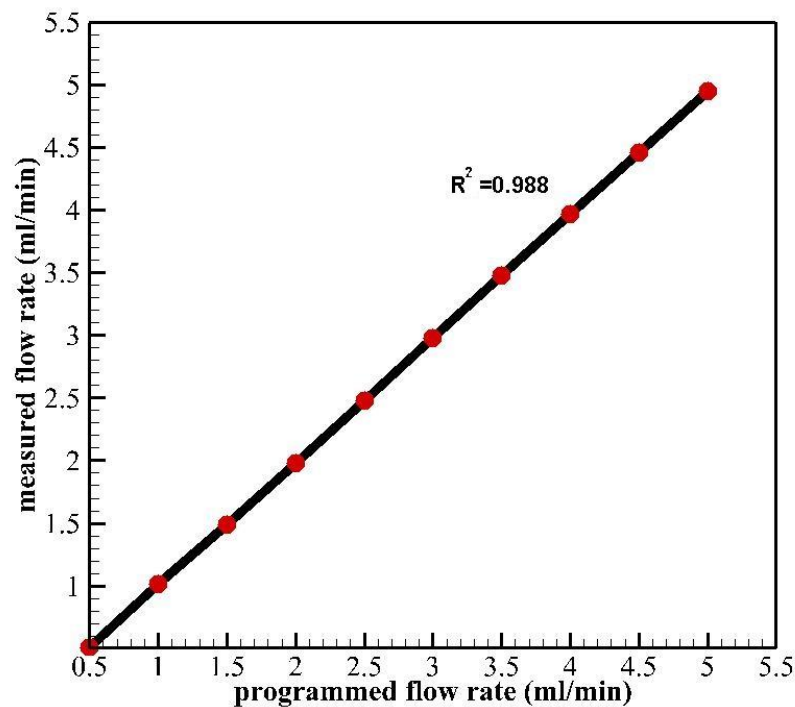


**Figure 2.34** Measured flow versus the programmed flow for 40% hematocrit fluid. Results indicate excellent linearity between measurements with a linear regression of 0.988. The maximum error is under 1.2% of the operating flow rate

### 2.4.4 Sinusoidal Pulsatile flows

The total harmonic distortion confirms the frequency and power of a sine wave. However, it is magnitude independent. Root mean square (RMS) is a statistical measure of magnitude. RMS for an ideal sine wave is  $\frac{a}{\sqrt{2}}$  ("a" being the amplitude of the sine wave). Root mean square error (RMSE) provides the difference of RMS between an ideal sine wave and the generated sine wave. The root means square error percentage (RMSE %), is the ratio of RMSE and RMS. This gives the ratio of accuracy for the magnitude. In combination we are able to establish the accuracy of both the frequency and magnitude of the waveform generated. One hundred cycles were recorded for each sinusoidal frequency measurement point. Real time flow measurements were acquired for steady and pulsatile flow experiments through the data acquisition device.



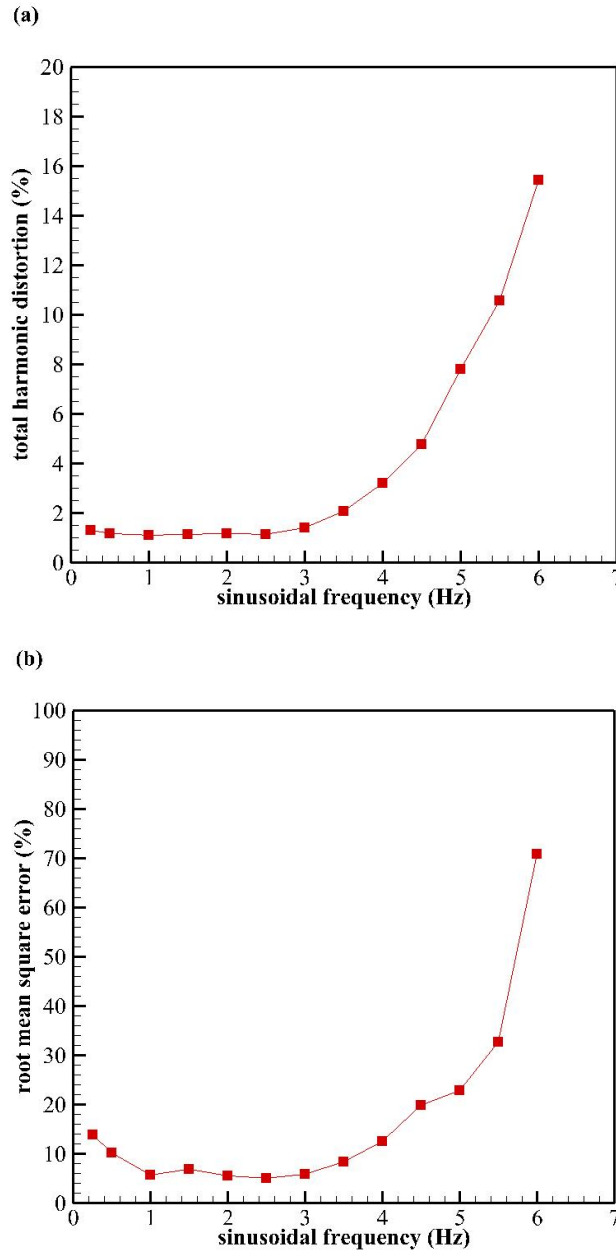


**Figure 2.35** Plot of (a) total harmonic distortion as a function of the sinusoid frequency. Distortion levels remain approximately constant up to about 2.5 Hz. (b) the root mean square error as a function of sinusoid frequency. The data complement the result from (a) indicating optimum operational range between 1-3 Hz, producing a total harmonic distortion of under 2% and a root mean square error under 8%.

The performance of the pump for pulsatile flow was evaluated using sinusoidal input waveforms. Figure 2.35(a) presents the total harmonic distortion as a function of the sinusoidal frequency. Figure 2.35(b) presents the root mean square error as a function of the sinusoid frequency. Both figures indicate a similar trend where total harmonic distortion and root mean square error increased with sinusoidal frequency. The total harmonic distortion remains approximately constant up to 2.5 Hz while the root mean square error remains relatively constant between 1 - 3 Hz. For frequencies less than 1 Hz the root mean square error is slightly higher. This is directly due to the selected system gains for the feedback control system and the

hardware limitations of the flow control system. Beyond a frequency of 3 Hz the total harmonic distortion and root mean square error increases. The optimum operating range for this system is between 1 - 3 Hz producing a total harmonic distortion of under 2% and a root mean square error under 8 %. Good system performance can be attained between 0 - 4.5 Hz with a total harmonic distortion of less than 5% and root mean square error less than 20%. For physiological flow experiments this range is acceptable as it translates to 0-270 beats per minute.

The control system gains were unchanged for all experiments in thesis to produce standardised results. For physiological experiments magnitude error is important, but the requirement for accurate frequency generation is more common. Increased frequency range can be achieved by substituting a faster control valve. To further improve the RMSE for high frequency applications (3 – 4.5 Hz) the sensitivity of control system can be increased. The magnitude accuracy can be improved by balancing the increase of base flow and re-tuning the gains of the feedback control system for a given flow profile. As an improvement for the next iteration of this control system, an auto-tuning gain control algorithm is proposed. This will automatically optimise the PID gains and reduce the magnitude error of flow waveforms over the working frequency as required.

#### 2.4.5 Complex Waveforms

Two test cases were used to test the prototype capability in complex waveform generation. The complex waveforms were generated through the programmed mode of the feedback control system. A human aorta waveform was digitised from the work of Taylor et. al (1998) . Five experimental runs of 100 cycles each were phase averaged and the root mean square error percentage was measured (*eqn 7.*). A Rat Aorta waveform was recorded at the Science, Technology, Research and Innovation Precinct (STRIP) Monash University, Clayton, Australia during a live rat experiment conducted by Laboratory of dynamic imaging (LDI), Monash University, Clayton, Australia. A perivascular flow probe was attached to the aorta similarly as shown in figure 2.36 (Eitzman et al. 2000).

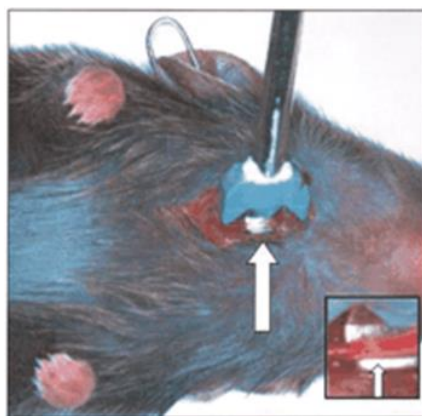
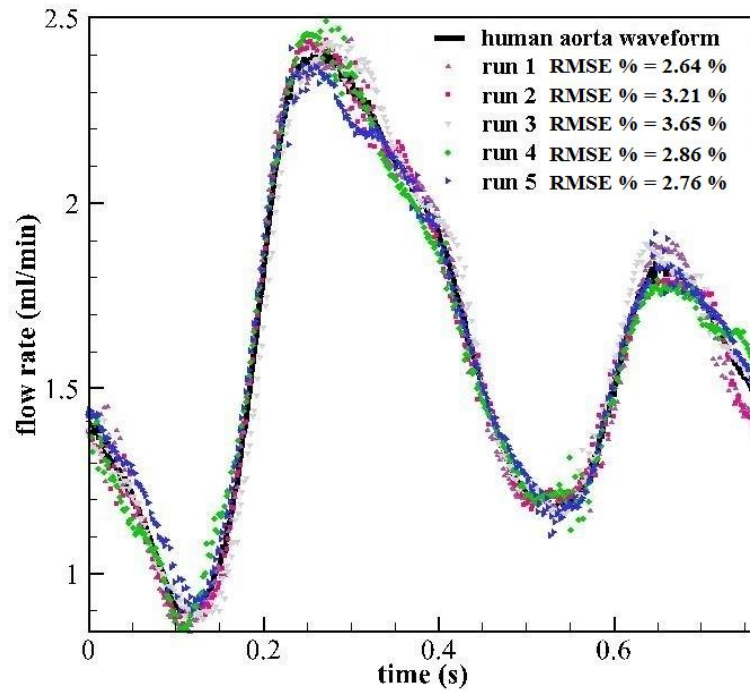


**Figure 2.36** Transonic perivascular probe attached to a rat aorta to record blood flow. Figure courtesy of (Eitzman et al. 2000)

(a)



(b)

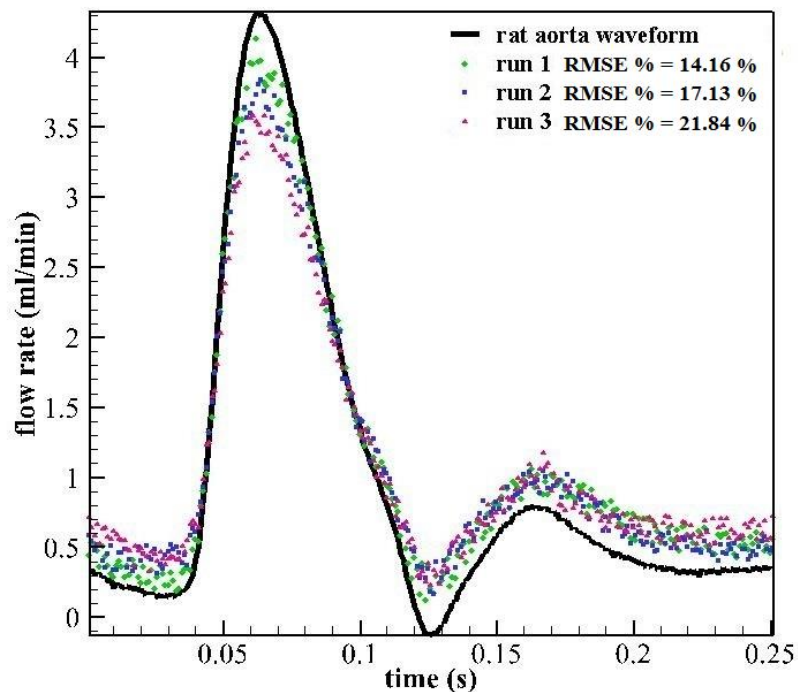


**Figure 2.37** Production of (a) a digitised human aorta waveform (Taylor et al. 1998). Five experimental runs with 100 cycles each were phase averaged (b) rat aorta waveform acquired from a live mouse at the Science, Technology, Research and Innovation Precinct (STRIP) Monash University, Clayton, Australia by Laboratory of dynamic imaging (LDI), Monash University, Clayton, Australia. 3 experimental runs with 100 cycles each were phase averaged

Figure 2.37 (a) presents the flow measured for the human aorta waveform. The output flow closely resembles the desired programmed flow rate with a root mean square error between 2.64% - 3.65 %. Figure 2.37 (b) presents the flow measured for the rat aorta waveform. A maximum root mean square error between 14.16 - 21.84% was measured. The period of one cycle is approximately 0.256s or 3.91 Hz which is approaching the limits of this prototype flow control system. In both aorta waveforms the main features remain preserved. The majority of errors occur at points of high flow acceleration or deceleration. The input rat aorta flow waveform has minor reverse flow. At this point the fluid control system would attempt to reach zero. The flow control systems lag between desired input flow and measured output flow for sinusoidal and Aorta waves were measured to be 0.07s. Lag adjustment for the curves were made prior to error calculation.

## 2.5 Flow control technique key advantages

The developed technique has many desirable features and characteristics suitable for a biological flow control system. The designed prototype system demonstrates these qualities.

### 1. Real time and programmed flow control technique

The technique provides accurate flow control real time with minor lag. Figure 2.33 confirms that any flow waveform can be easily programmed into the feedback control system. The system can also perform on demand waveform switching.

### 2. Low impact flow control method

The flow manipulating method exerts low forces on blood causing low hemolysis. Figure 2.24 shows how the fluid control valve compresses the silicone tube carrying the flow. This is highly desired as formation of a clot outside of the microchannel is unacceptable as it would alter or destroy any thrombi formed inside the microchannel (*Tolouei et al. 2011*).

### 3. Completely bio-compatible

All fluid contacting surfaces are fully bio-compatible and can be chemically treated for additional biological requirements. Figure 2.21 shows the fluid holding reservoir which initially holds the fluid. The flow subsequently travels through the 3D printed flow probe shown figure 2.25. The flow path is connected by silicone tubing.

### 4. Independent of viscosity

Blood consists of varying viscosity levels. This in turn affects the pressure at which the fluid needs to be pumped to maintain flow. Having a feedback control system allows for this and maintains the desired flow rate

independent of viscosity. Therefore it will handle both Newtonian and non-Newtonian liquids effectively

5. Ability to produce constant, pulsatile and complex flows

With the use of the high frequency control valve and the control feedback system any flow waveform can be generated in real time and programmed mode. Figure 2.30 shows steady flow results. Figure 2.31 shows results for pulsatile flow. Figure 2.33 confirms complex waveform generation.

6. High flow accuracy

The system maintains high flow accuracy for all types of waveform generation required for microchannel based experiments.

7. Flow control technique is independent of fluid properties

The technique is capable of handling any fluid without any chemical interaction as shown through the prototype.

8. Minimum operational volume

The reservoir syringe system is able work with a limited quantity of working fluid. It provides the practicality to modify commercially available syringes. The smallest size tested during experimentation was a 2.5 ml syringe. Figure 2.21 shows a modified Terumo 50 ml syringe

9. Control of pressure as well as flow

The feedback control system can be recalibrated to read pressure for pressure critical experiments.

10. Easy cleanup and disposability

Even with an inhibitor, blood ultimately clots when kept outside of the human body. The disposability eliminates the need for cleaning allowing for quick turnaround between experimental runs.

11. Non contacting pumping mechanism and minimal mechanical wear

As it is mostly an air pressure driven system the need to mechanically maintain gears and motors are eliminated.

12. Scalable technique for other flow applications

The pressure system, flow probe can be scaled according to the required application. Table 2.2 presents a list of modifications required for increase in performance

Increasing Variable	Modification
Flow range	Increasing pressure rating Increase pinch tube size
Accuracy	Use of a faster control valve Increase flow probe sensitivity Adopt filtering algorithms Better tuning of PID loop
Pulsatile Frequency	Use of a faster control valve
Number of control channels	Add I/O to feedback control system

**Table 2.2** Guide table for increasing performance of the flow control system.

## 2.6 Chapter conclusion

A real time and completely biocompatible flow control technique and prototype system for microchannel based physiological experiments has been developed. The control technique consists of a constant air pressure source to supply the base flow rate, a compact, disposable flow probe to measure flow rate and a real time feedback control system to drive a fluid control valve. The fluid control valve allows for fine control over the base flow produced by the pressure source by pinching a silicone tube carrying the flow. Performance tests completed for the prototype show a steady flow error of 1.2%. The optimum pulsatile working range is for flow oscillations between 1 – 3 Hz with a total harmonic distortion of under 2% and a root mean square error under 8% for sinusoidal waveforms.

## 3.0 Particle Image Velocimetry

Detailed knowledge of the velocity distributions of blood flow in microvessels are essential in-vivo studies of disease and substance exchange between blood and tissue. Thus one of main applications for this prototype flow control system is flow evaluation inside microchannels and models of diseased flow. The system can be used to produce typical and irregular blood flow waveforms within microchannels and models to identify local flow profiles and hemodynamics associated with disease. The most commonly used flow evaluation technique within this scale is microscopic Particle Image Velocimetry (micro PIV). This chapter aims to present background on micro PIV and demonstrate the prototype flow control systems suitability to be used in flow evaluation experiments.

### 3.1 Background

#### 3.1.1 Blood velocity profile and diseases

Microcirculation causes mechanical interactions between the blood and endothelium. Modeling of microcirculation in arterioles, capillaries and venules is essential in understanding the process of maintaining healthy tissue and organs (*Yasuhiko et al. 2005*). Research has revealed that atherosclerosis, stenosis development, and thrombus formation are linked to changes in hemodynamics (*Ku et al. 1985; Nesbitt et al. 2009; Tolouei et al. 2011*). It has been shown that local variations in flow, particularly slow flow, low mean wall shear rate and high concentration of LDL (a carrier of cholesterol) leads to a high risk of atherosclerosis (*T. Wada & Fukumoto 2000*). However, hemodynamic velocity profiles in arteries for these conclusions were not established based on physiological pulsatile conditions (*Bitsch et al. 2003*).

Micro PIV is a widely used technique used to measure velocity fields in microscopic flow systems (*Meinhart et al. 1999; Santiago et al. 1998*). It is an ideal tool to evaluate instantaneous velocities for steady and pulsatile flow profiles. The method was developed through the application of Particle Image Velocimetry (PIV) to studying flows in the range of hundreds of microns. PIV is ideal for direct validation of CFD and is a non-intrusive optical method (*Lindken et al. 2006*).

The flow profile near vessel walls for steady flow has been measured through micro PIV by numerous researches (*Meinhart et al. and 1999; Sinton 2004*). Near wall regions are often characterised by strong velocity gradients that can cause shear induced migration of particles. Yasuhiko et al. (2005) measured velocity distribution of red blood cells from PIV in a rat mesentery.

Sugii et al. (2002) improved in-vivo measurement accuracy and spatial resolution. By measuring the axial blood velocity on a rat mesenteric arteriole they demonstrated that the velocity profile and wall shear stress are sensitive to the geometry of the vessel due to multiphase flow attribute near the wall (*Sugii et al. 2002*).

### 3.1.2 Micro PIV

PIV is an optical technique which enables instantaneous measurement of the flow velocity at several positions in a plane. PIV involves seeding the flow with light reflecting or fluorescing particles and using a laser to illuminate these particles in the measurement plane. The motion of the seeding particles is used to calculate the velocity of flow being studied. While micro PIV is derived from PIV, they are considered separate methods as they have different optical and mechanical constraints. PIV is macro scaled and seeding particles in the measurement plane are illuminated through a laser sheet. In micro PIV it is difficult to illuminate only the measurement plane, therefore it is volume illuminated. In PIV, the flow is seeded with particles that are assumed to faithfully follow the flow they are subjected to. But in micro PIV the seeding particles are micro sized and heavily affected by Brownian motion. The optical limitations experienced by micro PIV increases background noise. Therefore, averaging and filtering techniques are used to improve the signal and to reduce noise.

Early attempts to develop micro PIV started with particle streak velocimetry. Epifluorescence microscopy was used with long exposure times to record images of streaks of moving submicron fluorescent particles, from which the fluid velocity field was visualised. The method displayed irregular particle spacing and spatial resolution. Since then micro PIV has made enormous advancements driven by improved optics, lasers, tracking particles and evaluation algorithms.

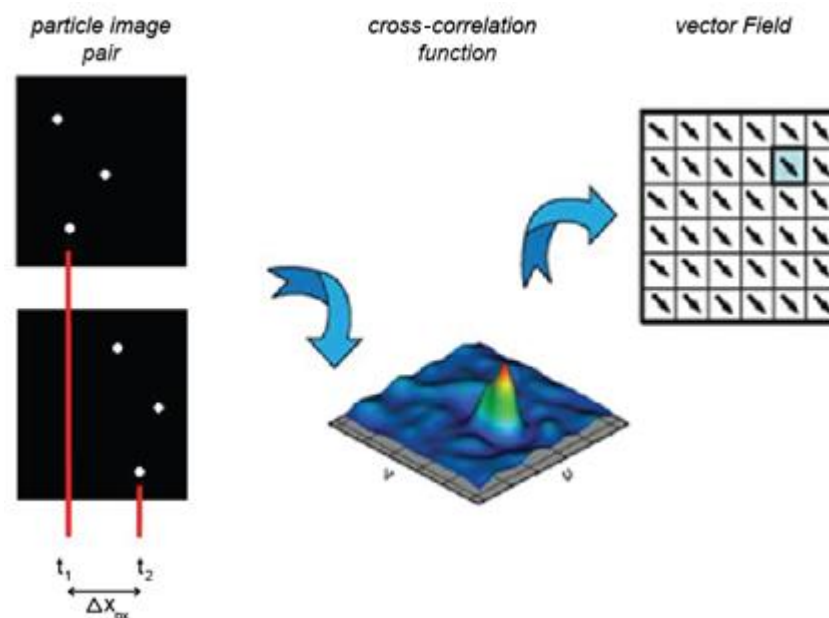


**Figure 3.1** Measurement of instantaneous velocity from micro PIV image pairs. Image pairs are acquired between a set time interval allowing particles to displace a measurable distance. The digitised PIV recordings are divided into small sub areas called interrogation windows. For each window, a cross correlation function is generated from the two image pairs. The function produces a signal peak indicating particle displacement and direction. Finally the local displacement vector for each interrogation window is determined.



Figure 3.1 presents steps required to generate velocity measurements from raw micro PIV images. Firstly, images are captured within a fixed time interval allowing for particle displacement. The interval between the two images  $\Delta t$  is a function of the camera frequency  $f$ . This is shown by equation (12) where  $\Delta t$  the time interval and  $f$  is the imaging frequency.

$$\Delta t = 1/f \quad (12)$$

The minimum measurable displacement of particles between images  $\Delta x_{px}$  must be greater than two pixels and less than half an interrogation window. Interrogation windows are subdivisions of the digitised PIV image containing a number of moving particles. These interrogation windows are then cross-correlated with the corresponding window in the next time interval. The cross-correlation function produces a map that is representative of a probability distribution for the displacement of the underlying particles. The signal peak of this map indicates the modal displacement and direction of the particles within the interrogation window. As the peak is defined by the integer pixel locations within the cross-correlation map a sub-pixel accurate displacement measurement is obtained through sub-pixel interpolation within the peak. The velocity field of the flow is calculated by evaluating the displacement vector for all the interrogation windows (*Raffel et al. 2007*). The velocity is expressed as displacement over time by equation (13).

$$V_{px} = \frac{\Delta x_{px}}{\Delta t} \quad (13)$$

There are many factors affecting the quality of micro PIV measurements. These will be discussed in the subsequent sections.

### 3.1.4 Factors affecting micro PIV quality

The spatial resolution of micro PIV imaging is primarily dictated by recording optics, intensity, seeding density, flow interaction, Brownian motion and the depth of correlation (*Meinhart et al. 1999; Santiago et al. 1998*). Selecting suitable image processing techniques affects the quality of results.

#### Optics & Intensity

Micro PIV uses volume illumination to fluoresce seeded particles. The entire depth of the sample is flooded by a volumetric cone of light. The measurement field must then be defined by the depth of field of the recording lens (*Wereley & Meinhart 2010*).

A double pulsed laser or a continuous laser with an optical shutter is used to generate suitable exposure times, image acquisition times ( $\Delta t$ ) and monochromatic

illumination. The fluorescence of the seeded particles is excited by the monochromatic laser light causing emission at longer wavelength. An optical filter in the microscope is placed between the light collecting objective and the camera. The filter allows the light emitted from the tracer particles to pass through the camera while filtering out the excitation. This removes most unwanted reflections thus increasing the signal to noise ratio.

Light emitted by fluorescent particles increase proportionally with excitation light intensity until it reaches a saturation level. Beyond which increasing the illumination intensity level does not improve image quality. Extreme seeding density should be avoided as this increases background noise and particle agglomerations. This is especially relevant for long running experiments where tracer particle agglomeration and adhesion to the wall reduces accuracy.

The two main properties of the camera are exposure time and the frame rate, where the frame rate represents the time ( $\Delta t$ ) between image pairs. Decreasing exposure time leads to darker images. Increasing the frame rate decreases the maximum possible exposure time. Therefore, a balance between these two properties must be established, taking into account the appropriate displacement values required to resolve the flow.

High spatial resolution for micro PIV can be obtained if particle diameter is in the range of 3-4 pixels when imaged. This can be achieved by using a high numerical aperture and adjusting the magnification to suit (*Wereley & Meinhart 2010*).

### *Seeding density & Brownian motion*

In micro PIV particles must be small enough to faithfully follow without disruption and must be large enough to be imaged and dampen the effects of Brownian motion (*Santiago et al. 1998*).

As particles are not constrained to travel directly along the focal plane, they can move in and out of focus. In addition there are particles above and below the focal plane. Figure 3.2 (a) illustrates how particle size varies as they move in and out of the focal plane. Figure 3.2 (b) is a sample micro PIV image seeded with particles. Focused particles appear bright and small while unfocused particles appear dull and large. Volume illumination of these out of focus particles introduces measurement errors as the velocity of these particles is not necessarily the velocity at the focal plane.

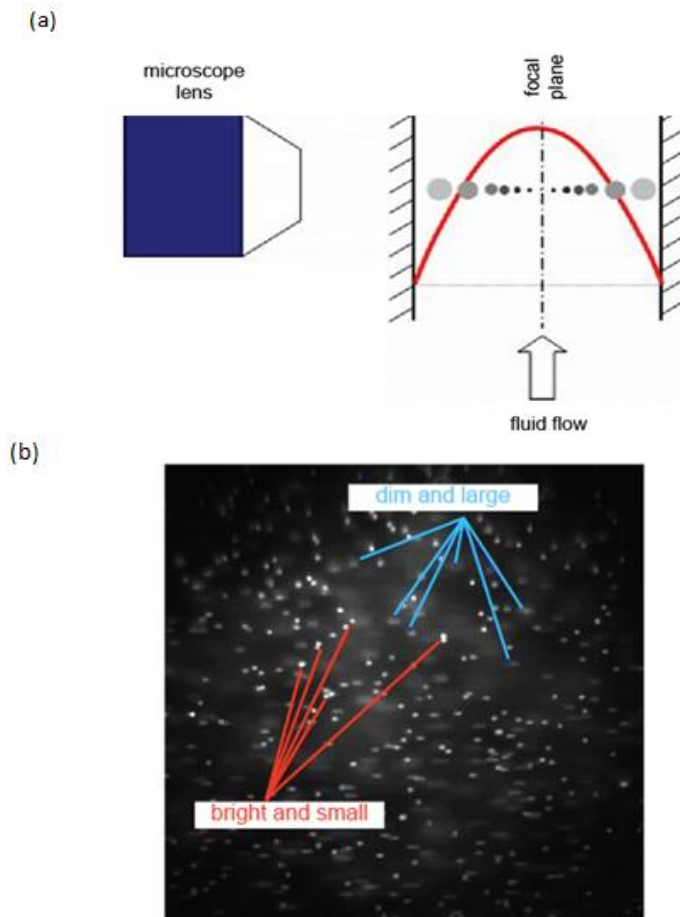


**Figure 3.2** Image presenting (a) change in particle size when imaged as it moves away from the focal plane (b) a micro PIV image seeded with particles. Focused particles appear bright and small while out of focus particles appear dull and large. Picture Courtesy of FLAIR Laboratory, Monash University, Australia

### Depth of correlation

In micro PIV compared to a conventional PIV system, the measurement plane is defined by the limited depth of focus of a microscope objective. The field of interest is volume illuminated allowing the fluorescent tracer particles to emit light at a specific wavelength. This distinguishes light emitted by tracer particles and background light that is scattered by the surrounding tissue (Kim *et al.* 2004).

The depth of correlation  $Z_{corr}$ , is defined as the focal distance which particles contribute significantly to the correlation function. As particles move out of the focal plane the particle size increases due to blurring. The width of the auto correlation function increases as this reduces the width of the auto correlation function. If the particles move further away from the focal plane it will exceed the depth of correlation. The properties of the microscope objective will influence the depth of correlation. Increasing focal number increases the depth of correlation. Increases magnification decreases the depth of correlation.

$$z_{corr} = \left[ \frac{1-\sqrt{\epsilon}}{\sqrt{\epsilon}} \left( f^{\#2} d_p^2 + \frac{5.95 (M+1)^2 \lambda^2 f^{\#2}}{M^2} + 8\beta^2 D\Delta t f^{\#2} \right) \right]^{\frac{1}{2}} \quad (14)$$

Where

$f^{\#}$	Focal number
$\epsilon$	Ratio between the correlation weighting at $z_{corr}$ and $z = 0$
$\lambda$	Particle fluorescence wavelength
$8\beta^2 D\Delta t f^{\#2}$	Effects of Brownian motion
$M$	Magnification
$d_p$	Particle diameter

Olsen et al. (2000) presented work on the effects of depth of correlation. From equation (14) it is clear that the depth of correlation is a function of focal number, the ratio between the correlation weighting at  $z_{corr}$  and  $z = 0$ , wavelength at which particles emit light, effects from Brownian motion, magnification and particle diameter.

### Image processing

Averaging measurements has shown to reduce noise in micro PIV. Comparison of accuracy of different averaging techniques for micro PIV was established by measuring the velocity field in a rectangular glass microchannel which has a known analytical solution (Meinhart et al. 1999). Meinhart et al. (1999) compared various averaging techniques to reduce the effects of noise on measurements. Image averaging is the process of averaging images to reduce image noise before producing cross-correlation and displacement measurement. Correlation field averaging involves averaging the cross-correlation maps at each time point to reduce noise within the cross correlation map before displacement measurement. Lastly, vector averaging is where the vector for each interrogation window at each time is calculated and averaged. All these techniques results in a time-averaged displacement measurement. Meinhart et al. (1999) showed that correlation averaging produces the lowest measurement error while vector averaging produced the highest measurement error. The averaged correlation function provides a more reliable estimate of the mean particle displacement than correlation functions from single image pairs. It also increases the effective particle image density and allows the corresponding interrogation size to be reduced (Samarage et al. 2012).

The size and spatial arrangement of interrogation windows define the in-plane spatial resolution of the resulting velocity field. The interrogation window should be sufficiently small so that effects due to velocity gradients are negligible.

As particles away from the depth of focus appear bigger and have low intensity, a band pass filter can be used to filter out these low intensities so that they do not contribute to the cross-correlation of the image.

## 3.2 Methods

The following experimental procedure was followed to measure varying sinusoidal flow waveforms inside a microchannel using micro PIV. The prototype flow control system allows for production of accurate sinusoidal waveforms under 4.5 Hz.

### 3.2.1 Experimental procedure

Micro PIV was used to evaluate the velocity profile inside the microchannel for steady flow and sinusoidal input waveforms at 1Hz, 1.5Hz, 2Hz, and 2.5Hz. The pulsatile frequencies relate to the physiological heart rates of 60, 90, 120, 150 beats per minute.

$$\tau = \frac{6Q_m}{wh^2} \quad (15)$$

Where,

$Q_m$  Volume flow rate inside microchannel  
 $w$  cross-sectional width of the microchannel  
 $h$  cross-sectional height of the microchannel

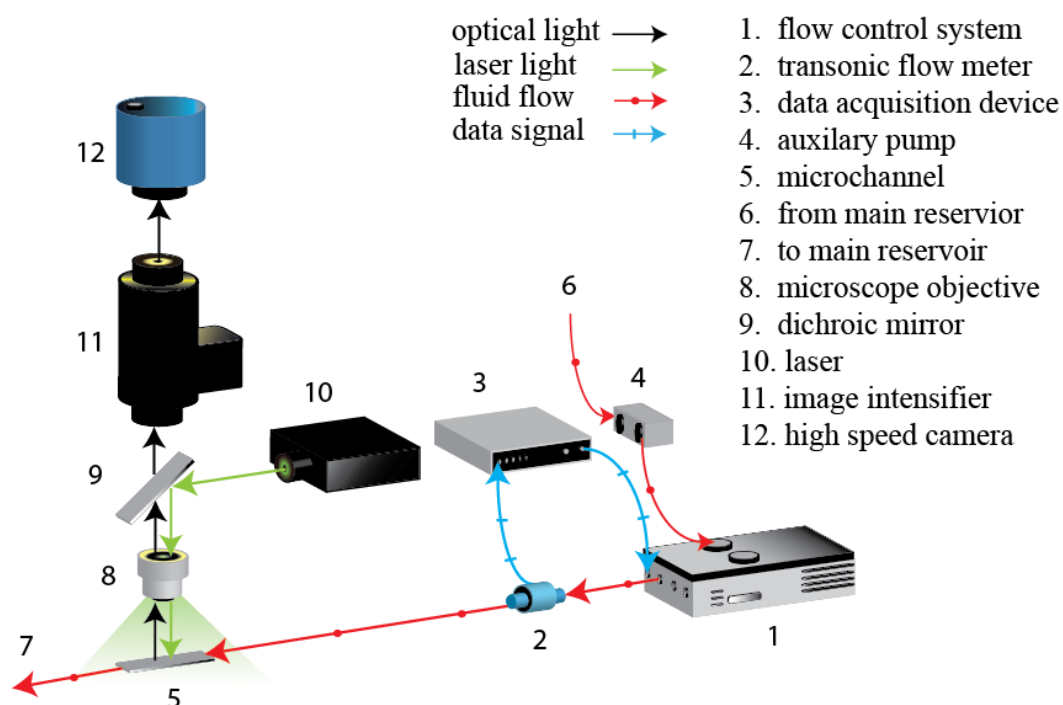


**Figure 3.3** Experimental setup used for micro PIV flow evaluation. Transonic flow meter is used to obtain independent measurement of flow. Real time flow measurements to the prototype flow control system is supplied through an IDT Data Acquisition device. Same device was used to record transonic flow meter readings.

Firstly, the prototype system and the microchannel must be checked for manufacturing defects. The technique of pinching the flow carrying tube must also be tested to evaluate its effect on producing typical flow profiles inside a microchannel. Therefore, to test these aspects, steady flow at a mean flow rate of ( $Q_m$ ) 1.44 ml/min was produced and imaged. For pulsatile flow a mean flow rate of ( $Q_m$ ) 1.44 ml/min corresponding to a mean shear rate of  $1800 \text{ s}^{-1}$  with an amplitude of 30% was used. This corresponds to flow rates used in thrombosis experiments presented by Tolouei et al. (2011). For steady flow a mean flow rate of 1.44 ml/min was maintained. The experimental micro PIV setup is presented in figure 3.3. It consists of a Leica microscope stage with a Nikon 20x 0.7NA objective, an IDT Y4-S1 camera for imaging, a ND YAG Class 3R laser to illuminate tracer particles and a Lambert instruments II18 intensifier to boost low emitting light conditions. Thermoscientific fluorescent green 3 micron particles were mixed with viscous fluid at a ratio of 15:1 ml. The viscosity of the fluid corresponds to blood at 40% hematocrit. PIV images were acquired at a frequency of 10 kHz. Microchannel of size 0.2 mm x 2 mm x 200 mm was used for the experiments. Flow probe orifice diameter channel of 0.5 mm was selected for the experiments. Figure 3.4 shows the three imaging planar locations inside the microchannel used for steady and all sinusoidal frequencies. Half the width of the microchannel was imaged at  $z = 25 \mu\text{m}$ ,  $z = 50 \mu\text{m}$  and  $z = 100 \mu\text{m}$  above the bottom wall. For steady flow both halves of the microchannel were imaged separately and combined to produce the flow profile for the entire width. Imaging was restricted to half the width of the microchannel to obtain high quality time varying velocity data. This is due to the high magnification and frequency required to image fluorescent particles and their displacement at a high planar resolution. Imaging at a high magnification and frequency is further restricted by the camera storage image capacity available to image the entire flow profile. The streamwise image position along the x axis was approximately at the middle of the channel. The maximum Reynolds number produced for this experiment was 1.45. In a microchannel of this size the transition occurs at around Reynolds number of 240 (Shou-Shing et al. 2004). Therefore, flow is fully developed at this streamwise location.

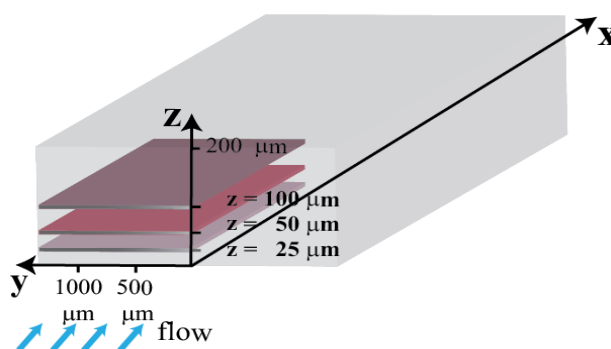


**Figure 3.4** Imaging planar locations inside the microchannel for all frequencies. Half the microchannel was imaged at  $z = 25 \mu\text{m}$ ,  $z = 50 \mu\text{m}$  and  $z = 100 \mu\text{m}$  above the bottom wall.

### 3.2.2 Pixels to ms<sup>-1</sup>

The flow measurement results were generated as pixel displacement. To convert these into displacement and velocity in SI unit's equations (16), (17) and (18) were used. The magnification factor  $M$ , is a function of the objective and the camera aperture. A 20x NA 0.4 microscopic lens and a 0.7 aperture was used for all the experiments. This produces a magnification factor of  $1 \times 10^{-6} \frac{m}{x_{px}}$  (i.e. 1 px = 1  $\mu$ m). Equation (17) gives the particle displacement. Equation (18) gives the velocity where  $\Delta t$  is the time interval between images.

$$M = \frac{m}{x_{px}} \quad (16)$$

$$x = x_{px} \times M \quad (17)$$

$$v = \frac{x_{px}}{\Delta t} \times M \quad (18)$$

### 3.2.3 Developing in plane velocity plots

The evaluated results are presented as contour plots of in-plane magnitude of the velocity as a function of time and the distance from the center. The following steps were completed to produce these plots from micro PIV data. The velocity oscillates around the mean flow. The velocity is in the positive streamwise (x) direction at all locations in the microchannel.

Figure 3.5 presents the step process involved in generating contour plots of in-plane magnitude of the velocity as a function of time and the distance from the center from micro PIV data, i.e  $u(y,t)$ . Sinusoidal flow waveforms were pumped through the microchannel. Initially, the data set contains resolved velocity in the imaging data plane (fig. 3.5(a)). All flow velocities are positive and along the x-axis. The velocity vectors in the imaging plane are constant at each single time point of the sinusoidal flow waveform. Therefore, the velocity field was averaged to obtain the average velocity at discrete (y) points at one time point. The aim is to evaluate the time varying flow velocity at discrete (y) points averaged along the (x) points (fig. 3.5(c)). The velocity profile,  $u(y)$ , at different time points of the flow waveform was determined (fig. 3.5(d)). By increasing the number of time points a vector plot of velocity as a function of time was developed (fig. 3.5(e)). The images were acquired at 10 kHz. Correlation averaging was used to average time varying flow rates to 100 time points. The vector plot is then converted to a contour plot giving the in-plane velocity, as a function of time and the distance from the center axis of the microchannel (fig. 3.5(f)).

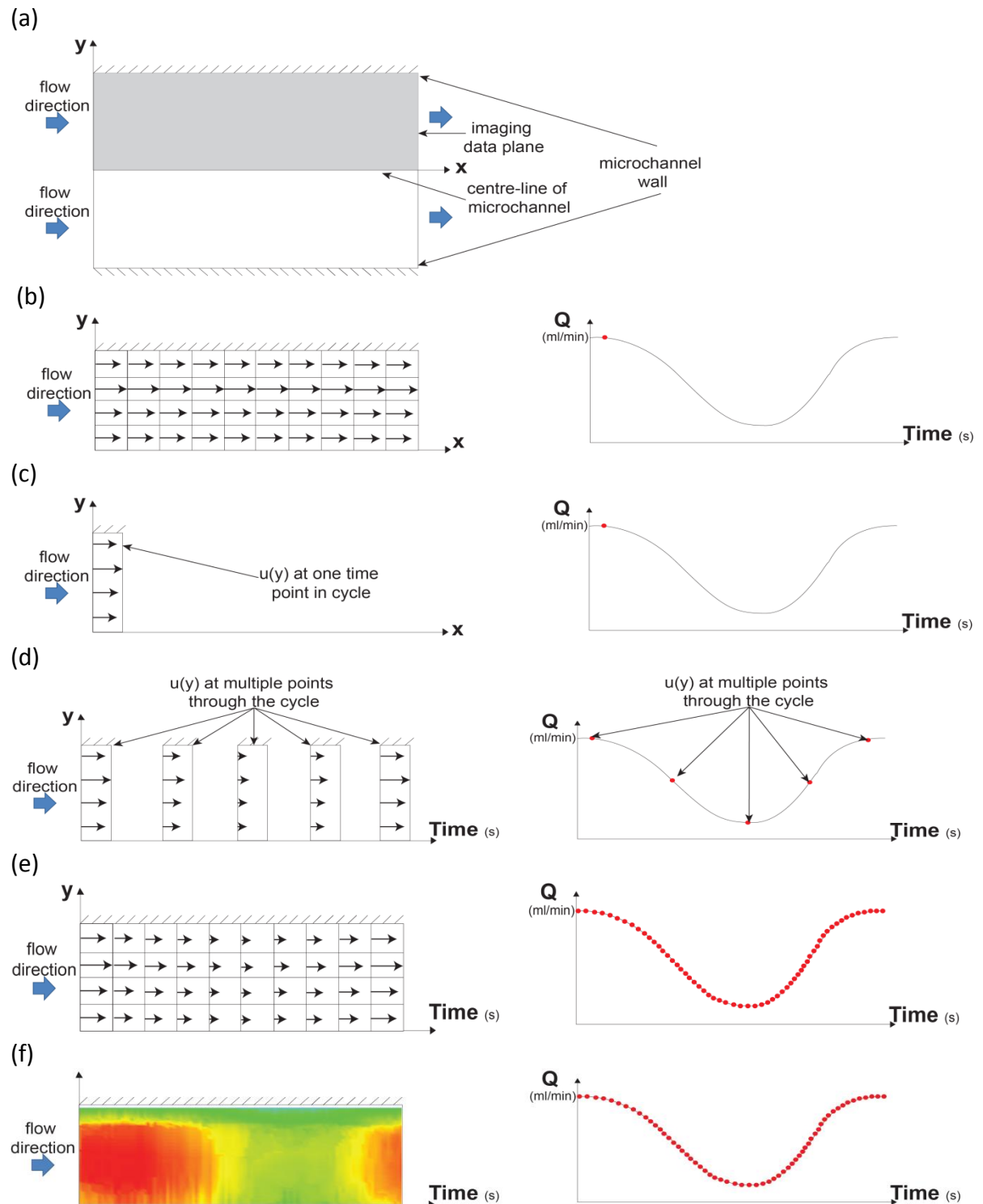


**Figure 3.5** Step process involved in generating contour plots of in-plane magnitude of the streamwise velocity as a function of time and the distance from the center from micro PIV data. (a) flow travels along the microchannel. (b) half a width of the microchannel was imaged extending from the center to the wall, the velocity field is constant at a single time point (c) time varying flow at discrete ( $y$ ) points averaged along the ( $x$ ) points. (d) velocity profile at different time points of flow waveform was determined. (e) final flow field showing  $u(y, t)$ . (f) vector plot is converted to a contour plot giving the in-plane velocity, as a function of time and the distance from the center axis of the microchannel.



## 3.3 Results & Discussion

### 3.3.1 Steady flow measurements

Figure 3.6 presents the steady flow velocity profile across the width of the microchannel. Results indicate a symmetrical parabolic velocity profile. The peak velocity has reduced with decreasing distance from the bottom of the microchannel wall. The lowest plane ( $z = 25 \mu\text{m}$ ) shows least symmetrical flow profile. This is due to the poor image quality produced when imaging near microchannel walls. The results confirm that the system and microchannel is free of manufacturing defects. The flow control technique does not introduce abnormalities to flow profiles generated inside microchannels for viscous fluids.

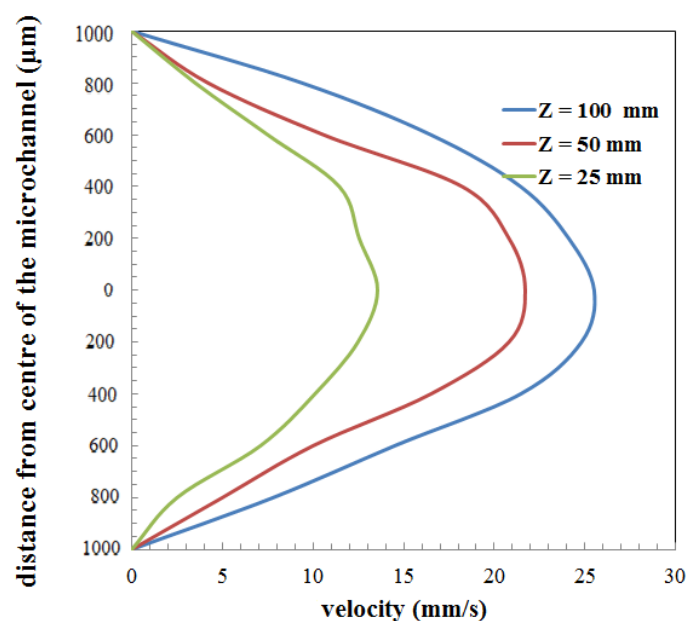


**Figure 3.6** Steady flow velocity profile across the width of the microchannel

### 3.3.1 Normalised input flow rate flow probe measurement

Figure 3.6 Presents the flow probe measurement of input flow rate averaged over 60 seconds plotted over one cycle. The flow probe measurements show slight increase of average flow rate from 1Hz to 2.5 Hz. The flow production error for each frequency produces a total harmonic distortion of under 2% and a root mean square error of under 8%.

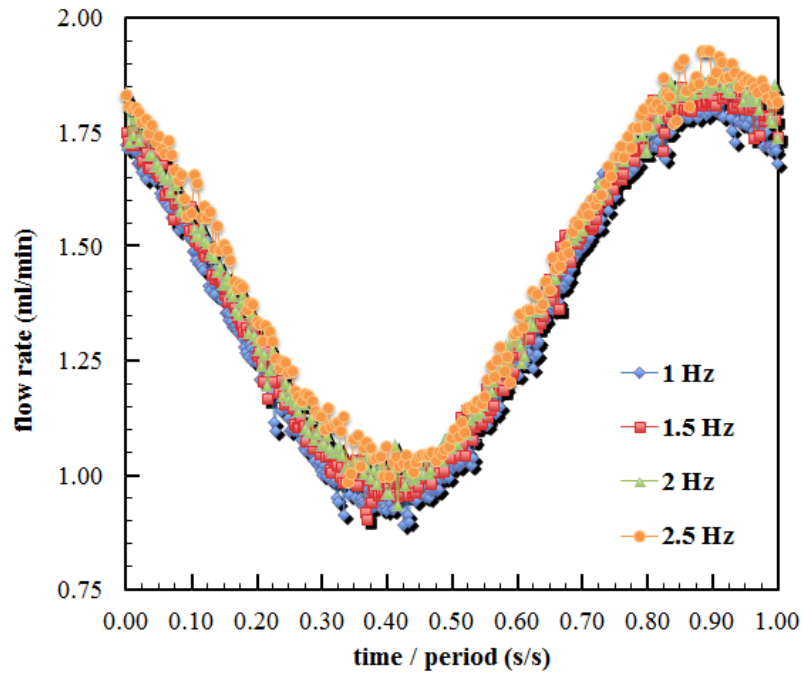


**Figure 3.6.** Flow probe measurement of input flow rate averaged over 60 seconds and plotted as a function of normalised time

### 3.3.2 Micro PIV results $z = 100 \mu\text{m}$

Figure 3.7 presents contour plots of the in-plane magnitude of the velocity at  $z = 100 \mu\text{m}$  above the bottom of the microchannel wall as a function of time and the distance from the center to the channel wall for sinusoidal waveforms at frequencies of 1 Hz, 1.5 Hz, 2 Hz and 2.5 Hz. Corresponding Reynolds number ( $Re$ ) and Womersley number ( $\alpha$ ) are noted for each plot. The flow clearly shows a pulsatile velocity profile with varying magnitude and profile,  $u(y)$ , over time. Steady flow in a rectangular microchannel exhibits Poiseuille flow. However, in these cases the velocity is close to parabolic but the maximum velocity seemingly exists slightly displaced away from the center. This is often observed in flow channels where viscous forces dominate shear forces (Sheen *et al.* 2008).

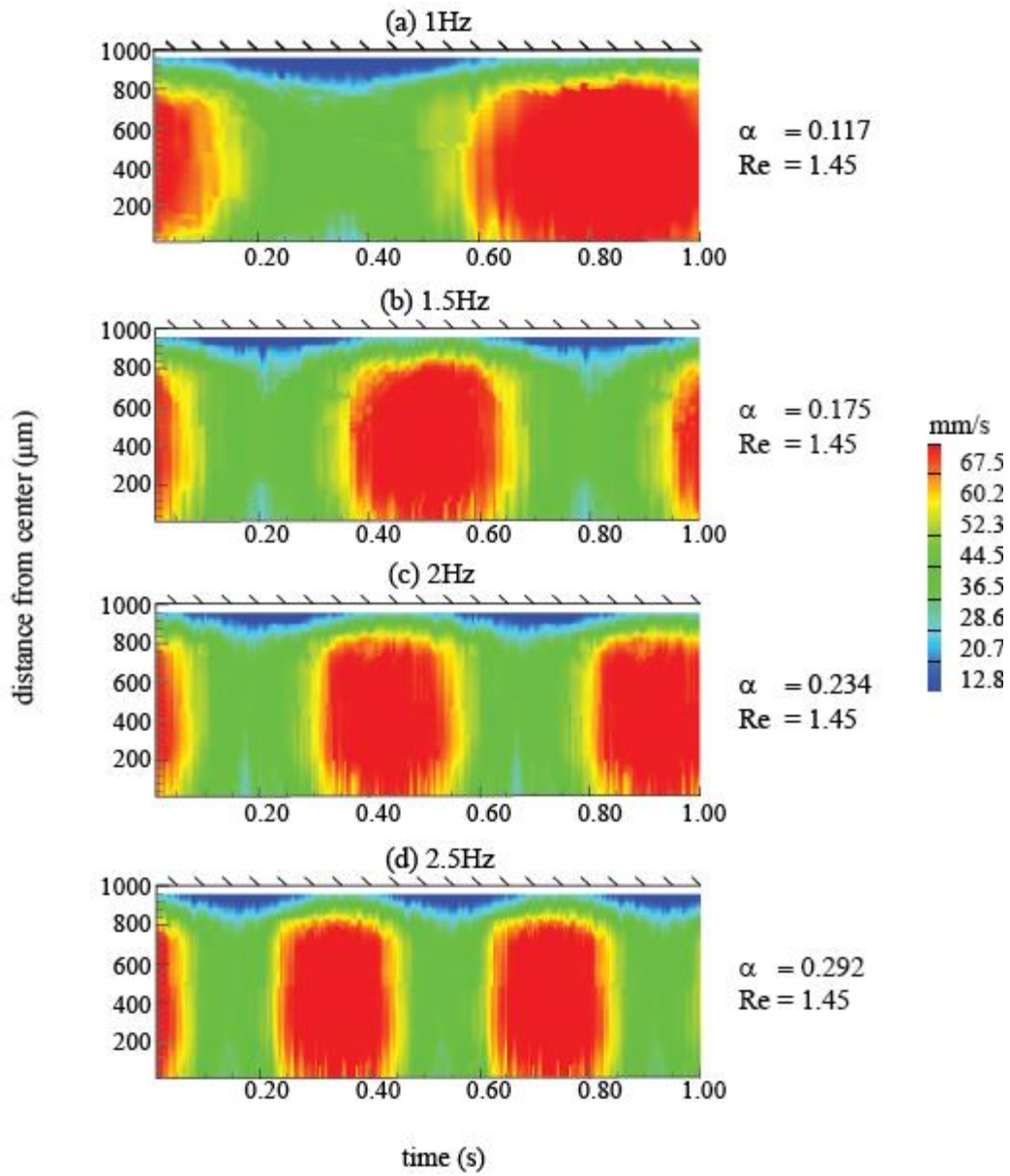


**Figure 3.7** Contour plots of in-plane magnitude of the velocity at  $z = 100 \mu\text{m}$  above the bottom of the microchannel wall as a function of time and the distance from the center for frequencies (a) 1 Hz, (b) 1.5 Hz, (c) 2 Hz and (d) 2.5 Hz. Corresponding Reynolds number ( $Re$ ) and Womersley number ( $\alpha$ ) are noted for each plot.

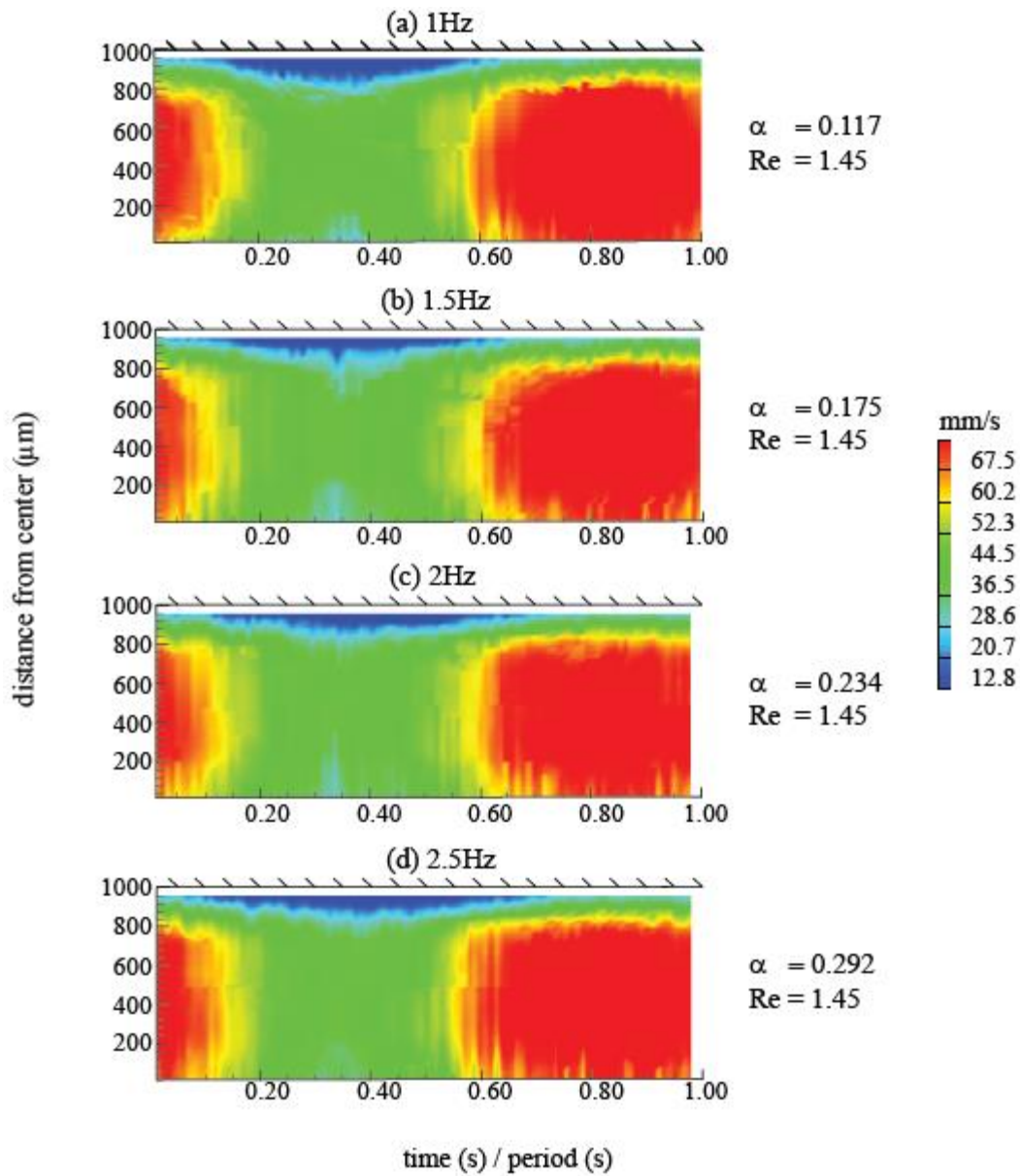


**Figure 3.8** Temporally Normalised contour plots of in-plane magnitude of the velocity as a function of time and the distance from the center for frequencies (a) 1 Hz, (b) 1.5 Hz, (c) 2 Hz and (d) 2.5 Hz at  $z = 100 \mu\text{m}$  above the bottom of the microchannel wall . Corresponding Reynolds number (Re) and Womersley number ( $\alpha$ ) are noted for each plot.

Figure 3.8 presents temporally normalised contour plots of in-plane magnitude of the velocity as a function of time and the distance from the center for frequencies (a) 1 Hz, (b) 1.5 Hz, (c) 2 Hz and (d) 2.5 Hz at  $z = 100 \mu\text{m}$  above the bottom of the microchannel wall. The data was normalised by dividing time from the period of each frequency. The temporally normalised velocity profiles are almost identical for the frequencies tested. With increasing frequency the duration of high velocity is marginally prolonged in normalised time ( $t/T$ ). This relates well to input flow data where the average velocity was observed to be slightly higher from 1 Hz to 2.5 Hz.

### 3.3.3 Micro PIV results $z = 50 \mu\text{m}$

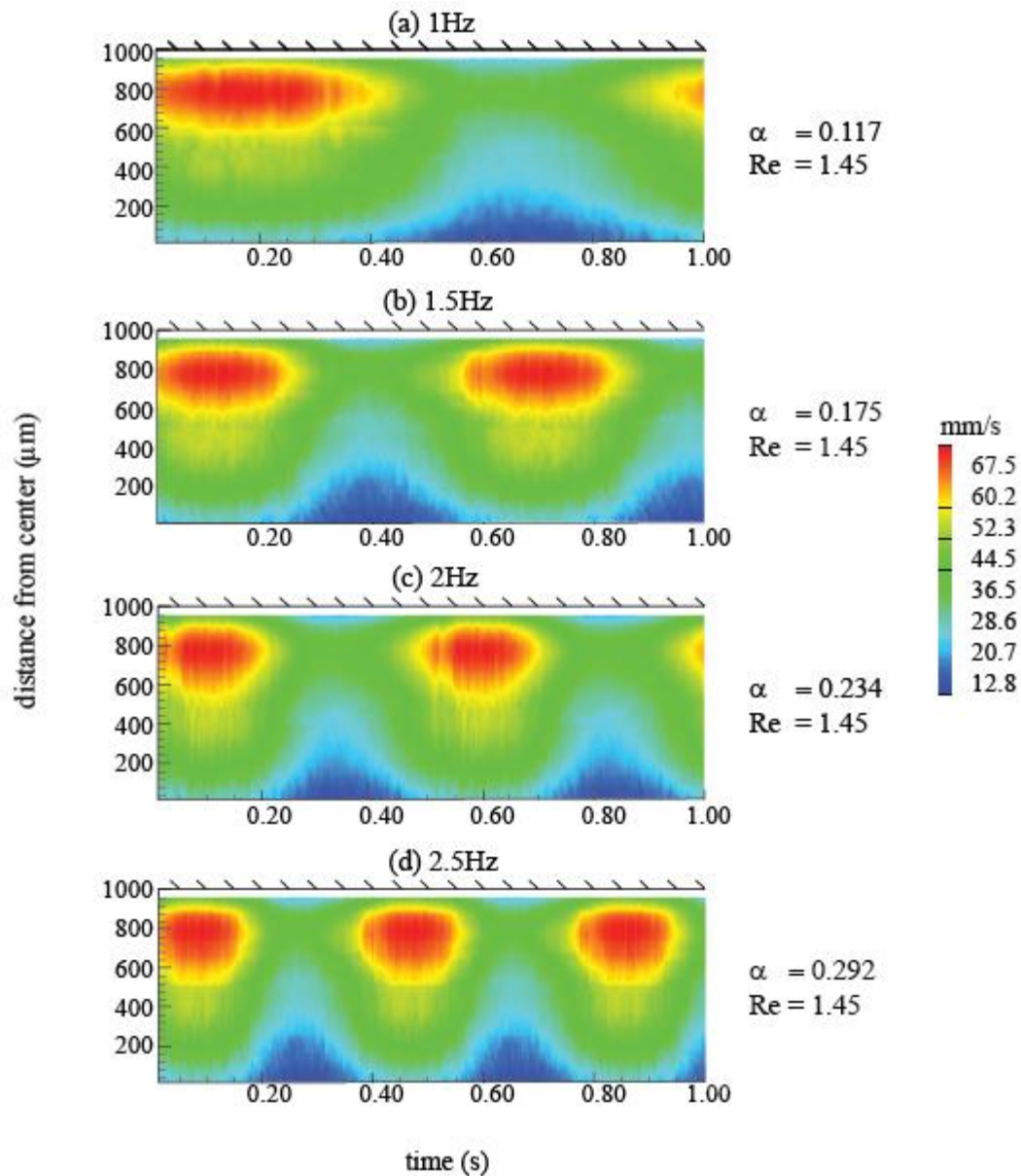


**Figure 3.9** Contour plots of in-plane magnitude of the velocity at  $z = 50 \mu\text{m}$  above the bottom of the microchannel wall as a function of time and the distance from the center for frequencies (a) 1 Hz, (b) 1.5 Hz, (c) 2 Hz and (d) 2.5 Hz. Corresponding Reynolds number ( $Re$ ) and Womersley number ( $\alpha$ ) are noted for each plot.

Figure 3.9 presents contour plots of in-plane magnitude of the velocity at  $z = 50 \mu\text{m}$  above the bottom of the microchannel wall as a function of time and the distance from the center for frequencies (a) 1 Hz, (b) 1.5 Hz, (c) 2 Hz and (d) 2.5 Hz. The velocity profile for  $z=50$  show less noise and a smoother velocity gradients than at  $z=100 \mu\text{m}$  and  $z = 25 \mu\text{m}$ . The smoother gradient is due to the smaller rate of change present in the  $z$  direction velocity profile. Higher velocity away from the center is higher indicating higher viscous effects at this plane.



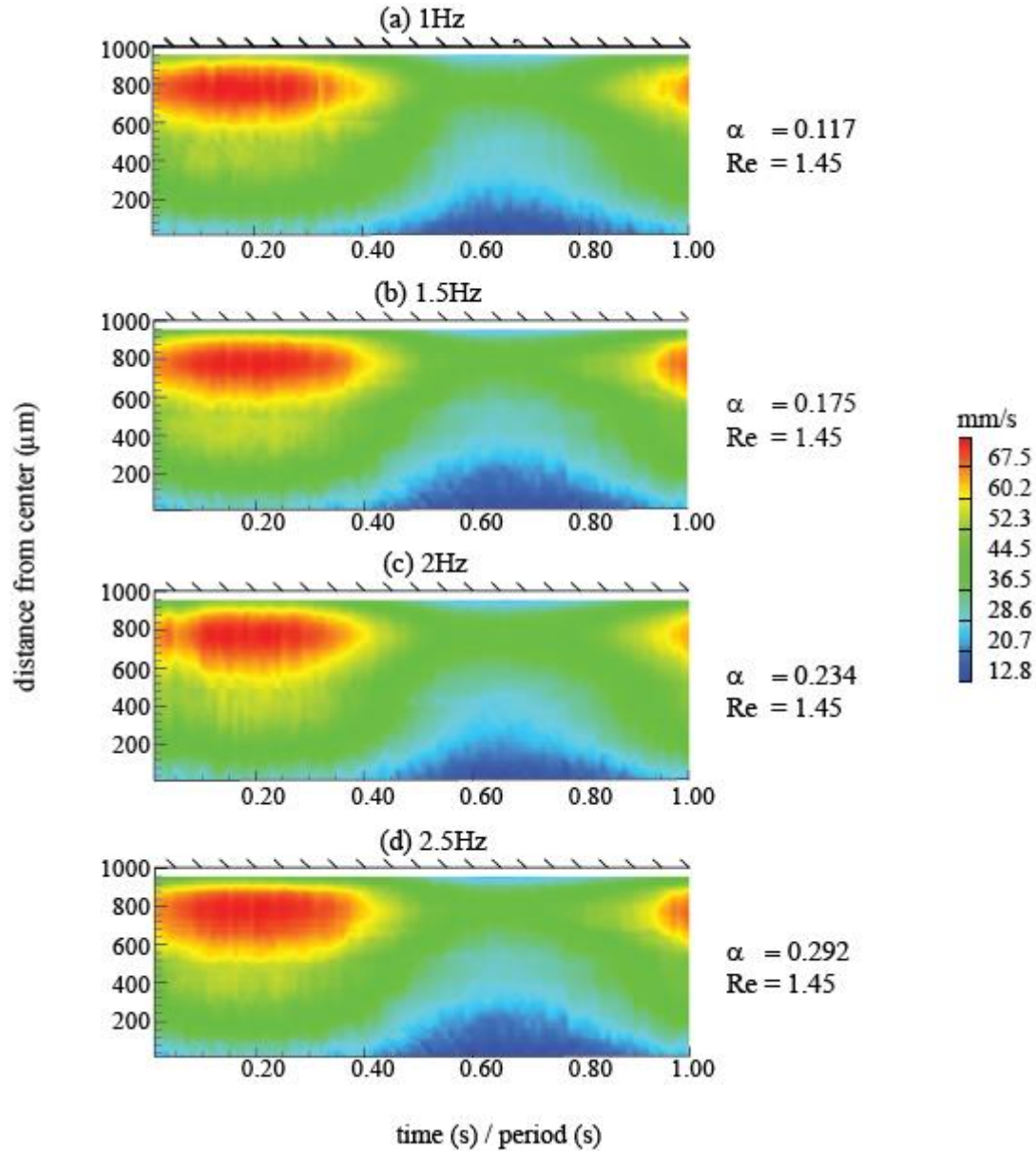


**Figure 3.10** Temporally normalised contour plots of in-plane magnitude of the velocity at  $z = 50 \mu\text{m}$  above the bottom of the microchannel wall as a function of time and the distance from the center for frequencies (a) 1 Hz, (b) 1.5 Hz, (c) 2 Hz and (d) 2.5 Hz. Corresponding Reynolds number ( $Re$ ) and Womersley number ( $\alpha$ ) are noted for each plot.

Figure 3.10 presents temporally normalised contour plots of in-plane magnitude of the velocity at  $z = 50 \mu\text{m}$  above the bottom of the microchannel wall as a function of time and the distance from the center for frequencies (a) 1 Hz, (b) 1.5 Hz, (c) 2 Hz and (d) 2.5 Hz. Similarly to  $z = 100 \mu\text{m}$  the temporally normalised velocity profiles are almost identical for the frequencies tested. The average magnitude of velocity was observed to be slightly higher from 1 Hz to 2.5 Hz.

### 3.3.3 Micro PIV results $z = 25 \mu\text{m}$

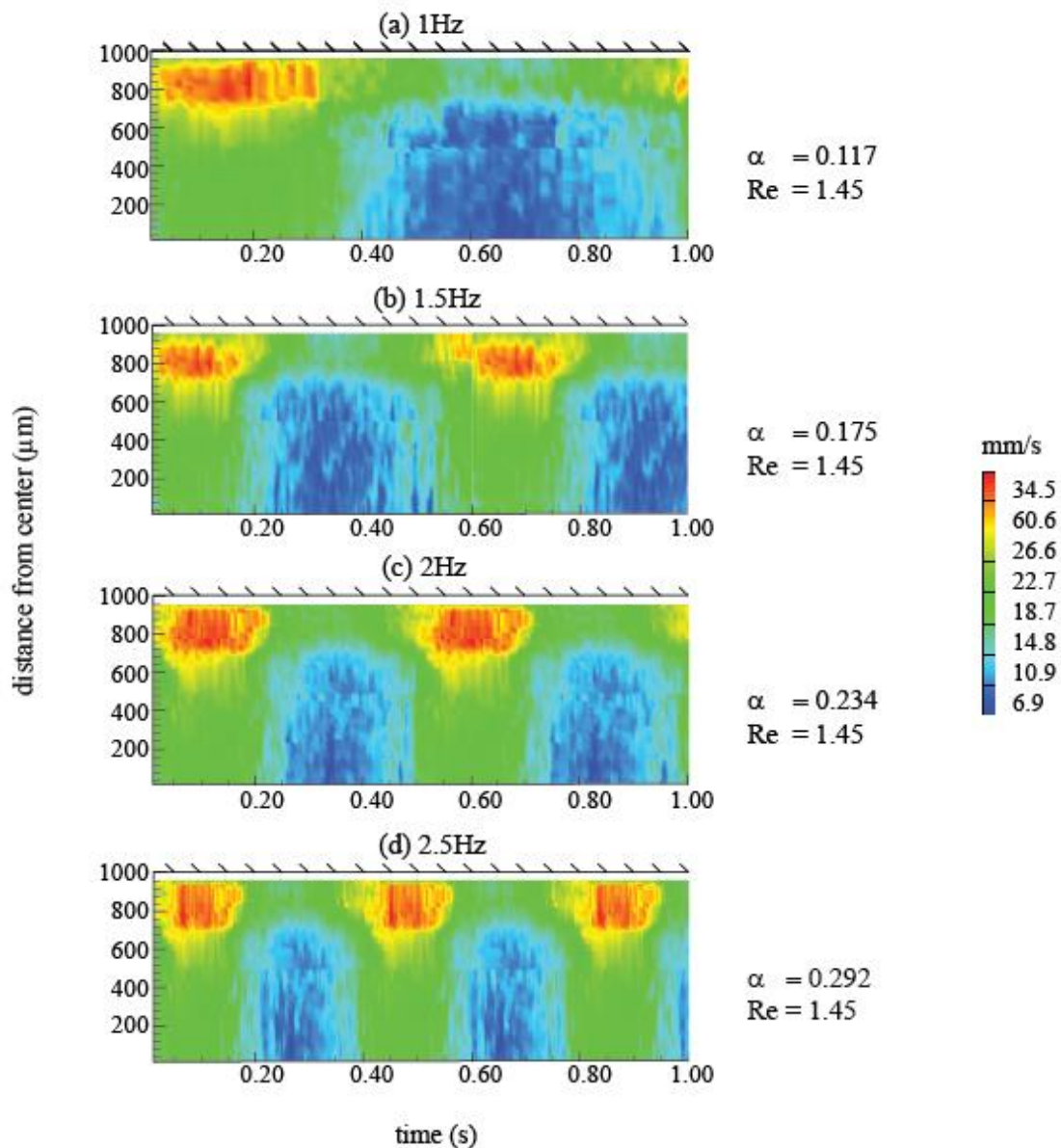


**Figure 3.11** Contour plots of in-plane magnitude of the velocity at  $z = 25 \mu\text{m}$  above the bottom of the microchannel wall as a function of time and the distance from the center for frequencies (a) 1 Hz, (b) 1.5 Hz, (c) 2 Hz and (d) 2.5 Hz. Corresponding Reynolds number ( $Re$ ) and Womersley number ( $\alpha$ ) are noted for each plot.

Figure 3.11 presents contour plots of in-plane magnitude of the velocity at  $z = 25 \mu\text{m}$  above the bottom of the microchannel wall as a function of time and the distance from the center for frequencies (a) 1 Hz, (b) 1.5 Hz, (c) 2 Hz and (d) 2.5 Hz. At  $z = 25 \mu\text{m}$  the particle image intensity is relatively low resulting in micro PIV measurements with a higher level of noise. The key features exhibited by the other plane  $z = 100 \mu\text{m}$  and  $z = 50 \mu\text{m}$  remain similar. Higher velocity is away from the center is higher indicating higher viscous effects. At a level of  $z = 25 \mu\text{m}$ , the flow would experience frictional forces from the bottom floor of the microchannel. The magnitude of the frictional forces increases with the viscosity of the fluid.

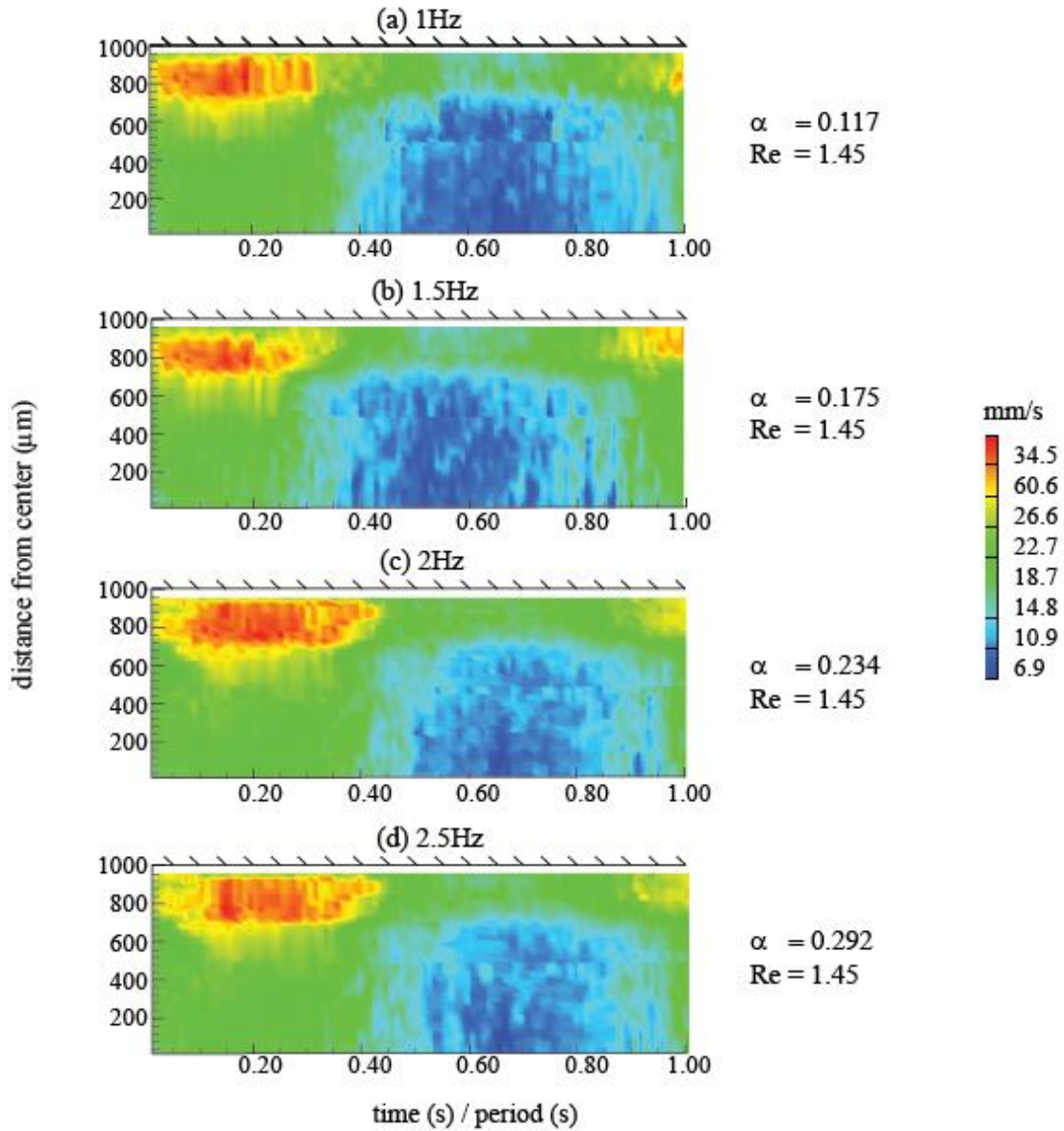


**Figure 3.12** Temporally normalised contour plots of in-plane magnitude of the velocity at  $z = 25 \mu\text{m}$  above the bottom of the microchannel wall as a function of time and the distance from the center for frequencies (a) 1 Hz, (b) 1.5 Hz, (c) 2 Hz and (d) 2.5 Hz. Corresponding Reynolds number ( $Re$ ) and Womersley number ( $\alpha$ ) are noted for each plot.

Figure 3.12 shows temporally normalised contour plots of in-plane magnitude of the velocity at  $z = 25 \mu\text{m}$  above the bottom of the microchannel wall as a function of time and the distance from the center for frequencies (a) 1 Hz, (b) 1.5 Hz, (c) 2 Hz and (d) 2.5 Hz. Similarly to  $z = 100 \mu\text{m}$ ,  $50 \mu\text{m}$ . The temporally normalised velocity profiles are almost identical for the frequencies tested.



### 3.3.3 Normalised micro PIV results for 1 Hz

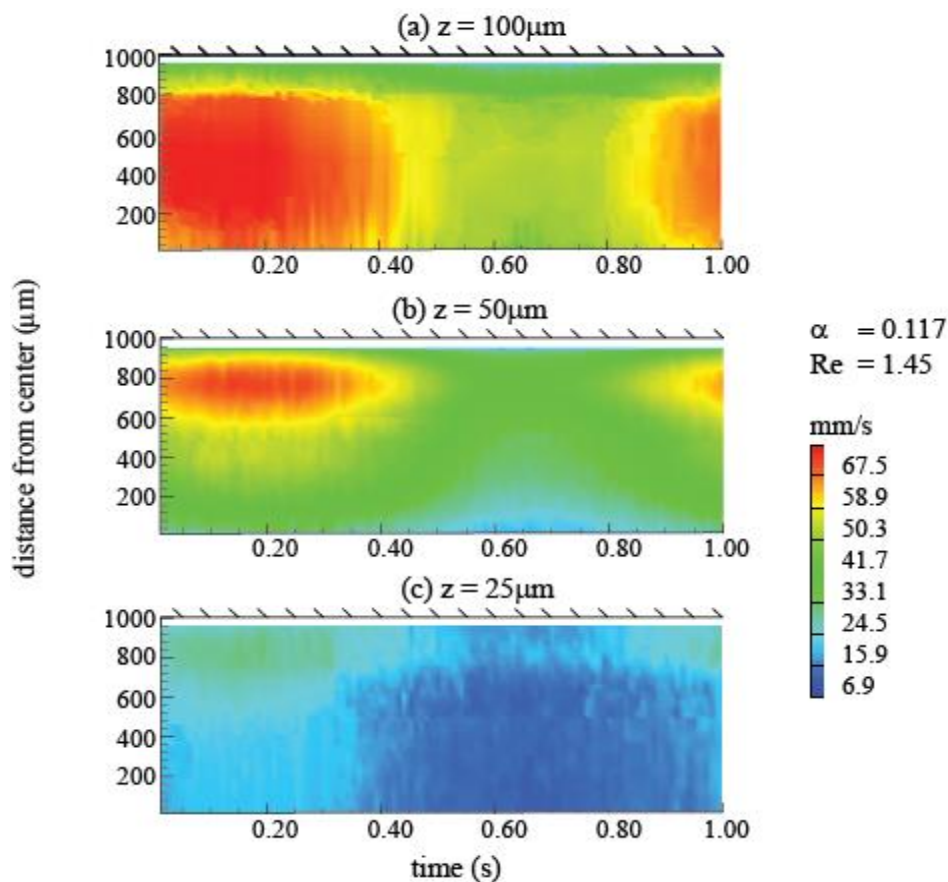


**Figure 3.13** Contour plots of in-plane magnitude of the velocity at (a)  $z = 100 \mu\text{m}$ , (b)  $z = 50 \mu\text{m}$ , (c)  $z = 25 \mu\text{m}$  above the bottom of the microchannel wall as a function of time and the distance from the center for frequencies of 1 Hz. Corresponding Reynolds number ( $Re$ ) and Womersley number ( $\alpha$ ) are 1.45 and 0.117 respectively.

Figure 3.13 presents contour plots of in-plane magnitude of the velocity at (a)  $z = 100 \mu\text{m}$ , (b)  $z = 50 \mu\text{m}$ , (c)  $z = 25 \mu\text{m}$  as a function of time and the distance from the center for the frequency of 1 Hz. The average magnitude of velocity of  $z = 100 \mu\text{m}$  is higher than  $z = 50 \mu\text{m}$  and  $z = 25 \mu\text{m}$ . This is a result of  $z = 100 \mu\text{m}$  plane experiencing lower viscous forces from the  $z$  axis wall (See figure 3.4 for planar location and axis orientation).

Steady flow in a rectangular microchannel exhibits Poiseuille flow as shown in figure 3.14 (a) (Lima et al. 2007). In our experiments higher velocity at on each plane is developed away from the center as shown in figure 3.14 (b). A micro pump designed by Sheen et al. (2008) exhibited a similar time varying velocity profile (Sheen et al. 2008). This can be hypothesised to be instigated by the development of Womersley flow within the microchannel. For viscous forces to alter flow, the Womersley number must be higher than 1. But these values are for circular channels. Our results show that for microchannels with an aspect ratio of 10:1, fluid viscosity of  $4 \times 10^{-3} \text{ N.s/m}^2$  and Womersley number between 0.117 - 0.2925 viscous forces appear to affect the flow profile.

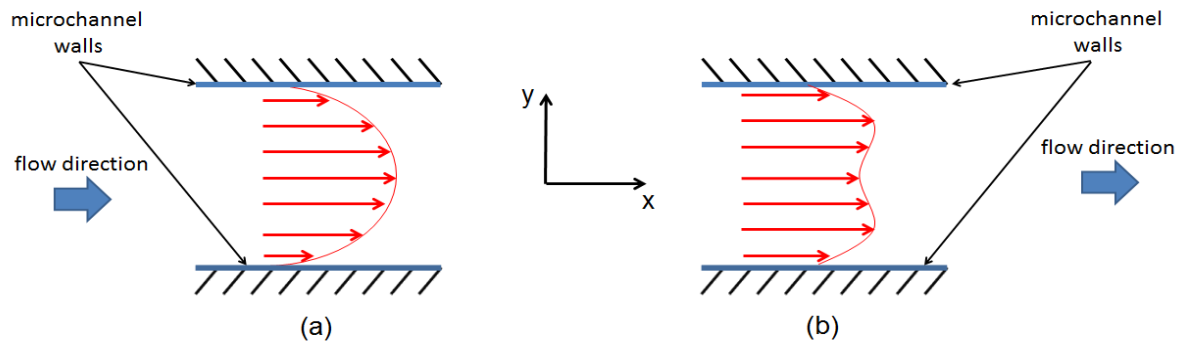


**Figure 3.14** (a) Poiseuille flow, (b) experimentally evaluated flow velocity profile developed inside a rectangular microchannel

### 3.4 Chapter conclusion

Micro PIV was used to evaluate the velocity profile inside the microchannel for steady and pulsatile flow. The steady flow experiments confirm that the flow control system and microchannel is free of manufacturing defects. The flow control technique does not introduce abnormalities to flow profiles generated inside microchannels for viscous fluids. In blood flow the velocity profile is greatly affected by the distribution of red blood cells (*Sherwood et al. 2014*). Therefore, it is recommended that further experiments are conducted to evaluate the effect of the flow control technique to the distribution of red blood cells.

Pulsatile sinusoidal waveforms of 1 Hz, 1.5 Hz, 2 Hz, 2.5 Hz were generated relating to the physiological heart rates of 60, 90, 120, 150 beats per minute. A mean shear rate of  $1800\text{s}^{-1}$  with an amplitude of 30% was used. The temporally normalised velocity profile is essentially independent of frequency for the range of frequencies tested. The maximum velocity of the plane seemingly exists slightly away from the center and consistent with a Womersley like velocity profile rather than a parabolic Poiseuille profile. These indicate for a 10:1 high aspect ratio microchannel with fluid viscosity of  $4 \times 10^{-3} \text{ N.s/m}^2$  and Womersley number between 0.117 - 0.2925, viscous forces affect the flow profile.

These experiments support the prototype flow control systems ability to generate pulsatile and physiologically flows with good control of frequency and amplitude. With this system in place our understanding of physiological flow mechanics can be improved by conducting experiments closely replicating in-vivo conditions.

## 4.0 Blood flow

In chapter 1, a new flow control technique was described and performance of the designed prototype system was evaluated. In chapter 2, the prototype system was used to produce experimental results showing the suitability of this technique in flow evaluation studies. This chapter presents experimental results demonstrating the suitability of the system to be used in microchannel based physiological studies. Thrombus growth experiments were completed for steady and pulsatile flow conditions. These thrombi were imaged with multi-photon confocal microscopy and analysed to quantify growth density and dimensional results. Significant differences were formed between steady and pulsatile flow conditions.

### 4.1 Background

Hemodynamics within the human body has shown to play a vital role in the development of many cardiovascular diseases. Research has revealed platelet activation, thrombus formation, stenosis and development of atherosclerosis to be linked to changes in hemodynamics (*Ku et al. 1985*). The developed system can be used solely, or as part of a cardiovascular model, to produce realistic physiological flow, enabling evaluation of these complex biological conditions.

#### 4.1.1 Blood flow and disease

Vascular diseases preferentially occur at sites of local flow interference within the human body (*Glagov et al 1988*). This suggests that hemodynamics processes play an important role in the development of disease (*Glagov et al 1988*). Research has shown that flow separation, low mean shear and oscillating wall shear to contribute towards Atheroma and Intimal Hyperplasia (*Kim et al. 2004*). *Ku et al. (1985)* showed flow patterns in the normal human carotid bifurcation differed from those associated with intraluminal disease. *Sinnot et al. (2006)* evaluated flow conditions between steady and pulsatile flow of a real magnetic resonance imaging derived diseases CDF model of a carotid artery bifurcation with rigid walls. The results revealed velocity and pressures across the stenosis to be higher for the pulsatile case (*Sinnot 2006*). These findings highlight the need to develop flow models capable of accurately replicating physiological flow and pressure levels.

Majority of research on platelet function has focused on bio-chemical stimuli, *Nesbitt et al. (2009)* showed platelets activation and subsequent thrombus formation to be both a mechanical and chemical process. Changes in hemodynamic forces are dominantly caused by changes in vessel geometry (*Nesbitt et al. 2009; Tolouei et al. 2011; Sinnot 2006*). Local geometry conditions such as branching, bending of blood vessels are primary regions of hemodynamic change. Additionally, regions of flow constrictions caused by a stenosis or thrombus formation exhibit critical changes in flow dynamics (*Nesbitt et al. 2009; Tolouei et al. 2011*). *Tolouei et al (2011)* showed a relationship between shear rate and dimensional growth of thrombi. The work

highlighted the need for experimentation to further understand the relationship between thrombus growth and physiological pulsatile flow. To develop an understanding of thrombosis, it is suitable to begin with identifying the mechanism in which platelet adhere to a microvessel.

#### 4.1.2 Platelet distribution in microvessels

The mechanical interaction between blood and the vascular wall is influenced by the velocity profile of the red blood cells flowing through the microvessel (Nakano A, 2005). Blood is mainly composed of red blood cells (RBCs) and plasma. This composition makes blood multiphase and non-newtonian in nature. Due these reasons it is difficult to accurately model blood flow through finite element models. In basic models, blood flow is considered to be incompressible and modeled using the Navier-Stokes equations. Boundary conditions are fixed by assuming rigid wall conditions. However, in nature vessels undergo spatial movement as well as elastic expansion.

In this cellular gradient, platelets, the smallest cellular component of blood, travel near the vessel wall while the erythrocytes and leukocytes travel near the center (Lopez et al. 1999). RBCs of different sizes travel at different speeds depending on their axial location in the blood stream. Cells near the vessel wall move significantly slower than those traveling at the center of the fluid stream. This is due to high viscous effects of the vessel wall as shown in the previous chapter. As RBCs travel through the vessel they are deformed drifting to the central axis of the vessel. This called the axial drift (Nakano et al. 2005). Aarts P.A et al (1998) showed that if RBCs were not present the platelets would follow a behavior known as “tubular pinch effect”. Figure 4.1 (a) shows the concentration profile of platelets without red blood cells. In blood flow under a normal concentration of platelets and RBCs, RBCs predominate in the axial stream. Conversely the disc-shaped platelets are margined along the vessel wall. At this location platelets are well positioned to monitor the integrity of the endothelium. To replicate this natural physiological condition, whole blood was used for all experiments in this chapter.

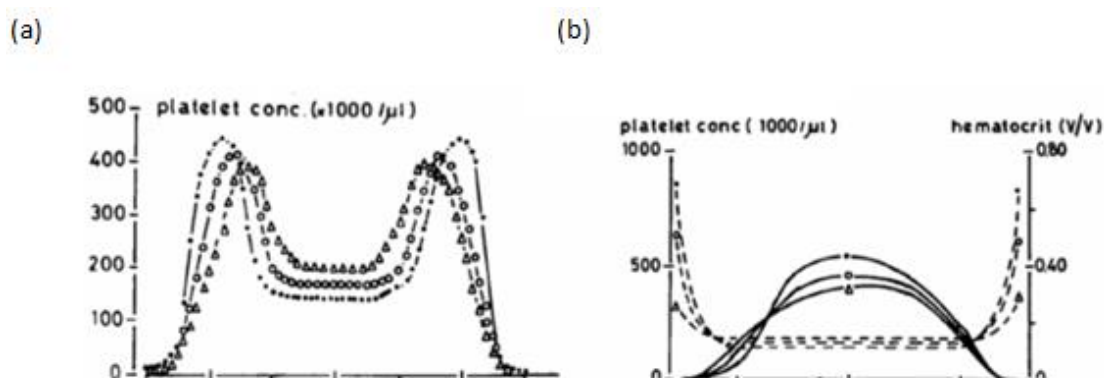


**Figure 4.1** Concentration profile of platelets (a) without ghost red blood cells developing tubular pinch effect. (b) with ghost red blood cells. Platelets are concentrated near the wall and RBCs at the center. Figure courtesy of (Aarts et al. 1988)

The endothelial layer consists of endothelial cells covered with glycocalyx to help reduce turbulence allowing blood to be pumped further (Nakano et al. 2005). Normally endothelium provides a non-adhesive surface to circulating platelets. However, when vessel wall injury occurs collagen fibers in the sub endothelium are exposed. The collagen actively interacts with adhesive platelet membrane surface receptors to initiate aggregation. Cardiovascular disorders may initiate undesired activation of these receptors leading to blood clots.

#### 4.1.3 Platelet aggregation process

Platelet aggregation, adhesion and subsequent thrombus formation heavily depends on shear rate. The hemodynamic shear within the human body varies from  $500 \text{ s}^{-1}$  to  $5,000 \text{ s}^{-1}$  and up to  $40,000 \text{ s}^{-1}$  in diseased and stenosed conditions (Bluestien et al. 1997).

Figure 4.2 presents the theoretical shear profile a platelet experience as it moves over an existing thrombus. Platelet aggregation begins with a sudden acceleration in shear. At this phase, the platelet undergo a dramatic shape change stimulating the development of membrane tethers promoting the formation of transient discoid platelet aggregates (Maxwell 2007; Nesbitt et al. 2009). In successive exposure to decelerating shear, these tethers physically restructure, increasing the strength and stability of discoid platelet aggregates (Maxwell 2007; Nesbitt et al. 2009). This restructuring process promotes thrombus growth (Nesbitt et al. 2009).

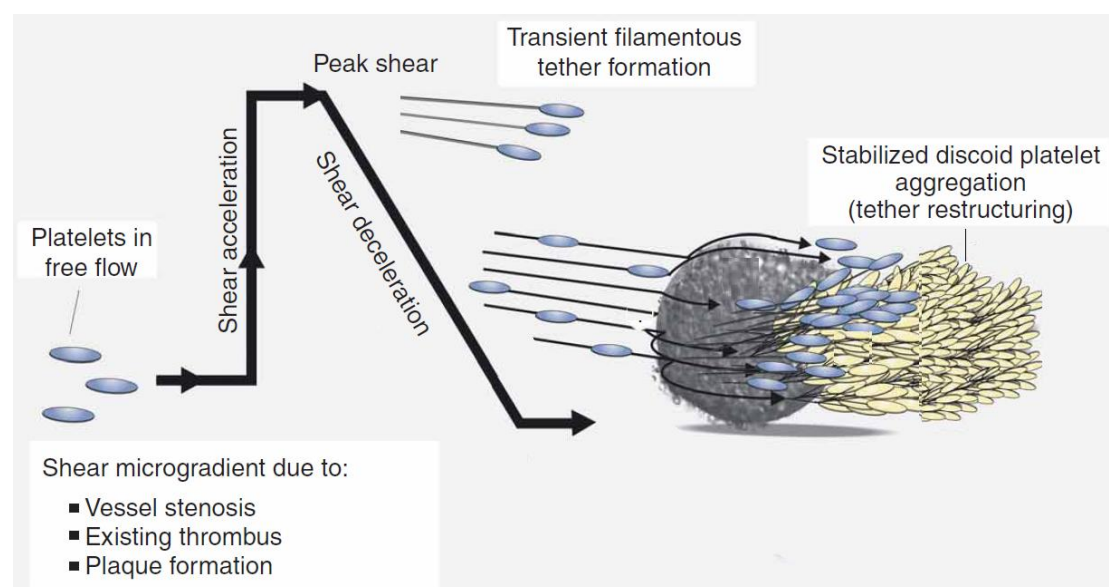


**Figure 4.2** Process of platelet aggregation. During shear acceleration platelets undergo a dramatic shape change forming filamentous membrane tethers. In successive exposure to decelerating shear, these tethers physically restructure, increasing the strength and stability of discoid platelet aggregates. This restructuring process promotes thrombus growth. Figure courtesy of (Nesbitt et al. 2009).

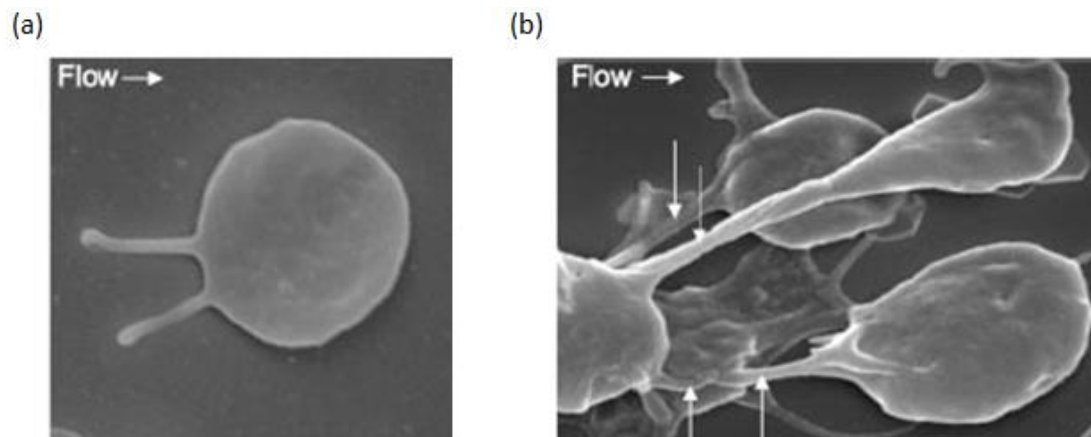


**Figure 4.3** Electron microscopy images of (a) tether formation of a platelet (b) a group of platelets adhering to each other the membrane tethers. Figure courtesy of (Jackson 2007)

Figure 4.3 (a) presents electron microscopy image of tether formation of a platelet. Figure 4.3 (b) presents a group of platelets adhering to each other via the membrane tethers as shown by arrows.

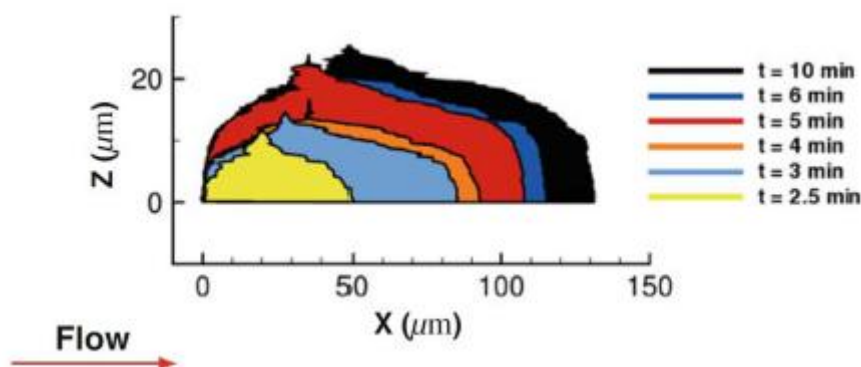


**Figure 4.4** Cross sectional area of thrombus growth over a 10 min time period. Figure courtesy of (Tolouei et al. 2011)

Platelet adhesion is initiated by exposure to collagen but the extent of thrombus growth is shear dependent. These complimentary processes make it hard to model thrombus growth. Figure 4.4 shows the cross sectional area of thrombus growth over time period of 10 minutes (Tolouei et al. 2011). Platelet bonding is achieved when adhesion receptors on a platelet attaches to ligands. Ligands act like bridges to bind neighboring platelets together. At different shear ranges platelets use different adhesion receptors and ligands (Jackson 2007).



Characteristic Features	Low shear < 1000 s <sup>-1</sup>	High Shear < 10,000 s <sup>-1</sup>	Extreme Shear >10,000 s <sup>-1</sup>
Adhesion receptor	Integrin $\alpha_{IIb}\beta_3$ (GP Ia-IIa)	Integrin $\alpha_{IIb}\beta_3$ (GP Ia-IIa), GP IV	GP Ib-V-IX
Activation dependent	Yes	Yes	No
Tether formation	No	Yes	Yes
Ligand	Fibrinogen	VWF, Fibrinogen, Fibronectin	VWF
Platelet Morphology	Sphere and filopodia	discoid	Smooth spherical

**Table 4.1** Summary of adhesion receptors and ligands used at different shear rates. Table courtesy of (S.P Jackson 2007).

Table 4.1 presents a summary of adhesion receptors and ligands used at different shear rates. For low shear rates binding of platelets is considered to occur via the Integrin  $\alpha_{IIb}\beta_3$  (GP Ia-IIa) receptor with fibrinogen. Activated platelets undergo shape change forming spheres with filopodia for stable aggregation (Jackson 2007). For high shear Integrin  $\alpha_{IIb}\beta_3$  (GP Ia-IIa) receptor allows for further binding to collagen via the GP VI receptor. Initial formations of aggregates occur between discoid platelets assisted by formation of membrane tethers. The membrane tethers help the aggregates to stabilise (Jackson 2007). At extreme shear platelets form smooth spheres and rolls over the surface (Jackson 2007). The receptors Integrin  $\alpha_{IIb}\beta_3$  and GP VI, becomes insufficient to initiate binding to collagen. For extreme shear, binding of the GP Ib-V-IX receptor to Von Willebrand factor becomes more essential for platelet adhesion. In addition to adhesion of receptors, platelet activation stimulates the formation other aggregating agents such as ADP, Thombixin A2 and Thrombin which promote further platelet activation.

#### 4.1.4 Stenosis

Undesired platelet activation due to shear microgradients occur due to stenosed vessel conditions. Lee B. Y. (1978) conducted studies on the effects of varying degree of stenosis on arterial pulsatile waveforms. The study showed with increasing degree of stenosis, the deceleration phase of the flow and pressure cycle occurs earlier than normal. Lee B. Y. (1978) hypothesised that there would be alterations in hemodynamic pulsatile flow and the pressure pattern even in early stages of occlusive diseases. Therefore, obtaining a better understanding of profiles and periods of pulsatile flow and pressure under stenosed conditions would aid in the development of valid clinical tests for early detection of vascular diseases. It would also be beneficial for pre and post operative evaluation of reconstructive arteries (Lee et al. 1978). The most common cause of vessel stenosis is a condition known as atherosclerosis.

#### 4.1.5 Atherosclerosis

Atherosclerosis is the build-up of fatty deposits on wall of the arteries. It the most common condition affecting arteries leading to stroke and heart attack. Figure 4.5 shows the progression of atherosclerosis.

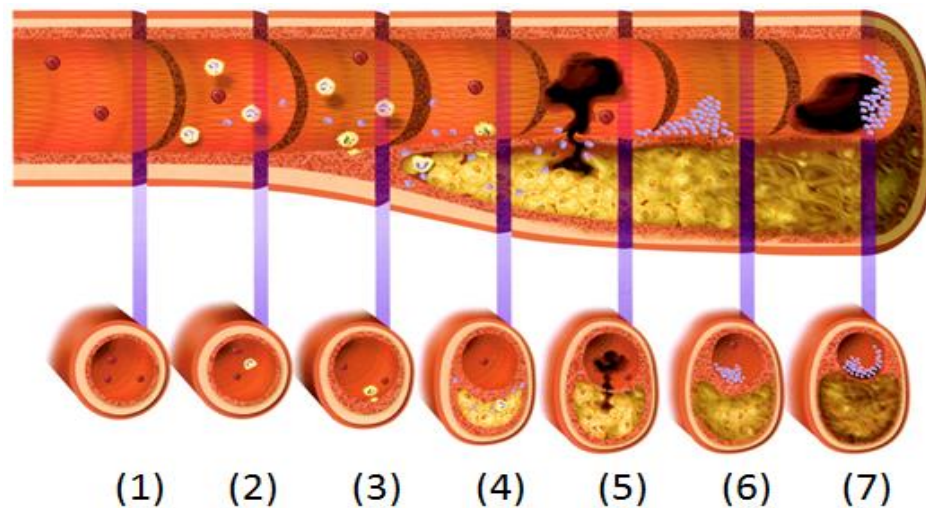


**Figure 4.5** The progression of atherosclerosis. Figure courtesy of (Libby 2001).

- (1) Healthy blood vessel
- (2) Due to bad habits such as high cholesterol, smoking and diabetes the level of LDL-C (bad cholesterol) increases over the HDL-C (good cholesterol which control LDL-C).
- (3) This excess bad cholesterol is absorbed in to the walls of arteries forming foam cells. The accumulation of foam cells can be seen by fatty streaks on the vessel wall.
- (4) As the fatty streaks grow the body defends itself by surrounding it by a fibrous capsule forming a plaque. As the plaque expands arteries narrower, leading to reduced or blocked blood flow. Over time calcium may be deposited in the plaque, reducing the vessels elasticity and increasing vulnerability.
- (5) Reduced blood flow increases pressure causing the plaque to rupture. This exposes smooth muscles and collagen fibres promoting platelet aggregation forming thrombi inside the artery.
- (6) This blood clot can suddenly block all blood flow through the artery.
- (7) It can also break off and travel through the bloodstream to block another artery elsewhere. Blockage of an artery to the heart causes a heart attack, while blockage to the brain causes a stroke.



#### 4.1.6 Factors effecting blood viscosity

The viscoelastic properties of blood play a vital role in developing the local velocity profile inside a vessel. This was highlighted in the micro PIV experiments presented in the previous chapter. This attribute is influenced by several conditions.

- **Shear rate**

Blood is a viscoelastic fluid that behaves as a non-newtonian fluid for shear rates below  $500 \text{ s}^{-1}$ . At shear rates less than  $50 \text{ s}^{-1}$ , viscosity of blood increases exponentially due to the formation of large aggregates of erythrocytes (Long *et al.* 2005). Figure 4.6 shows experimental results of shear rate vs. shear stress for blood with 40% hematocrit. The results indicate that for very high shear rates blood exhibits Newtonian properties.

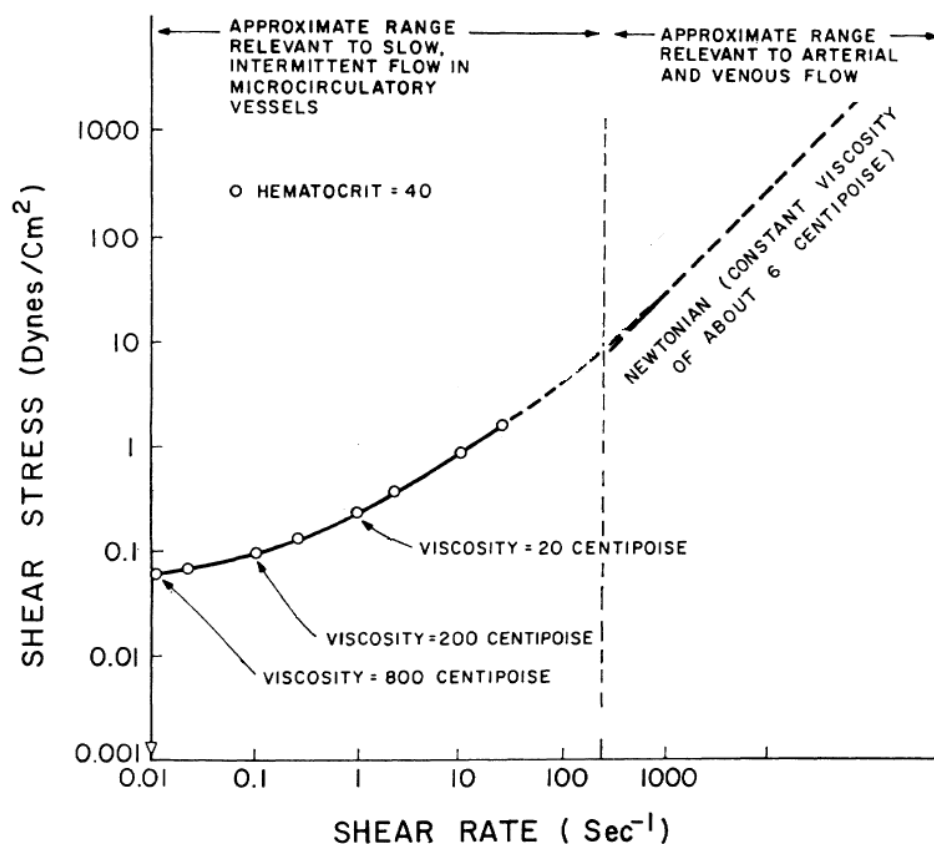


**Figure 4.6** Shear rate vs. shear stress of blood with 40% hematocrit (Replogle 1967).

- **Red blood cell deformability**

Red blood cells deform as forces are applied. Deformability allows cells to squeeze through small vessels. Therefore, viscosity increases with decreasing deformability.

- **Temperature**

The optimal temperature for platelet function is 37 °C. Temperature over this limit leads to increased hemolysis (Ratner 2000).

- **Hematocrit & Plasma level**

Corpuscles to plasma protein concentration influences the viscosity and elasticity of whole blood. The viscoelastic behavior of blood increases rapidly with increasing hematocrit as direct cell to cell interactions become more likely. At low velocity this relationship is linearly while at high velocity it is nonlinear (*Long et al. 2005; Thurston 1989*).

- **Vessel size**

Fahraeus and Lindqvist (1931) showed that blood viscosity reduces with reducing diameter for vessels between 10  $\mu\text{m}$  and 300  $\mu\text{m}$ . This is known as the Fahraeus–Lindqvist effect (*Fahraeus & Lindqvist 1931*). The effect is caused by the RBCs traveling in an axial drift and pushing the plasma to form a sleeve between the RBCs and the wall.

- **Vessel wall roughness**

Endothelial roughness is negligible in larger arteries, In small vessels where roughness is substantial the flow rate is too low for roughness to have much effect

## 4.2 Methods

This section describes the methodology followed to grow thrombi inside microchannels using the developed prototype flow control system. Thrombus growth procedure developed by Tolouei et al (2011) and microchannel coating procedure developed by Colace et al. (2010) were followed. All procedures involving collection of human blood were approved by the Monash University Standing Committee on Ethics in Research involving Humans.

### 4.2.1 Experimental Procedure

The experimental procedure involves bio-chemical preparation, bio-chemical microchannel coating, experimental preparation and setup as outlined below.

#### *Bio-chemical Preparation*

1. Collagen produced by mixing 700  $\mu\text{g}/\text{ml}$  bovine type 1 collagen with 3  $\text{mg}/\text{ml}$  of acetic acid.
2. Tyrodes buffer prepared by mixing appropriate quantities of chemicals as listed in table 4.2. Tyrodes buffer is an interstitial fluid which assists in transferring nutrients and removal of waste for cells and tissue.

Materials	Per Liter of distilled water
Sodium Carbonate ( $\text{NaHCO}_3$ )	1.008 g
HEPES buffer	10 mL
Sodium Chloride ( $\text{NaCl}$ )	8.0063 g
Potassium Chloride ( $\text{KCl}$ )	0.2013 g
D-Glucose	0.9909 g
Calcium Chloride ( $\text{CaCl}_2$ )	0.111 g
Bovine Serum Albumin (BSA)	0.5 g
Apyrase enzyme	44.44 $\mu\text{g}$

**Table 4.2** List of chemical and quantities required for producing Tyrodes buffer. Tyrodes buffer is a balanced aqueous solution of salt and glucose. Its osmotic pressure and ion concentration is similar to blood plasma. In experiments it used to act as a barrier protecting blood from the atmosphere.

- Fixative solution prepared by diluting 40% formaldehyde solution with Tyrode's buffer at 8% (v/v). This fixative is used to fix the developed thrombi inside the microchannel.
- Anticoagulant prepared by reconstituting 5 mg vial D-Phenylalanyl-L-Prolyl-L Arginine Chloromethyl Ketone with 1 ml of saline. This was used to prevent blood from clotting immediately allowing for completion of the experiment.

#### Experimental Preparation

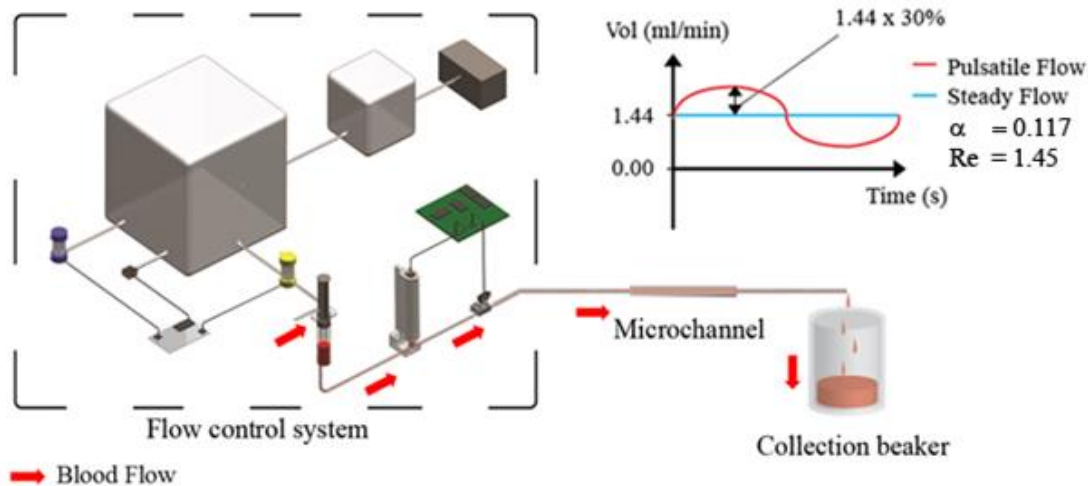


**Figure 4.7** Experimental setup for the thrombus growth. With the use of the prototype flow control system, blood was driven through a bio-chemically treated microchannel at a mean flow rate of  $Q_m = 1.44 \text{ ml/min}$  and an upstream shear rate of  $\gamma = 1800 \text{ s}^{-1}$ . Blood was allowed to run for 7 min enabling thrombus growth inside the microchannel. Fixative solution was then added to the reservoir allowing 5 ml of fixative solution to run through the microchannel at a low flow rate.

1. Microchannels were washed and coated with sigmacote and allowed to dry under a range hood for 24 hrs to create a hydrophobic surface for protein absorption.
2. Microchannels are washed out to remove excess hydrochloric acid and coated with bovine collagen type 1 and allowed to dry for 2.5 hrs to create the protein absorption surface.
3. Post 2.5 hrs the microchannels are washed out and tubing fixed.
4. The experimental system is setup in preparation for the experiment as shown in figure 4.7.
5. 180  $\mu$ L Anticoagulant is transferred to a tube to which contains 50 ml of human blood.
6. The tube was placed in the water bath which was set to 37°C to allow for blood to maintain appropriate temperature.
7. The system was completely flushed out with tyrodes buffer taking care to remove any trapped air. Air bubbles disrupt flow and destroy formed thrombi.
8. Blood was drawn in allowing it to fill in just before the microchannel entrance.
9. Blood is pumped using the prototype flow control system at a mean volume flow rate of  $Q_m = 1.44$  ml/min to meet the  $\tau = 1800$  s<sup>-1</sup> upstream shear rate inside the 2 mm x 0.2 mm microchannel.

Wall shear rate ( $\gamma$ ) in a rectangular channel can be approximated as,

$$\tau = \frac{6Q_m}{wh^2} \quad (15)$$

where,

$Q_m$	blood volume flow rate through the microchannel
$w$	microchannel width
$h$	microchannel height

For pulsatile flow, blood was pumped with a sinusoidal waveform of 1 Hz with an amplitude of 30% of the mean flow rate of  $Q_m = 1.44$  ml/min. This corresponds to a Reynolds number (Re) of 1.45 and a Womersley number ( $\alpha$ ) of 0.117 respectively.

10. Blood was allowed to run for 7 min enabling thrombogenesis inside the microchannel.

11. Fixative solution was then added to the reservoir allowing 5 ml of fixative solution to run through the microchannel at a low flow rate.
12. The microchannel is disconnected from both ends and sealed off.
13. All tubes and reservoirs were replaced in preparation for the next experimental run.
14. This process was repeated for steady and pulsatile flow.

#### 4.2.2 Thrombi Staining procedure

Chemical staining was used to biologically tag the platelet membrane enabling clear identification and evaluation of thrombi. Dihexyloxacarbocyanine Iodide ( $\text{DiOC}_6$ ) dye is a cell-permanent, green-fluorescent, lipophilic dye that is selective for the mitochondria of live cells specifically platelets, when used at low concentrations. The staining procedure consists of injecting it into the microchannel and allowing it to sit for 10 seconds and washing it out.

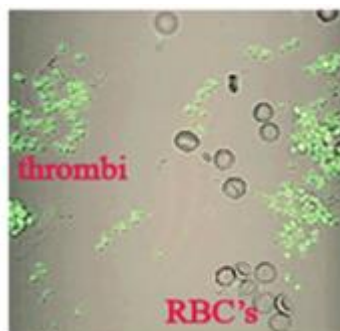


**Figure 4.8** Image of fluorescing thrombi superimposed on to the bright field image

The dye ( $\text{DiOC}_6$ ) was prepared from diluting 10 mg of dye powder ( $\text{DiOC}$ ) with Dimethyl sulfoxide (DMSO), Ethanol and Phosphate saline buffer (PBS). Ethanol was used as the primary diluting agent as  $\text{DiOC}_6$  is a hydrophobic molecule. The Dihexyloxacarbocyanine Iodide ( $\text{DiOC}_6$ ) dye is produced by following the procedure below.

1. 10 mg of dye powder ( $\text{DiOC}$ ) was dissolved in 1 ml of Dimethyl sulfoxide (DMSO) to produce 175mM DMSO stock.
2. 1/100 dilution with DMSO stock Ethanol to produce the master stock.
3. 1/100 dilution with the master stock and Ethanol to produce the working stock.

4. 1/100 dilution with working stock with PBS to produce the experimental dye solution.

Once stained, platelets would fluoresce under a blue monochromatic laser as shown in figure 4.8. The figure shows the bright field image superimposed on to the fluorescence image. Thrombi are fluorescing in green.

#### 4.2.3 Thrombi imaging procedure

Multiphoton confocal microscopy was used to image the “tagged” thrombi. An inverted confocal microscope similar to figure 4.9 at Monash Micro Imaging (MMI) was used to acquire a series of image stacks.

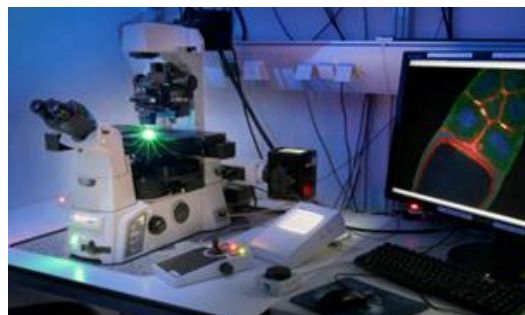


**Figure 4.9** Inverted confocal microscope setup used for biological cell imaging. Figure courtesy of Prismatic Solutions (2012).

To distinguish thrombi growth between steady and pulsatile flow, number of key characteristics were evaluated as listed below.

1. Density of thrombi growth along the microchannel between steady and pulsatile flow. Density is considered as the area of the sample covered with thrombi
2. Population distribution of thrombi area developed under steady and pulsatile flow.
3. Thrombi height between steady and pulsatile flow at middle and the wall of the microchannel.

Overlapping Images were acquired in the x-y plane along the microchannel and in  $\Delta z$  plane increments as shown in figure 4.10.

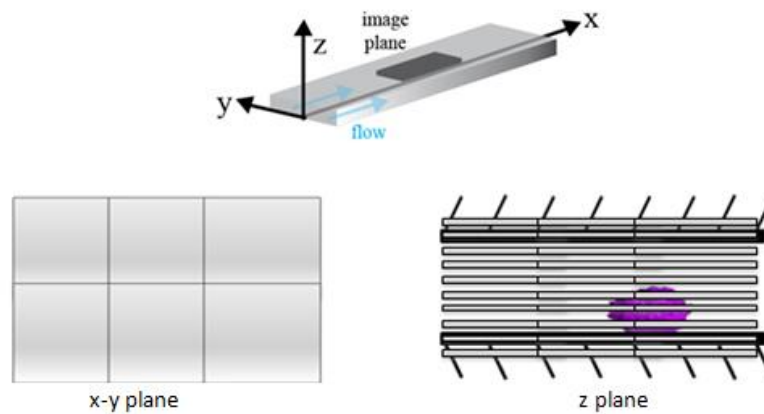


**Figure 4.10** Overlapping Image acquired in the x-y plane along the microchannel and  $\Delta z$  plane increments.

Thrombi characteristic	x-y Plane		z Plane
	Magnification	Overlapping	$\Delta z$
Density & Population dist.	20x	15%	20 $\mu\text{m}$
Height	40x	15%	0.5 $\mu\text{m}$

**Table 4.3** Imaging properties for x-y plane and z plane for each thrombi evaluation characteristic.

Table 4.3 presents imaging properties for x-y plane and z plane for each thrombi evaluation characteristic. To evaluate the population distribution of thrombi area, images were acquired at a lower magnification of 20x. To evaluate the height of thrombi, a higher magnification of 40x was used. This reduces the depth of focus increasing the accuracy of measurement. Generally platelets are 2 – 4  $\mu\text{m}$  in size. By acquiring image stacks of  $\Delta z$  at 0.5  $\mu\text{m}$  the error of the height measurement was only  $\pm 0.5 \mu\text{m}$ .

#### 4.2.4 Image Processing

Through staining only thrombi are captured in fluorescence imaging. All other biological and non-biological substances are non-fluorescing. This improves signal to noise ratio and overall image quality. The small size of the microchannel makes it difficult to obtain completely flat z-plane images. The confocal microscope acquires images by sweeping the laser across the sample. These contributors results in uneven illumination across the images. At each z level only a certain area of the microchannel will be illuminated. By utilizing the z plane image stacks the maximum projection can be produced from FIJI imaging software. This projection is the combined image of all the highest intensities in each pixel address of the z plane image stack. The resulting image has the total illumination of thrombi and the total noise. This noise can be easily removed from a combination of inbuilt Matlab filtering functions without loss of data.

To remove non-uniform background illumination, image processing code based on Matlab's "imopen" function was developed. This function utilizes the morphological opening to estimate the background illumination. Morphological opening performs basic erosion and subtle dilation on greyscale images. Erosion removes some of the foreground (bright) pixels from the edges of objects. Dilation fills out pixels to preserve the shape and size of the larger objects on the image. For this application, objects are thrombi. The effect of the morphological opening is determined by a structuring element. The structuring element is the minimum threshold size of an object. The structuring element size for this dataset was 4 pixels. This corresponds to  $4 \mu\text{m}^2$ . This level allows for the effective removal of background noise without erasing small sized platelets. The estimated background illumination from morphological opening is then subtracted from the original image resulting in a noise free image. Figure 4.11 presents the maximum projected (a) unfiltered image in the x-y plane with background illumination. All thrombi are illuminated along with streak of lighting originating from each z plane. Figure 4.11 (b) presents the filtered image in the x-y plane with background illumination removed.

(a)

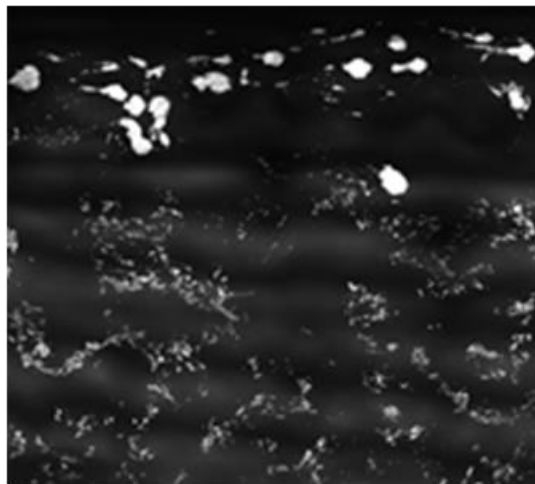


**Figure 4.11** Maximum projected (a) unfiltered image in the x-y plane with background illumination



(b)

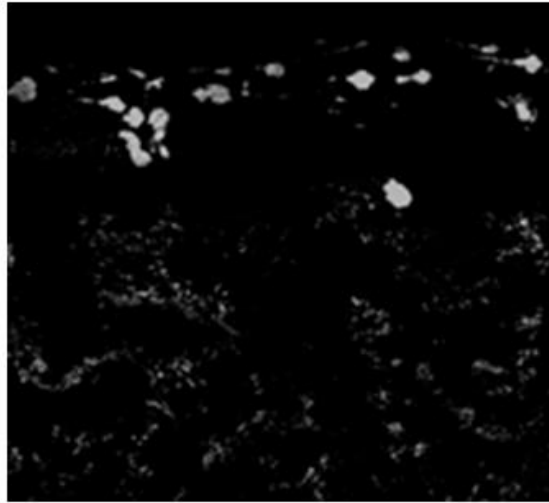


**Figure 4.11** Maximum projected (b) filtered image in the x-y plane with background illumination removed.

#### 4.2.5 Data evaluation

The filtered images were then used to evaluate thrombi growth characteristics between steady and pulsatile flow. Data evaluation was completed through Matlab and three dimensional visualization software Avizo®/VSG. Matlab codes were written to calculate the density of thrombi growth along the length of the sample, to identify individual thrombi and to calculate the size of each identified thrombi. Avizo software was used to three dimensionally reconstruct and evaluate the heights of imaged thrombi (Avizo® / VSG 2012).

The Matlab function reads the fluorescent image, tags individual thrombi and calculates the area of each. Tagging is performed by checking for the number of pixels connected together in a group of pixels. The accuracy of this process is dependent on the connectivity parameter. The connectivity parameter is the minimum number of pixels that must be connected to each other for it to be tagged. This value was set to 2 pixels to allow for identification of individual platelets. Figure 4.12 presents a local region of the microchannel with thrombi identified in red. Once thrombi are tagged area of the identified thrombi is calculated. These values are stored in a vector array allowing for statistical manipulation.

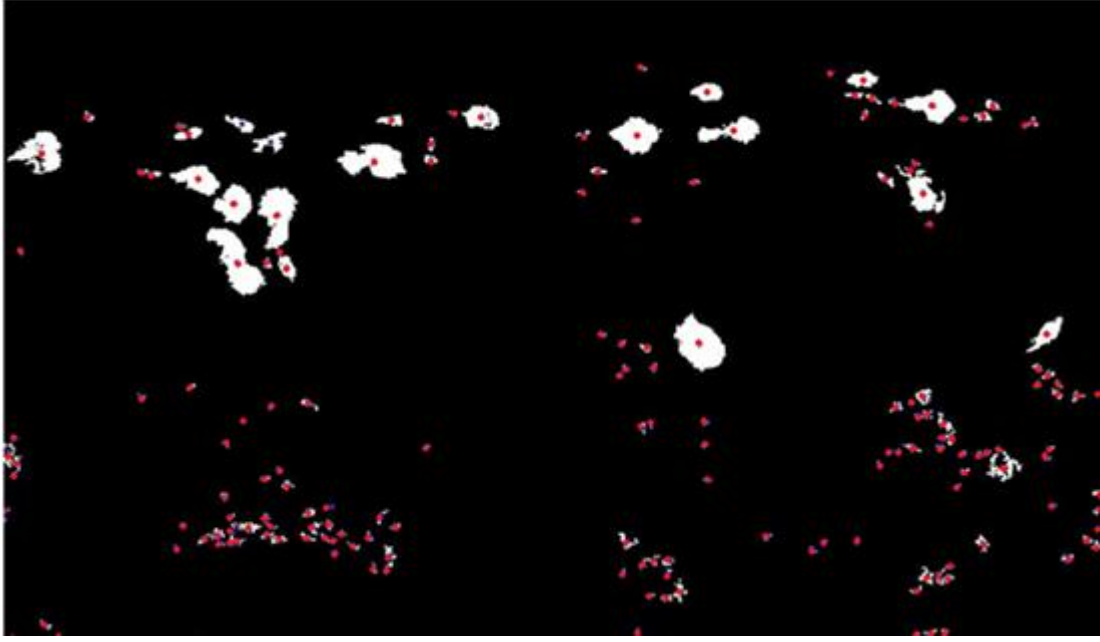


**Figure 4.12** Thrombi identified from Matlab function. Thrombi are identified in red.

#### Density of thrombi growth

Measuring the density of thrombi growth over the length of the imaged sample should provide an understanding of the difference in thrombi development between steady and pulsatile flow. It would also highlight flow regions promoting thrombi development across the y axis of the microchannel. The flow conditions at high thrombi growth regions can be reproduced for future thrombi growth experiments.

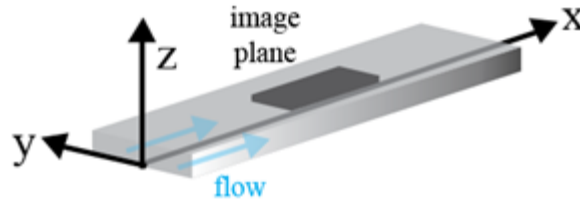


**Figure 4.13** Planar location and direction of flow inside the microchannel.

#### Thrombi population distribution

A Gaussian distribution was used to estimate the population density of thrombi area between steady and pulsatile flow. The function can be described through equation (19). Thrombi smaller than  $5 \mu m^2$  in area were filtered out. At this size they are primarily monolayers. Monolayers are of minor interest for these types of experiments.

$$f(x_{TA}; \mu_{TA}, \sigma_{TA}^2) = \frac{1}{\sigma_{TA}\sqrt{2\pi}} e^{-\frac{(x_{TA}-\mu_{TA})^2}{2\sigma_{TA}^2}} \quad (19)$$

#### *Avizo reconstruction for height estimation*

To obtain measurements of thrombi height Avizo software was used (Avizo® / VSG 2012). Avizo is a three dimensional data processing software. The high resolution z plane image stacks were imported and cleaned for noise. These were then used to three dimensionally visualize and evaluate the height properties of thrombi. Figure 4.14 presents three dimensional reconstruction of (a) thrombi developed under steady flow (b) thrombi developed under pulsatile flow. It can also export this constructed data to CFD software. A collaborative research will use this data to accurately evaluate shear forces experienced by thrombi in in-vitro environments. This research will contribute towards completely simulating thrombi growth through CFD.



**Figure 4.14** Avizo three dimensional re-construction of (a) thrombi developed under steady flow (b) thrombi developed under pulsatile flow.

### **4.3 Results & Discussion**

The maximum projection for steady and pulsatile flow was produced from the z plane image stacks. The maximum projection gives the maximum intensity of volumetric pixels which are parallel to each other and in line with the projection plane. In other words it produces a single image by projecting only the highest intensity pixel between all the image stacks .Figure 4.15 (a) presents the maximum projected steady flow image frame covering an area of 1300 x 1000  $\mu\text{m}$ . Figure 4.15 (b) presents the maximum projected pulsatile flow image frame covering an area of 1300 x 1000  $\mu\text{m}$ .

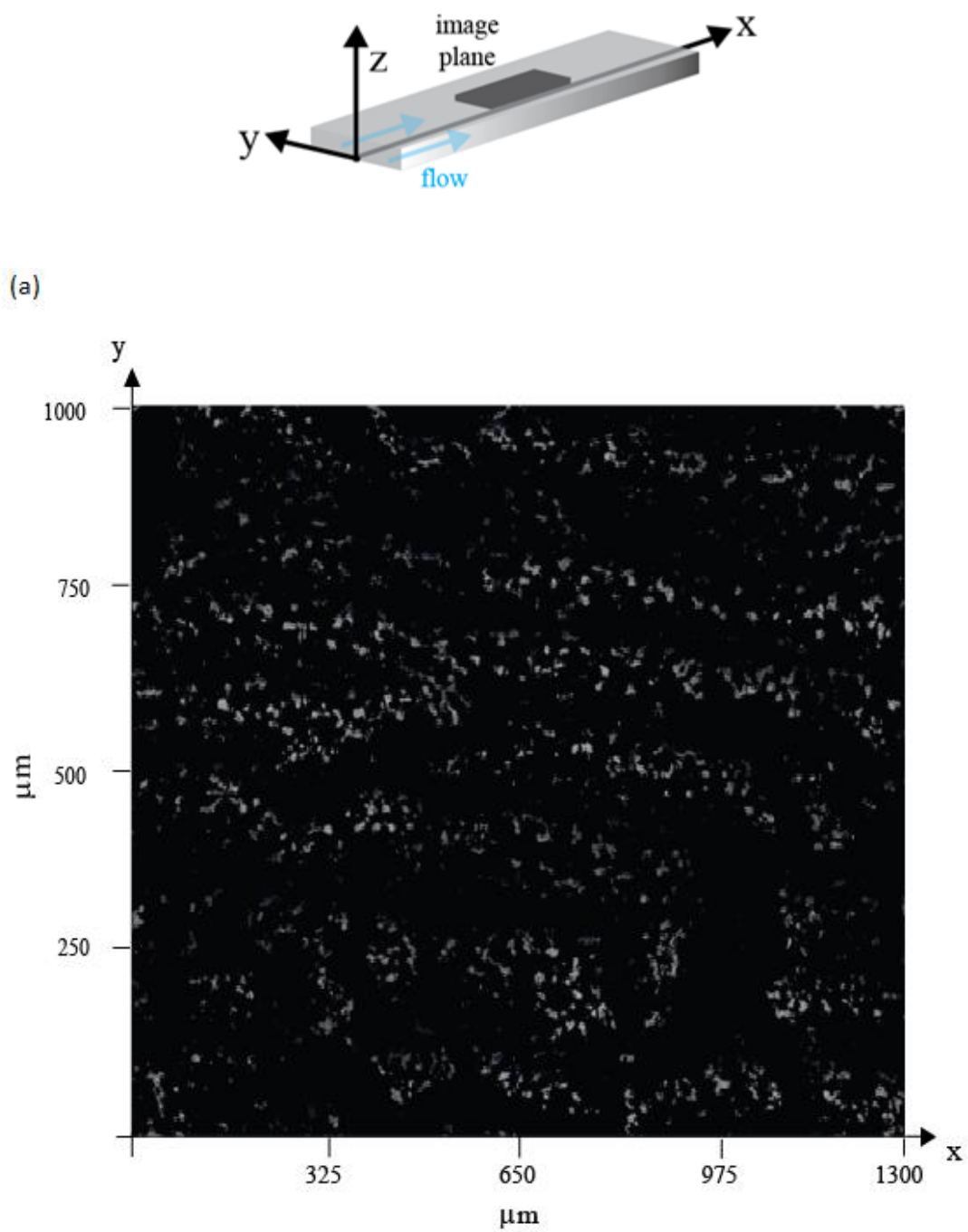


**Figure 4.15** Maximum projected image of (a) steady flow

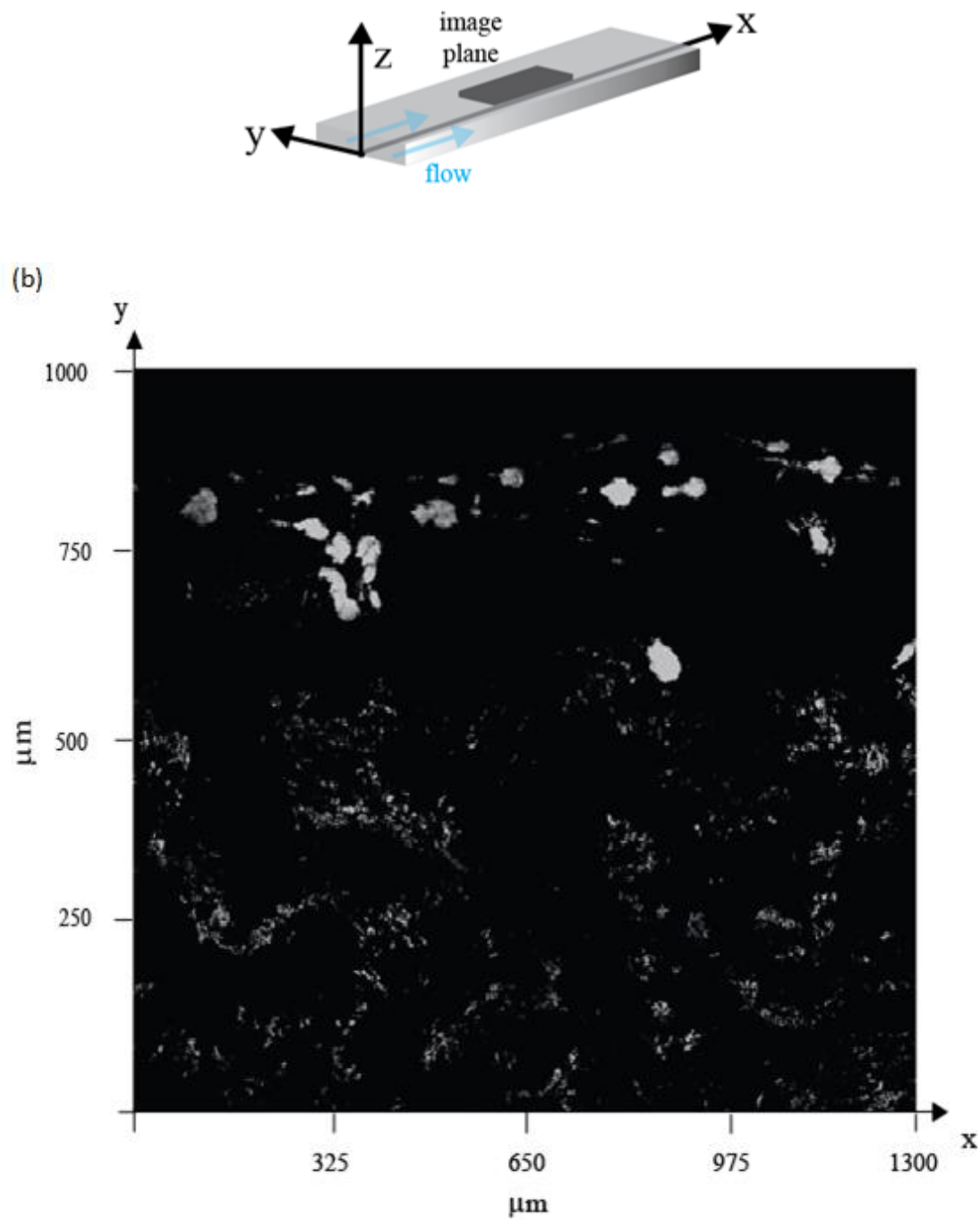
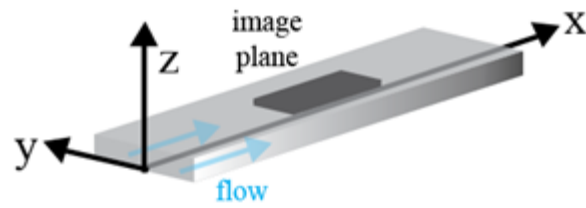


**Figure 4.15** Maximum projected image of (b) pulsatile flow

Density of thrombi growth was measured 1300  $\mu\text{m}$  along the x axis and 1000  $\mu\text{m}$  across y axis, which is half width of the microchannel. Population distribution of thrombi area for steady and pulsatile flow was measured across this range. Thrombi height for ten thrombi each for steady and pulsatile flow at the middle and the wall of the microchannel were measured. Results presented as below.

### 4.3.1 Density of thrombi growth



(a)

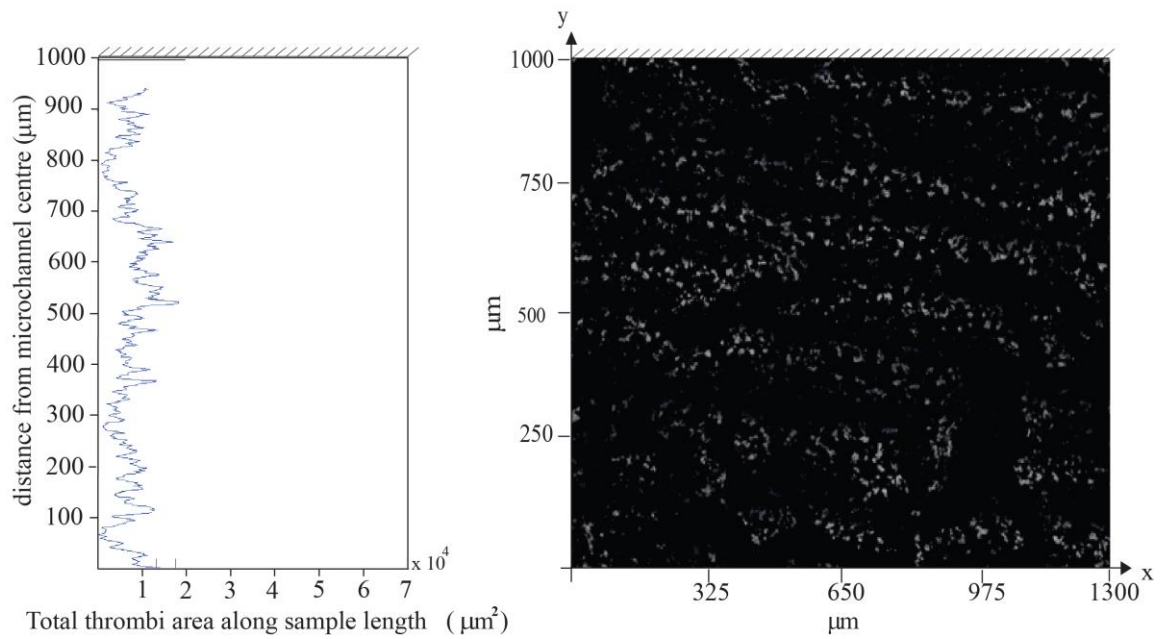
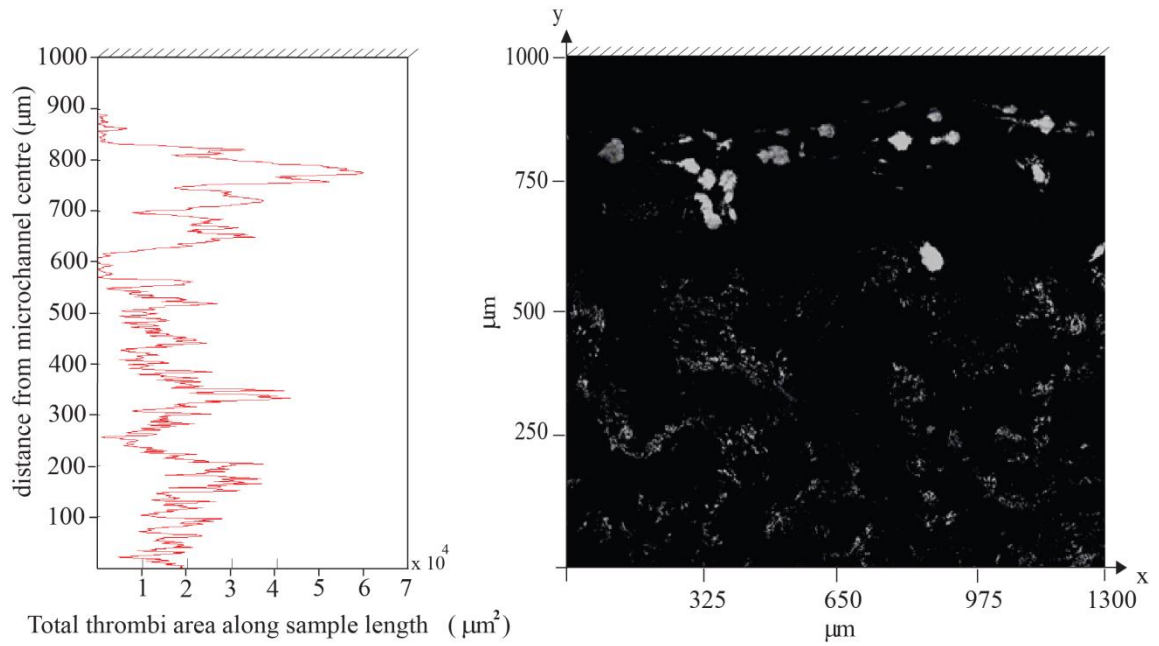


**Figure 4.16** graph of density of thrombi growth over half a width of the microchannel for (a) steady flow. The direction of flow is along the x-axis with the microchannel wall at 1000  $\mu\text{m}$  from the centre of the microchannel

(b)



(c)

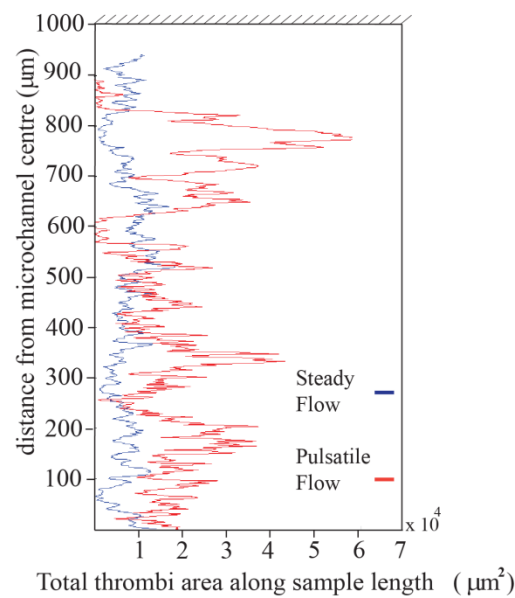


**Figure 4.16** graph of density of thrombi growth over half a width of the microchannel for (b) pulsatile flow (c) steady and pulsatile flow. The direction of flow is along the x-axis with the microchannel wall at 1000  $\mu\text{m}$  from the centre of the microchannel.

The density of thrombi growth for steady flow across half a width of the microchannel is presented in figure 4.16 (a). The variability along the y axis is low. The low number indicates that steady flow conditions do not excessively promote thrombi development. Figure 4.16 (b) shows the density of thrombi growth for

pulsatile flow across half a width of the microchannel. This is an increase over steady flow indicating pulsatile flow promotes additional thrombi growth across the channel. Additionally, in pulsatile flow, near the channel wall at 800  $\mu\text{m}$  from the microchannel centre, significant increase of thrombi growth has occurred. This can be further highlighted from figure 4.16 (c) which is a superimposed image of density of thrombi growth for steady and pulsatile flow. This figure demonstrates the increase in overall thrombi growth and significant thrombi growth at 800  $\mu\text{m}$  from the microchannel centre for pulsatile flow.

The only conditional difference at this location is the flow. As presented in figure 4.17, micro PIV flow results for pulsatile flow shows that this region experiences a specific magnitude range of flow inside the microchannel. Further, in blood vessels the bigger RBC's travel along the central region pushing majority of the platelets towards the wall. Therefore it can be established that pulsatility and the magnitude range of flow in a platelet rich region would promote platelet aggregation over other flow conditions.

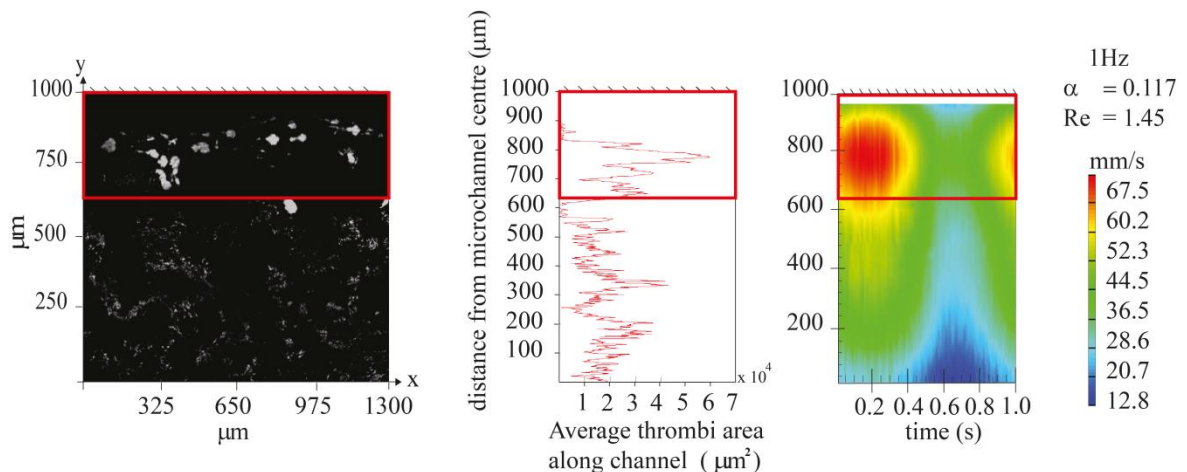


**Figure 4.17** graphical comparison of (a) fluorescence image (b) density of thrombi growth (c) particle image velocimetry at  $z = 50 \mu\text{m}$  plane developed under pulsatile flow. The direction of flow is along the x-axis with the microchannel wall at 1000  $\mu\text{m}$  from the centre of the microchannel.

### 4.3.2 Population density for steady and pulsatile

Figure 4.18 presents the population density distribution of thrombi area for steady and pulsatile flow calculated from Matlab. It is evident that there is a large number of small sized thrombi for steady flow and larger sized thrombi for pulsatile flow. Majority of steady flow thrombi are under  $70 \mu\text{m}^2$ . In contrast, majority of pulsatile flow thrombi are over  $70 \mu\text{m}^2$ . The mean of the distributions are relatively same with steady flow  $23.32 \mu\text{m}^2$  and pulsatile flow with  $21.29 \mu\text{m}^2$ . Significantly, pulsatile flow has produced extremely larger thrombi ranging from  $200 - 750 \mu\text{m}^2$ . The standard deviations of thrombi area for steady and pulsatile flow respectively are  $21 \mu\text{m}^2$  and  $53.45 \mu\text{m}^2$ . These results further supports that pulsatile flow conditions promote thrombi growth creating larger sized thrombi.



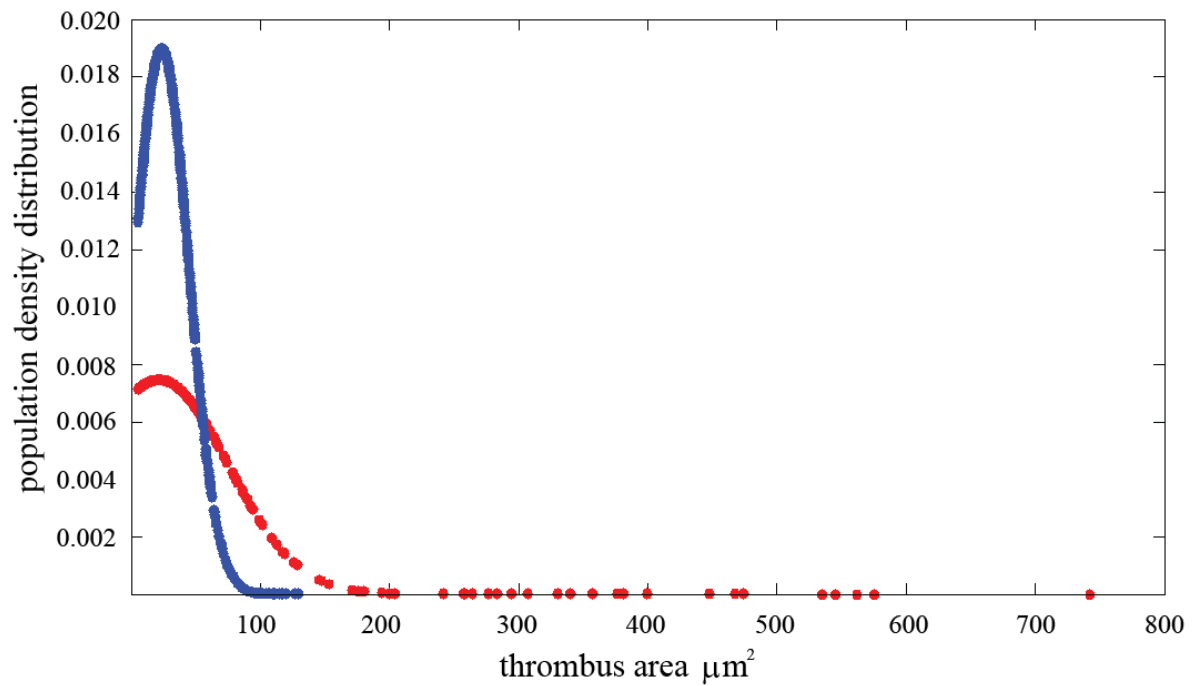
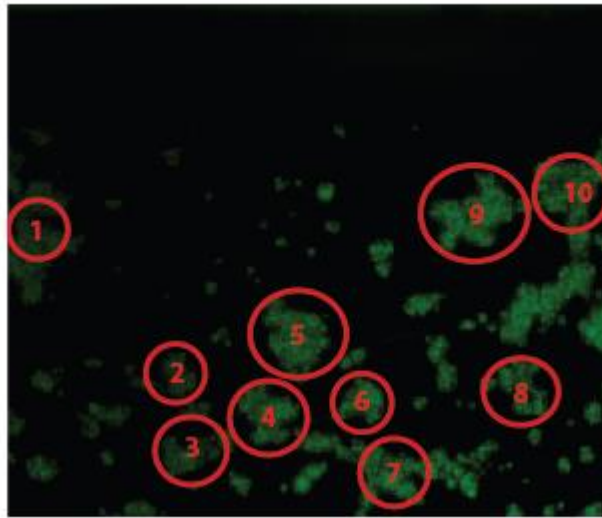


**Figure 4.18** Population density distribution of thrombi area for steady and pulsatile flow.

#### 4.3.3 Thrombus height for steady and pulsatile

Thrombus height is a critical property analysed in physiological experiments (*Tolouei et al. 2011*). For direct comparison, ten thrombi each from steady and pulsatile flow at the middle and the wall of the microchannel were selected and averaged. Using Avizo three dimensional re-construction the heights of these thrombi were measured. Thrombi developed at the middle of the microchannel for pulsatile flow were essentially monolayers of around 4  $\mu\text{m}$ . Figure 4.19 presents an image of (a) ten thrombi selected at the middle of the microchannel for steady flow (b) ten thrombi selected at the wall of the microchannel for steady flow (c) thrombi coverage selected at the middle of the microchannel for pulsatile flow (d) ten thrombi selected at the wall of the microchannel for pulsatile flow.

(a)



(b)

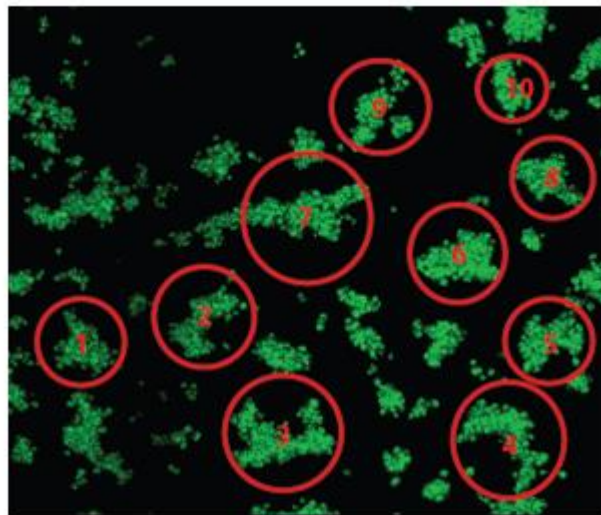
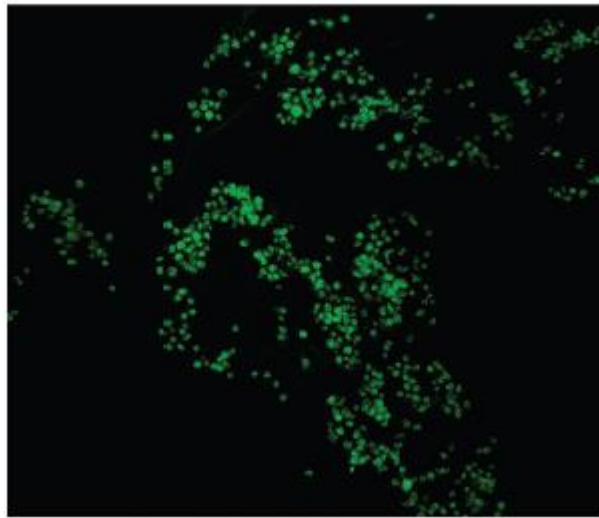


**Figure 4.19** Florescence image of (a) ten thrombi selected at the middle of the microchannel for steady flow (b) ten thrombi selected at the wall of the microchannel for steady flow

(c)



(d)

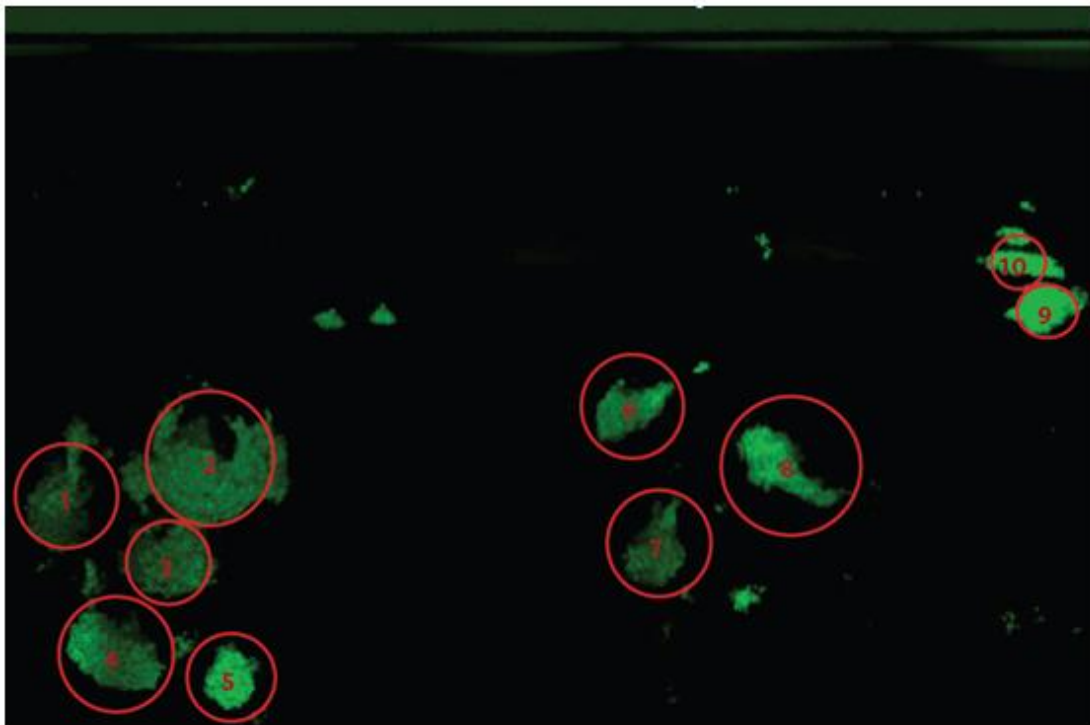


**Figure 4.19** Florescence image of (c) thrombi coverage selected at the middle of the microchannel for pulsatile flow (d) ten thrombi selected at the wall of the microchannel for pulsatile flow.

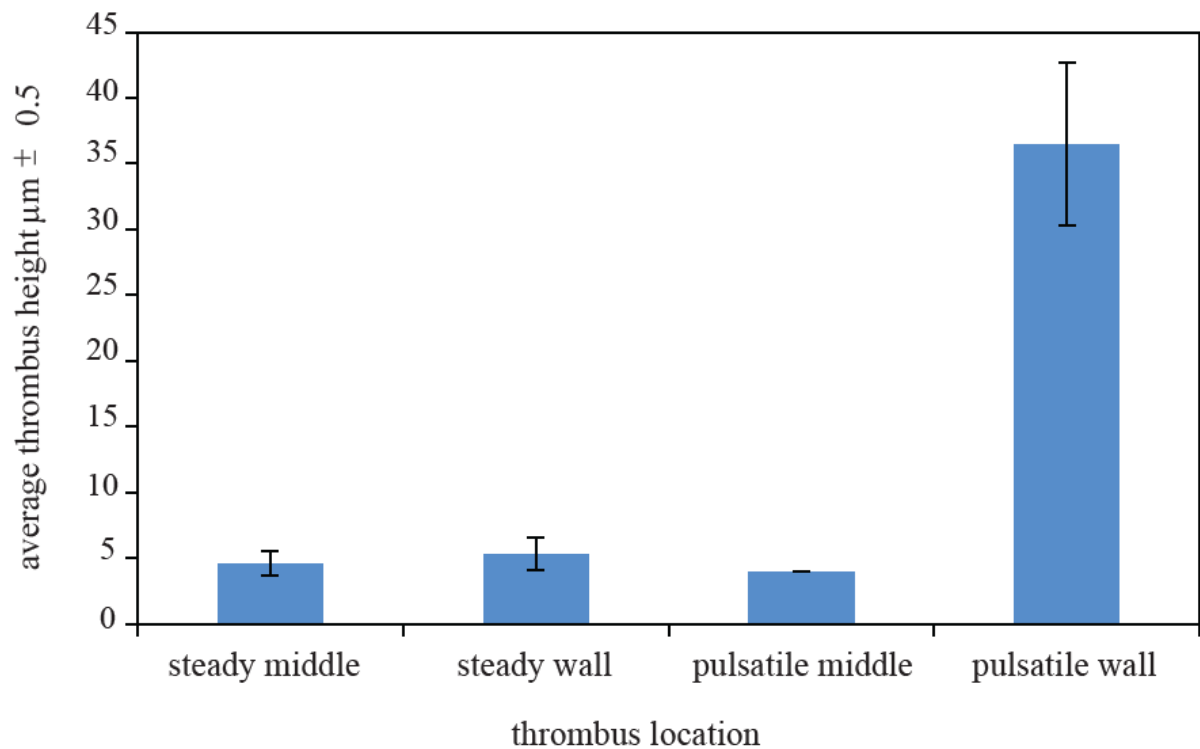


**Figure 4.20** Graph of average thrombi height and standard deviation for ten thrombi selected for steady and pulsatile flow at the middle and wall of the microchannel.

Figure 4.20 presents a bar graph of average thrombi height for ten thrombi selected for steady and pulsatile flow at the middle and wall of the microchannel. Thrombi developed under steady flow at the middle and wall of the microchannel have minor height of 5  $\mu\text{m}$ . Although initial platelet activation has occurred further activation was not promoted under steady flow conditions. In comparison, wall of the pulsatile flow microchannel shows significant thrombi growth across all ten thrombi with an average height of 36.5  $\mu\text{m}$ . pulsatile flow middle of the microchannel middle showed similar heights to steady flow. For typical physiological studies larger sized thrombi over the whole microchannel is favored. These results indicate that specific flow characteristics promote thrombi aggregation.

## 4.4 Chapter conclusion

This chapter presented results contrasting thrombus growth between steady and pulsatile flow produced by the designed prototype flow control system. Thrombi were grown by following thrombus growth procedure developed by Tolouei et al (2001) with microchannel coating procedure developed by Colace et al. (2010). Thrombi were stained with Dihexyloxacarbocyanine Iodide (DiOC<sub>6</sub>) and imaged with multiphoton confocal microscopy. Matlab and Avizo software were used to quantify density and dimensional results of thrombi. Density of thrombi growth was measured 1300  $\mu\text{m}$  along the x axis and 1000  $\mu\text{m}$  across y axis which is half a width of the microchannel. Results showed that steady flow conditions do not excessively promote thrombi development. In contrast pulsatile flow at the wall region showed significant increase of thrombi growth. Micro PIV experiments conducted in chapter 3 show that this region experiences a specific magnitude range of pulsatile flow inside the microchannel. The pulsatility and the magnitude range of flow in a platelet rich region has contributed towards the increase of platelet aggregation over other flow conditions. Population distribution of thrombi area for steady and pulsatile flow was measured across this range. Steady flow produced a large number of small sized thrombi. Pulsatile flow produced extremely larger thrombi ranging from 200 – 750  $\mu\text{m}^2$ . Average height of ten thrombi each for steady and pulsatile flow at the middle and the wall of the microchannel were measured. Steady flow at the middle and the wall produced thrombi with minor height. Pulsatile flow at the middle produced small thrombi. Pulsatile flow at the wall region showed significant growth across all ten thrombi. In combination, these results confirm an increase in thrombi growth for pulsatile flow. The only conditional difference at this location is the flow. Therefore, sinusoidal flow with a mean flow rate of 1.44 ml/min, amplitude of 30% of mean flow at a frequency of 1 Hz near the microchannel wall would promote thrombi growth.

## 5.0 Conclusions

### 5.1 Summary of major findings and contributions to the field

This master's thesis details the development of a real time biocompatible flow control system technique for microchannel based physiological experiments. A prototype system has been developed and validated. The system provides superior functionality and biocompatibility over current systems. The main features of the flow control technique are:

- i. Capability of producing accurate steady and complex flows
- ii. Scalable technique and system for other flow applications
- iii. Ability to run real time or produce pre-programmed flows
- iv. Flow control system is independent of fluid properties allowing universal use in fluid applications
- v. Highly biocompatible low impact flow control method
- vi. Allows for easy cleanup and disposability
- vii. Operates with minimal dead space
- viii. Can be designed to control pressure as well as flow
- ix. Non-contacting pumping mechanism and minimisation of mechanical wear

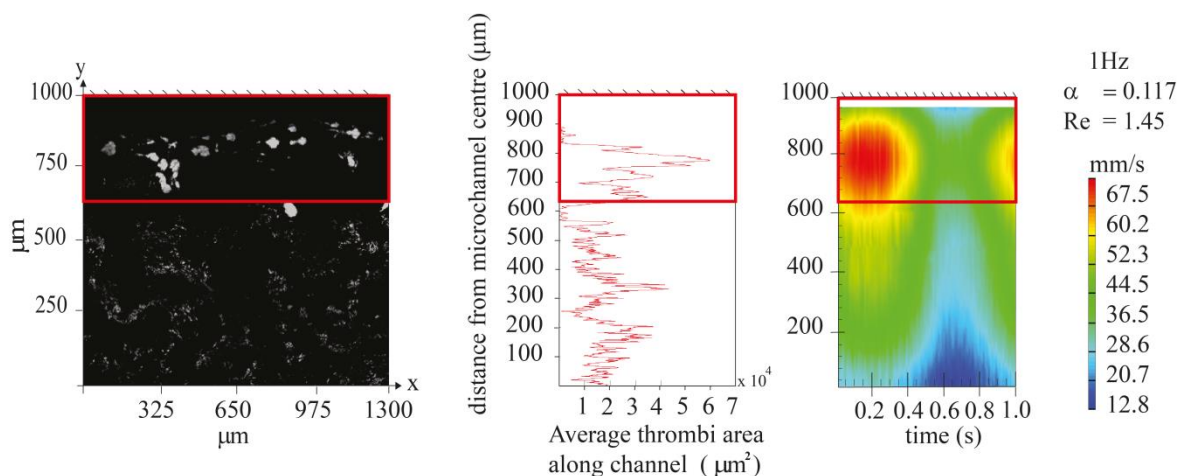
The system scalability (as per table 2.2) allows for increase in flow range, accuracy, pulsatile frequency and number of flow control channels. Performance tests on the prototype showed a steady flow error of 1.2 %. The optimum pulsatile working range was between 1 – 3 Hz with a total harmonic distortion of less than 2% and a root mean square error less than 8% for sinusoidal waveforms. PIV and thrombus growth experiments showed the capability of flow control technique in physiological flow evaluation experiments.

Micro PIV Results showed there is a relationship between regions of altered flow and regions of platelet aggregation. The completed experiments produced velocity profiles inside the microchannel for sinusoidal input waveforms at 1 Hz, 1.5 Hz, 2 Hz, 2.5 Hz relating to the physiological heart rates of 60, 90, 120, 150 beats per minute. The results showed that apart from its rate of change, the velocity profile itself is almost identical for all the frequencies. The maximum velocity of the plane exists slightly away from the center. Therefore it is established that for a fluid viscosity of  $4 \times 10^{-3} \text{ N.s/m}^2$ , sinusoidal frequencies of 1 Hz, 1.5 Hz, 2 Hz and 2.5 Hz would develop Womersley flow inside a high aspect ratio microchannel.

Thrombus growth experiments produced the following findings:

1. The density of thrombi growth along the microchannel between steady and pulsatile flow for half a width of the microchannel was measured. Results showed that steady flow conditions do not excessively promote thrombi growth while pulsatile flow near the microchannel wall showed significant increase of thrombi growth.
2. Population distribution of thrombi developed under steady and pulsatile flow was measured. Steady flow produced a large number of small sized thrombi. Pulsatile flow produced dramatically larger thrombi ranging from 200 – 750  $\mu\text{m}^2$ .
3. Thrombi height between steady and pulsatile flow at the middle and near the wall of the microchannel was measured. Steady flow produced thrombi with lower height throughout the microchannel. Pulsatile flow produced similar small thrombi at the middle of the microchannel. However, at the wall of the microchannel, the height measurement was significantly higher for all ten thrombi that were measured.

Thrombi growth experiments were conducted for steady and pulsatile flow. Results showed pulsatile flow near the wall would promote significant thrombi growth. The experimental conditions were identical except for local flow conditions. Micro PIV was used to evaluate the local flow conditions. This can be seen from figure 4.17 (reproduced below for convenience) which presents graphical comparison of (a) fluorescence image (b) density of thrombi growth (c) particle image velocimetry at  $z = 50 \mu\text{m}$  plane developed under pulsatile flow.



**Copy of Figure 4.17** graphical comparison of (a) fluorescence image (b) density of thrombi growth (c) particle image velocimetry at  $z = 50 \mu\text{m}$  plane developed under pulsatile flow. The direction of flow is along the x-axis with the microchannel wall at 1000  $\mu\text{m}$  from the centre of the microchannel.

The results show the wall region of the microchannel to experience velocities between 33.1 and 67.5 mm/s. In blood vessels the bigger RBC's travel along the central region pushing majority of the platelets towards the wall. Therefore it can be

hypothesised that pulsatile velocities fluctuating between 33.1 and 67.5mm/s in a high platelet dense region would promote the development of thrombi. The newly designed prototype flow control system was used to generate this pulsatile flow. The flow control technique can be used to produce controlled complex flow waveforms in-vitro for experiments where flow is a key condition.

## 5.2 Recommendations for future work

The designed flow control technique and the prototype physiological flow control system extends capabilities beyond those of its predecessors. The following represent the best opportunities for future enhancements.

- Additional negative pressure box to introduce reverse flow.
- Incorporating an adaptive filter algorithm to eliminate manual gain adjustment and introducing auto tuning capabilities.
- Recommended upgrades from section 2.5 to improve speed, accuracy, operating range and the number of control valves of the system.

Flow mechanics can be evaluated in numerous models by producing in-vivo blood flow patterns with the use of the designed system. By measuring additional planes along each axis it would be possible to produce a realistic three-dimensional velocity map inside each model. This would assist in identifying abnormal flow regions in pathological conditions. In blood flow the velocity profile is greatly affected by the distribution of red blood cells (*Sherwood et al. 2014*). Therefore, it is recommended that further experiments are conducted to evaluate the effect of the flow control technique to the distribution of red blood cells.

Studies show that shear rates play a key role in thrombosis (*Tolouei et al. 2011*). However, there is further need for investigation surrounding this topic as research conducted to date has been done over a limited number of shear rates. This was due to lack of capability in current systems to produce a range of shear rates, frequencies and complex waveforms. Experiments were further limited by the small time frame allowed by blood before it starts clotting. With this system ability to produce complex waveforms and control multiple flow channels it would possible to overcome these limitations and conduct a larger volume of experiments over a shorter time period.

With improved optics, researchers will be able to measure thrombi growth as a function of time. The flow control technique of this thesis is highly desirable for these experiments. With real time flow control it is possible to investigate changes in thrombi growth with varying flow patterns. Chemical properties of blood, such as level of hematocrit and collagen concentration, can be altered to investigate the effect each has on thrombus growth. These types of experiments can be further enhanced to trial different medications against desired effects. For example certain drug classes can be assessed against their ability to inhibit platelet activation under various hemodynamic conditions.



The relationship between the geometry of the vessel and pressure for pulsatile flow has not yet been fully explored. The control technique can be modified to be a pressure control system. A feedback pressure system would be able to produce pressure waveforms with varying amplitudes to measure the level of vessel elasticity.

The flow control technique has been beneficial in high frequency “lab on a chip” applications. Figure 6.1 presents a CAD image of a conceptual fluid controlled cross slot designed to isolate and interrogate cell properties (Curtis *et al.* 2011). An improved version of the fluid control system described in this this thesis is currently being developed to address the above application. The control technique will be used with high frequency fluid control valves to isolate a cell in a stagnation point in a cross slot microchip. The isolated cell will then be interrogated for its mechanical properties through fluid forces. It is believed that healthy and diseased cells would contain identifiable dissimilarity in their mechanical properties. In-vitro drug testing can be performed for diseases such as diabetes and malaria.

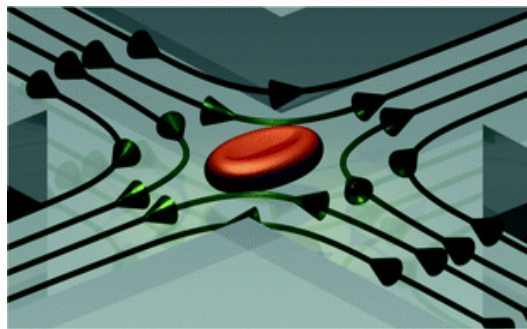


**Figure 5.1** CAD image of a conceptual fluid controlled cross slot designed to isolate and interrogate cell properties. Figure courtesy of (Curtis *et al.* 2011).

The flow control technique of this thesis can be used in cardiovascular models in pathological and physiological studies. By producing in-vivo flow patterns pathological conditions in arteries, veins and bifurcations can be investigated more accurately. The system opens up new avenue for testing the effectiveness of new drugs which can alter local flow conditions to prevent pathological conditions. Animal subjects are commonly used for physiological studies. Ability to replicate in-vivo waveforms outside of the animal would reduce the need for using live test subjects. With increasing demand for organs for transplant and advances in stem cell research this flow control technique would be able to supply in-vivo flow to growing tissue.

The presented results establish that the flow control technique developed in this thesis is a valuable tool to produce and investigate physiological conditions. The increased capability coupled with high potential for improvement provides a base to expand current physiological studies. Future recommendations and potential applications highlight the contribution of this new flow control technique to biomedical research.

## 6.0 References

1. Aarts, P.A. et al., 1988. Blood Platelets Are Concentrated Near The Wall And Red Blood Cells, In The Center In Flowing Blood, Arteriosclerosis, Thrombosis, And Vascular Biology. *Journal of the American Heart Association*, 8, pp.819–824.
2. Analytik Jena, 2012. Aj Cybertron. Available at: <http://www.analytik-jena.de/404.html> [Accessed July 15, 2012].
3. Ansys, 2012. Pumps. Available at: <http://www.ansys.com/Industries/Industrial+Equipment+&+Rotating+Machinery/Pumps+&+Water+Turbines/Pumps> [Accessed July 15, 2012].
4. Ascuitto, R., Ross- Ascuitto, N. & Guillot, M., 2010. Fluid Viscosity Increases Pressure Drop and Exacerbates Flow-Energy Loss (Relevance to Modified-Fontan Patients with Elevated Hematocrit). *CONGENITAL CARDIOLOGY TODAY*, 8(12).
5. Avizo® | VSG, 2012. Avizo® | VSG. Available at: <http://www.vsg3d.com/avizo/overview> [Accessed August 19, 2012].
6. Beaulieu, A. et al., 2011. A flow meter for unsteady liquid flow measurements in total liquid ventilation. *Flow Measurement and Instrumentation*, 22(2).
7. Bitsch, L. et al., 2003. Micro PIV On Blood Flow In A Microchannel. 7th International Conference of Miniaturised Chemical and Biochemical Analysis Systems.
8. Bluestien, D. et al., 1997. Fluid mechanics of arterial stenosis: Relationship to the development of mural thrombus. *Annals of Biomedical Engineering*, 25, pp.344–356.
9. Borgstrom, P., Clementz, L.A. & Grande, P.O., 1981. A Servo Controlled Roller Pump For Constant Flow Or Constant Pressure Blood Perfusion Under Normal Pulsatile Or Non Pulsatile Conditions. *Acta Physiologica Scandinavica*, 112(4), pp.437–442.
10. Bown, M.R., MacInnes, J.M. & Allen, R.W.K., 2007. Three-component micro PIV using the continuity equation and a comparison of the performance with that of stereoscopic measurements. *Experiments in Fluids*, 42(2), pp.197–205.
11. Calil, S.J. & Roberts, V.C., 1985. Detection Of Low-Grade Arterial-Stenosis Using An Automatic Minimum Flow Velocity Tracking System (Mvts) As An Adjunct To Pulsed Ultrasonic Doppler Vessel Imaging. *Medical & Biological Engineering & Computing*, 23(4), pp.311–323.

12. Caro, C. G. 1978, The Mechanics of the circulation / C. G. Caro ... [et al.] Oxford University Press Oxford ; New York
13. Charo, I.F. & Taub, R., 2011. Anti-inflammatory therapeutics for the treatment of atherosclerosis. *Nat Rev Drug Discov*, 10(5), pp.365–376.
14. Colace, T., Falls, E., Zheng, X.L.Z & Diamond, S.L, 2010. Analysis Of Morphology Of Platelet Aggregates Formed On Collagen Under Laminar Blood Flow, *Annals of Biomedical Engineering*, Vol. 39, No. 2.
15. Conklin, B.S. et al., 2000. A Simple Physiologic Pulsatile Perfusion System For The Study Of Intact Vascular Tissue. *Medical Engineering & Physics*, 22(6), pp.441–449.
16. Curtis, M.D., Sheard, G.J. & Fouras, Andreas, 2011. Feedback control system simulator for the control of biological cells in microfluidic cross slots and integrated microfluidic systems. *Lab on a Chip*, (14).
17. DeBakey, M.E., 1999. A Miniature Implantable Axial Flow Ventricular Assist Device. *Annals of Thoracic Surgery*, 68(2), pp.637–640.
18. Douville, Y. et al., 1983. An In-vitro Model And Its Application For The Study Of Carotid Doppler Spectral Broadening. *Ultrasound in Medicine and Biology*, 9(4), pp.347–356.
19. Eitzman, D.. et al., 2000. Hyperlipidemia promotes thrombosis after injury to atherosclerotic vessels in apolipoprotein E-deficient mice. *Arterioscler Thromb Vasc Biol*, 20(7), pp.1831–4.
20. Engineeringtoolbox, 2009. Orifice, Nozzle and Venturi Flow Rate Meters. Available at: [http://www.engineeringtoolbox.com/orifice-nozzle-venturi-d\\_590.html](http://www.engineeringtoolbox.com/orifice-nozzle-venturi-d_590.html) [Accessed July 15, 2012].
21. Enmodes, 2014. Exemplary cases: Rotary Blood Pumps (RBPs), Available at: <http://www.enmodes.de/references/exemplary-cases/rotary-blood-pumps/> [ Accessed Nov 1, 2014]
22. Eriksson, A., Persson, H.W. & Lindstrom, K., 2000. A Computer Controlled Arbitrary Flow Wave Form Generator For Physiological Studies. *Review of Scientific Instruments*, 71(1), pp.235–242.
23. Fahraeus, R. & Lindqvist, T., 1931. The viscosity of the blood in narrow capillary tubes. *The American Journal of Physiology*, 96, pp.562–568.
24. Flexible Learning, 2008. Chemical & Oil Refining, Recognise pumps. Available at: <http://toolboxes.flexiblelearning.net.au/demosites/series2/204v2/PROC201/PROC201-010100-RecognisePumps.htm> [Accessed July 15, 2012].

25. Fouras, A. et al., 2009. Volumetric Correlation PIV: a New Technique for 3D Velocity Vector Field Measurement. *Experiments in Fluids*, 47, pp.569–577.
26. Frayne, R. et al., 1992. Computer-Controlled Flow Simulator For MR Flow Studies. *Jmri-Journal of Magnetic Resonance Imaging*, 2(5), pp.605–612.
27. Greaby, R., Zderic, V. & Vaezy, S., 2007. Pulsatile Flow Phantom For Ultrasound Image-Guided HIFU Treatment Of Vascular Injuries. *Ultrasound in Medicine and Biology*, 33(8), pp.1269–1276.
28. Haguen Finn, 2010. Comparing PI Tuning Methods in a Real Benchmark Temperature Control System. *Modeling, Identification and Control*, Vol. 31, No. 3, pp 79-91
29. H Padleckas, 2006. Metering pump. Available at: [http://en.wikipedia.org/wiki/Metering\\_pump](http://en.wikipedia.org/wiki/Metering_pump) [Accessed July 15, 2012].
30. Hein, I.A. & Obrien, W.D., 1992. A Flexible Blood-Flow Phantom Capable Of Independently Producing Constant And Pulsatile Flow With A Predictable Spatial Flow Profile For Ultrasound Flow Measurement Validations. *Ieee Transactions on Biomedical Engineering*, 39(11), pp.1111–1122.
31. Holdsworth, D.W. et al., 1991. Computer-Controlled Positive Displacement Pump For Physiological Flow Simulation. *Medical & Biological Engineering & Computing*, 29(6), pp.565–570.
32. Hoppmann, W.H. & Liu, J.C.C., 1972. Mechanics Of A Certain Class Of Pumps. *Journal of Biomechanics*, 5(2), pp.153–&.
33. Hoskins, P.R., Anderson, T. & McDicken, W.N., 1989. A Computer Controlled Flow Phantom For Generation Of Physiological Doppler Waveforms. *Physics in Medicine and Biology*, 34(11), pp.1709–1717.
34. Iijima, K. & Salerno, R.A., 1965. Factors Influencing Hemolysis In Model Perfusion Systems. *Annals of Surgery*, 161(1), pp.148–&.
35. Jackson, S.P., 2007. The growing complexity of platelet aggregation. *Blood*, pp.5087–5095.
36. Kim, H.B. et al., 2004. Non-invasive Measurement Of Steady And Pulsating Velocity Profiles And Shear Rates In Arteries Using Echo PIV: In Vitro Validation Studies. *Annals of Biomedical Engineering*, 32(8), pp.1067–1076.
37. Kiyose, T. et al., 1977. Development Of Pump System For Experimental Model Simulation Of Blood Flow In Peripheral Artery. *Fucuoata Acta Med.*, 68, pp.86–91.
38. Krane, M., 2006. A Computer Controlled Pulsatile Pump System for Cardiopulmonary Bypass and Its Effects on Regional Blood Flo, Haemolysis and Inflammatory Response.

39. Ku, D.N. et al., 1985. Hemodynamics Of The Normal Human Carotid Bifurcation - In-vitro And In-vivo Studies. *Ultrasound in Medicine and Biology*, 11(1), pp.13–26.
40. Law, Y.F. et al., 1987. Computer controlled pulsatile pump system for physiological flow simulation. *Medical & Biological Engineering & Computing*, 25(5), pp.590–596.
41. Lee, B.Y. et al., 1978. Hemodynamics of arterial stenosis. *World J Surg*, 2(5), pp.621–7.
42. Libby, P., 2001. Current Concepts of the Pathogenesis of the Acute Coronary Syndromes. *Circulation*, 104, pp.365–372.
43. Lima, R. et al., 2007. In vitro confocal micro PIV measurements of blood flow in a square microchannel: the effect of the haematocrit on instantaneous velocity profiles. *Journal of Biomechanics*, 40(12), pp.2752–2757.
44. Lindken, R., Westerweel, J. & Wieneke, B., 2006. Stereoscopic micro particle image velocimetry. , 41, pp.161–171.
45. Long, A.J. et al., 2005. Viscoelasticity of Pediatric Blood and its Implications for the Testing of a Pulsatile Pediatric Blood Pump. *American Joournal of Artificial Internal Organs*, 51(5), pp.563–6.
46. Lopez, J., Conde, I. & Dong, J., 1999. Platelet function under flow. *Platelet Function: Assessment, Diagnosis, and Treatment*.
47. Nishida, M., Yamane, T., 2004, Geometric Optimisation for Non-Thrombogenicity of a Centrifugal Blood Pump through Computational Fluid Dynamic Analysis, *JSME International Journal Series C Mechanical Systems, Machine Elements and Manufacturing*, Vol. 47
48. Maxwell, M., 2007. Identification of a 2-stage platelet aggregation process mediating shear-dependent thrombus formation.
49. Meinhart, C.D., Wereley, S.T. & Santiago, J.G., 1999. PIV measurements of a microchannel flow. *Experiments in Fluids*, 27, pp.414–419.
50. Nakano, A. et al., 2005. Velocity Profiles of Pulsatile Blood Flow in Arterioles with Bifurcation and Confluence in Rat Mesentery Measured by Particle Image Velocimetry. *JSME International Journal Series C Mechanical Systems, Machine Elements and Manufacturing*, 48(4), pp.444–452.
51. Nesbitt, W.S. et al., 2009. A shear gradient-dependent platelet aggregation mechanism drives thrombus formation. *Nature Medicine*, 15(6), pp.665–U146.
52. Netpumps, 2010. Gear pumps from General Pump and Machinery. Available at: <http://www.netpumps.com/gear-pumps.html> [Accessed July 15, 2012].

53. Olsen, M.G., Adrian, R.J., 2000. Out-of-focus effects on particle image visibility and correlation in microscopic particle image velocimetry *Exp Fluids Suppl*:S166–S174
54. Petersen, J.N., 1984. Digitally controlled system for reproducing blood flow waveforms in vitro. *Medical & Biological Engineering & Computing*, 22, pp.277–280.
55. Pitts, W.H.I. & Dewey, C.F.J., 1975. Programmable pulsatile flow apparatus for simulation of arterial hemodynamics. *Proceedings of San Diego Biomedical Symposium*, 14, pp.119–124.
56. Plewes, D.B. et al., 1995. An MR Compatible Flow Simulator for Intravascular Pressure Simulation. *Medical Physics*, 22(7), pp.1111–1115.
57. Prismatic Solutions, 2012. Prismatic Solutions • Confocal Imaging. Available at: <http://www.prismaticolutions.com/> [Accessed August 19, 2012].
58. Qian, K. et al., 2001. Pulsatile rotary pumps with low hemolysis. *Sheng Wu Yi Xue Gong Cheng Xue Za Zhi*, 18(3), pp.391–3.
59. Qian, K.X., 1990. Hemodynamic Approach to Reducing Thrombosis and Hemolysis in an Impeller Pump. *Journal of Biomedical Engineering*, 12(6), pp.533–535.
60. Raffel, M. et al., 2007. *Particle Image Velocimetry, A Practical Guide*. , (2).
61. Ratner, B.D., 2000. Blood compatibility - a perspective. *Journal of Biomaterials Science-Polymer Edition*, 11(11), pp.1107–1119.
62. Replogle R.L., Meiselman H.J., Merrill E.W., 1967. Clinical implications of blood rheology studies. *Circulation*, 36(1), 148-60.
63. Reul, H. et al., 1974. Hydromechanical simulation of systemic circulation. *Medical and Biological Engineering and Computing*, 12(4), pp.431–436.
64. Robin Gledhill, 2011. Confessions of a Chemical Feed pump Manufacturer. Available at: <http://www.blwhite.com/artchemfeedpump.htm> [Accessed July 15, 2012].
65. RWTH Aachen University, 2010. Perfecting a Life-Saving Blood Pump. Available at: <http://www.apple.com/science/profiles/aachen/> [Accessed July 15, 2012].
66. Santiago, J.G. et al., 1998. A micro particle image velocimetry system. *Experiments in Fluids*, 25(4).
67. Samarage, C.R., Carberry, J., Hourigan, K. & Fouras, A. (2012) Optimisation of temporal averaging processes in PIV. *Experiments in Fluids*. 52(3), 617–631.

68. Savitzky, A. & Golay, M.J., 1964. Smoothing and Differentiation of Data by Simplified Least Squares Procedures. *Analytical Chemistry*, 36, pp.1627–1639.
69. Sheen, H.J. et al., 2008. Unsteady flow behaviors in an obstacle-type valveless micropump by micro PIV. *Microfluid Nanofluid*, 4, pp.331–342.
70. Sherwood, M. J., Kaliviotis, E., Dusting, D., Balabani, Stavroula.,2014, Hematocrit, viscosity and velocity distributions of aggregating and non-aggregating blood in a bifurcating microchannel, *Biomech Model Mechanobiol*. 2014 Apr;13(2):259-73
71. Shou-Shing, H. et al., 2004. Liquid flow in a micro-channel. *Journal of Micromechanics and Microengineering*, 14(4).
72. Sinnot, M., 2006. An Investigation of Pulsatile Blood Flow in a Bifurcation Artery Using a Grid Free Method.
73. Sinton, D., 2004. Microscale flow visualization. *Microfluid Nanofluid*, 1, pp.2–21.
74. Sugii, Y., Nishio, S. & Okamoto, K., 2002. In vivo PIV measurement of red blood cell velocity field in microvessels considering mesentery motion. *Physiological Measurement*, 23, pp.403–416.
75. Taylor, C.A., Hugues, T.J.R. & Zarins, C., 1998. Finite Element Modeling of Three-Dimensional Pulsatile Flow in the Abdominal Aorta: Relevance to Atherosclerosis. *Annals of Biomedical Engineering*, 26, pp.975–987.
76. Thurston, G.B., 1989. Plasma release-cell layering theory for blood flow. *Biorheology*, 26, pp.199–214.
77. Tolouei, E. et al., 2011. Effect of Hemodynamic Forces on Platelet Aggregation Geometry. *Annals of Biomedical Engineering*, 39, pp.1403–1413.
78. Tsai, W. & Savas, O., 2010. Flow pumping system for physiological waveforms. *Medical & Biological Engineering & Computing*, 48(2), pp.197–201.
79. Wada, T. & Fukumoto, T., 2000. Biomechanical diagnosis of atherosclerosis by ultrasound. *Methods of Information in Medicine*, 39(3), pp.246–8.
80. Wereley, S.T. & Meinhart, C.D., 2010. Recent Advances in Micro-Particle Image Velocimetry. *Annual Review of Fluid Mechanics*, 42, pp.557–576.
81. Werneck, M.M., Jones, N.B. & Morgon, J., 1984. Flexible Hydraulic Simulator for Cardiovascular Studies. *Medical & Biological Engineering & Computing*, 22(1), pp.86–89.
82. World Health Organization, 2011. WHO | The top 10 causes of death. WHO. Available at: <http://www.who.int/mediacentre/factsheets/fs310/en/> [Accessed November 17, 2011].

83. Wong, P., Graves, M.J. & Lomas, D.J., 2008. Integrated physiological flow simulator and pulse sequence monitoring system for MRI. *Medical & Biological Engineering & Computing*, 46(4), pp.399–406.
84. Yasuhiko, S. et al., 2005. Velocity measurement of both red blood cells and plasma of in vitro blood flow using high-speed micro PIV technique. *Measurement Science and Technology*, 16.
85. Ziegler, J. G. and Nichols, N. B.: Optimum Settings for Automatic Controllers, *Trans. ASME*, Vol. 64, 1942, s. 759-768